Controlled coupling of nanoparticles to polymer-based photonic structures

Dam Thuy Trang Nguyen

université PARIS-SACLAY

NNT : 2018SACLN014

Thèse de doctorat

école normale supérieure paris–saclay

Controlled coupling of nanoparticles to polymer-based photonic structures

Thèse de doctorat de l'Université Paris-Saclay
préparée à l'Ecole normale supérieure Paris-Saclay

École doctorale n°575 EOBE
Spécialité de doctorat: physique

Thèse présentée et soutenue à Cachan, le 26/01/2018, par

Dam Thuy Trang NGUYEN

Composition du Jury :

Jean-Pierre Hermier Professeur, Université de Versailles Saint-Quentin-en-Yvelines (UMR 8635)	Président
Manh-Huong Phan Associate Professor, University of South Florida	Rapporteur
Sophie Brasselet Directrice de recherche, Université d'Aix-Marseille (UMR 7249)	Rapporteur
Catherine Schwob Professeur, Université Paris VI (UMR 7588)	Examinateur
Isabelle LEDOUX-RAK Professeur, ENS Paris-Saclay (UMR 8537)	Examinateur
Ngoc Diep Lai Maître de Conférences, ENS Paris-Saclay (UMR 8537)	Directeur de thèse

Résumé

Dans ce travail, nous étudions théoriquement et expérimentalement le couplage entre nanoparticules uniques de différentes natures (fluorescentes, non-linéaires, plasmoniques, etc.) et une structure photonique en matériau polymère. Dans un premier temps, nous avons optimisé la méthode dite écriture directe par laser en régime de faible absorption à un photon (LOPA) pour réaliser des structures photoniques de bonne qualité à la demande. Ensuite, nous avons également exploité l'effet thermique induit par le laser d'excitation continue, pour simplifier la méthode de fabrication LOPA et améliorer les structures fabriquées. Puis nous avons introduit de façon précise une nanoparticule unique à un emplacement contrôlé dans la structure photonique. Le couplage nanoparticule/structure photonique a été réalisé par le même système optique. Ce couplage a été démontré par une augmentation du nombre de photons émis par la nanoparticule fluorescente et par une forte amélioration du signal de génération de seconde harmonique. Parallèlement, nous avons effectué des calculs numériques par la méthode FDTD pour prédire les propriétés optiques intéressantes des structures photoniques et pour confirmer les résultats expérimentaux.

Abstract

In this study, we investigate theoretically and experimentally the coupling between nanoparticle and photonic structures. The work focuses on the elaboration and applications of structured polymer materials, as well as the manipulation of optical properties of various kinds of single nano-fillers such as gold nanoparticles, magnetic and nonlinear nanoparticles, etc. The study of each kind of nanoparticle addresses a specific goal. In order to conduct our research, we first built and tested an optical confocal setup, which allowed us to both image and fabricate nanostructures at a sub-lambda resolution. Besides, we propose a method exploiting the thermal effect caused by a continuous-wave laser source to optimize 2D and 3D structures realized by low one-photon absorption (LOPA)-based direct laser writing (DLW). Then by using this technique, we are capable of creating novel 2D and 3D polymeric photonic structures containing nanoparticles of different kind (gold nanoparticles, nonlinear nanoparticles, and magnetic nanoparticles). The characterization of the fabricated structures was carried out using the same confocal setup. We demonstrated a significant enhancement of the optical properties of the nanoparticles embedded inside the photonic structures. We also performed numerical calculations using a finite different time domain (FDTD) method to confirm the experimental results.

Acknowledgement

The past three years have been a period of intense learning for me, not only in the scientific arena, but also on a personal level. Writing this dissertation has had a big impact on me. I would like to reflect on the people who have supported and helped me so much throughout this period.

First and foremost, I would like to express my sincerest and deepest gratitude to my supervisor, Prof. Ngoc Diep Lai for accepting me into his group for my master internship and then PhD study. I am deeply grateful for his continuous support of my PhD study and research, for his patience and immense knowledge. His guidance helped me in all the time of research and writing of this thesis. I also really appreciate all the advices and help he has given to me and my husband during our life in France. One could not wish for a better supervisor.

I would also like to express my sincere thanks and immense gratitude my co-supervisor, Prof. Isabelle Ledoux-Rak. I am gratefully indebted to her for for her scientific guidance, consistent support, and encouragement throughout the duration of my PhD. As the directrice of the laboratory, she has always provided me with the best working conditions, which I appreciate a lot.

I would like to thank my labmates and friends who spent their time discussing the work with me and helping me with my problems, especially Tong Cong, Au Huong, Luong Hoang, Mai Thao. It has been a true pleasure working with them. I would also like to thank Dr. Rasta Ghasemi for her great help in the cleanroom facilities.

I would like to thank the jury members, professor Sophie Brasselet, professor Manh-Huong Phan, professor Catherine Schwob, professor Jean-Pierre Hermier, for your insightful comments and encouragement. All your precious comments and evaluations will help me improve my thesis and widen my research in various perspectives.

Finally, I must express my very profound gratitude to my parents, my sister, and especially my loving husband for providing me with unfailing support and continuous encouragement throughout my years of researching and through the process of writing this thesis. This accomplishment would not have been possible without them. Thank you.

Dedication

I dedicate this thesis to my newborn daughter, Ban Mai.

List of publications (related to this work)

- **Nguyen, D. T. T.**, Do, M. T., Li, Q., Tong, Q. C., Au, T. H., and Lai, N. D., "*One-photon absorption-based direct laser writing of three-dimensional photonic crystals*", Book chapter, "Photonic Crystals" Intech (2017).
- **Nguyen, D. T. T.**, Del Guercio, O., Au, T. H., Trinh, D. T., Mai, N. P. T., and Lai, N. D., "*Direct laser writing of three-dimensional magneto-photonic microdevices*", to be published in Optical Engineering journal (2018).
- Mao, F., Tong, Q. C., **Nguyen, D. T. T.**, Au, T. H., Odessey, R., Saudrais, F., and Lai, N. D., "*LOPA-based direct laser writing of multi-dimensional and multi-functional photonic submicrostructures*", Proc. SPIE 10115, Advanced Fabrication Technologies for Micro/Nano Optics and Photonics X, 1011509 (2017).
- Vu, T. V. P., Nguyen, M. T., **Nguyen, D. T. T**, Vu, T. D., Nguyen, D. L., An, N. M., Nguyen, M. H., Sai, C. D., Bui, V. D., Hoang, C. H., Truong, T. T., Lai, N. D., Nguyen-Tran, T., "*Three-Photon Absorption Induced Photoluminescence in Organo-Lead Mixed Halide Perovskites*", Journal of Electronic Materials 46, 3622 (2017).
- Tong, Q. C., Luong, M. H., Remmel, J., Do, M. T., **Nguyen, D. T. T.**, Lai, N. D., "*Rapid direct laser writing of desired plasmonic nanostructures*", Optics Letters 42, 2382-2385 (2017).
- Tong, Q. C., **Nguyen, D. T. T.**, Do, M. T., Luong, M. H., Journet, B., Ledoux-Rak, I., and Lai, N. D., "*Direct laser writing of polymeric nanostructures via optically induced local thermal effect*," Applied Physics Letters 108(18), 183104 (2016).
- **Nguyen, D. T. T.**, Au, T. H., Tong, Q. C., Luong, M. H., Pelissier, A., Montes, K., Ngo, H. M., Do, M. T., Do, D. B., Trinh, D. T., Nguyen, T. H., Palpant, B., Hsu, C. C., Ledoux-Rak, I., and Lai, N. D., "*Coupling of a single active nanoparticle to a polymer-based photonic structure*", Journal of Science: Advanced Materials and Devices 1, 18-30 (2016).
- **Nguyen, D. T. T.**, Tong, Q. C., Ledoux-Rak, I., Lai, N. D., "*One-step fabrication of submicrostructures by low one-photon absorption direct laser writing*

technique with local thermal effect," Journal of Applied Physics 119(1), 13101 (2016).

- **Nguyen, D. T. T.**, Pelissier, A., Montes, K., Tong, Q. C., Ngo, H. M., Ledoux-Rak, I., Lai, N. D., "*Deterministic embedding of a single gold nanoparticle into polymeric microstructures by direct laser writing technique,*" Proc. SPIE 9884, Nanophotonics VI, 98842C (April 2016).
- Do, M. T., **Nguyen, D. T. T.**, Ngo, H. M., Ledoux-Rak, I., and Lai, N. D., "*Controlled coupling of a single gold nanoparticle in polymeric microstructure by LOPA-based direct laser writing technique*", Nanotechnology 26, 105301 (2015).
- Nguyen, T. T. N., Luong, M. H., Do, M. T., Kieu, D. M., Li, Q., **Nguyen, D. T. T.**, Tong, Q. C., Ledoux-Rak, I., Lai, N. D., "*Micro and nanostructuration of polymer materials and applications*," Proc. SPIE 9171, Nanobiosystems: Processing, Characterization, and Applications VII, 91710O (August 2014).

Conference contributions

- **Nguyen, D. T. T.**, Au, T. H., Tong, Q. C., Odessey, R., Ledoux-Rak, I., and Lai, N. D., "*Fabrication and characterization of polymeric microstructures containing single nanoparticle by direct laser writing*", 3rd International Symposium on Frontiers in Materials Science, Hanoi, Vietnam (September 2016), Oral.

- **Nguyen, D. T. T.**, Pelissier, A., Montes, K., Tong, Q. C., Ngo, H. M., Ledoux-Rak, I., and Lai, N. D., "*Deterministic embedding of a single gold nanoparticle into polymeric microstructures by direct laser writing technique,*" SPIE Photonic Europe, Brussels (April 2016), Poster.

- **Nguyen, D. T. T.**, Tong, Q. C., Ngo, H. M., Ledoux-Rak, I., and Lai, N. D., "*Couplage contrôlé des nanoparticules d'or dans des structures photoniques en polymère*", Optique Bretagne, Rennes (July 2015), Poster.

- **Nguyen, D. T. T.**, Do, M. T., Tong, Q. C., Ngo, H. M., Ledoux-Rak, I., and Lai, N. D., "*Precisely embedding a single gold nanoparticle into polymeric*

photonic structure by LOPA-based direct laser writing", GLEAM'15 - Games of Light with Meta-Molecules: Communicating, Sensing and Imaging, Cachan (June 2015), Poster.

- Nguyen, T. T. N., Luong, M. H., Do, M. T., Kieu, D. M., Li, Q., **Nguyen, D. T. T.**, Tong, Q. C., Ledoux-Rak, I., and Lai, N. D., "*Micro and nanostructuration of polymer materials and applications*", SPIE Optics and Photonics, San Diego (August 2014), Invited talk.

Contents

Résumé i

Abstract iii

Acknowledgment iv

List of publications vi

Contents ix

1 General Introduction 1

2 Low one-photon absorption direct laser writing with optically induced local thermal effect 11

2.1 Introduction . . . 11
2.2 LOPA-based DLW technique . . . 15
2.2.1 Electromagnetic field distribution of a tightly focused beam in an absorbing medium . . . 15
2.2.2 Numerical calculation of point spread function . . . 17
2.3 Theoretical model of optically induced local thermal effect . . . 22
2.4 LOPA-based DLW by local PEB . . . 28
2.4.1 LOPA-based DLW system . . . 28
2.4.2 Sample preparation . . . 31
2.4.2.1 Substrate cleaning . . . 32
2.4.2.2 Deposition of SU8 . . . 32
2.4.3 Fabrication process . . . 33
2.4.3.1 Exposure process . . . 33
2.4.3.2 Post exposure bake . . . 34
2.4.3.3 Development process . . . 34
2.4.4 2D and 3D microstructures fabrication enabled by LOPA DLW with local PEB . . . 35
2.4.4.1 Small featured size structures . . . 35
2.4.4.2 Accumulation-free and short period structures . . . 38

2.4.4.3 Uniform shrinkage structures . . . 41
2.5 Potential applications . . . 44
2.5.1 Hybrid surface-enhanced Raman scattering substrate from gold nanoparticles and photonic crystal . . . 44
2.5.2 Optomechanics in polymer for sensor applications . . . 46
2.5.3 DFB laser with controllable emitting direction using perovskite material . . . 47
2.6 Conclusion . . . 48

3 Realization of magneto-photonic microstructures and microdevices 49
3.1 Introduction . . . 49
3.2 Synthesis of photopatternable magneto-polymer nanocomposite . . . 51
3.2.1 Preparation of superparamagnetic nanoparticles . . . 51
3.2.2 Magnetic-polymer nanocomposites . . . 52
3.2.2.1 Influence of SU8 viscosity and MNPs concentration . 52
3.2.2.2 Influence of time on MNPs dispersion and homogeneity 55
3.2.3 Typical hybrid properties of nanocomposites . . . 56
3.2.3.1 Absorption spectrum . . . 56
3.2.3.2 Optically induced thermal effect . . . 57
3.2.3.3 Submicroscale manipulation by an external magnetic field . . . 58
3.3 Realization of 2D and 3D magneto-photonic structures on demand . . 58
3.4 Fabrication on demand of free-floating submicrostructures by LOPA-based DLW . . . 62
3.5 Realization of 3D magneto-photonic devices . . . 64
3.6 Discussion . . . 67
3.7 Conclusion . . . 68

4 Coupling of a single gold nanoparticle into photonic structures 71
4.1 Introduction . . . 71
4.2 Localized plasmonic resonance and plasmonics/photonics coupling: theoretical calculations . . . 72
4.2.1 Localized surface plasmonic resonance . . . 73
4.2.2 Coupling of light into cavities . . . 75
4.2.3 Plasmonics/photonics coupling . . . 76
4.2.4 Enhanced light out-coupling . . . 79
4.3 Coupling of a single gold nanoparticle to a polymer-based photonic structure: experimental demonstration . . . 80
4.3.1 Characterization of gold nanoparticles . . . 81
4.3.2 Sample preparation . . . 82
4.3.3 Precisely positioning a single NP . . . 83
4.3.4 Embedding single NP into PC . . . 85

4.3.5 Effect of PEB on the quality of structures . . . 87
4.3.6 Characterization: Fluorescence measurement . . . 89
4.3.7 Influence of gold particle sizes . . . 90
4.4 Conclusion . . . 92

5 Controlled coupling of KTP nanoparticles into photonic structures 93
5.1 Introduction . . . 93
5.2 Characterization of KTP NPs . . . 95
5.2.1 Experimental setup . . . 95
5.2.2 Sample preparation . . . 95
5.2.3 Emission signal of a single KTP NP . . . 97
5.3 Controlled coupling of a single KTP nanoparticle into a polymeric photonic structure . . . 102
5.3.1 Sample preparation and fabrication process . . . 102
5.3.2 Control of size and shape of structures . . . 104
5.3.3 Control of position of NP in structures . . . 108
5.4 SHG signal enhancement . . . 109
5.4.1 Experimental measurement . . . 109
5.4.2 Simulation model . . . 111
5.4.2.1 Influence of the cavity . . . 111
5.4.2.2 Influence of dipole orientation . . . 116
5.5 Conclusion . . . 117

Conclusions and Prospects 119

Appendices 123

A The PSF of high NA OLs 125

B The calculation of local thermal effect induced by a focused laser beam 127

C Optical characteristics of KTP 131

Bibliography 133

Chapter 1

General Introduction

The age of nanotechnology was born with the invention and development of tools that could see and manipulate nanostructures and nanoparticles, such as super-resolution optical microscope (OM), scanning electron microscope (SEM), atomic force microscope (AFM), scanning tunneling microscope (STM), and transmission electron microscopy (TEM), etc. Since then, nanotechnology has drawn a great deal of attention due to its capability and diversity, with many subject areas under its banner, for example, nanoelectronics, nanomaterials, nanomechanics, nanomagnetics, nanophotonics, nanobiology, nanomedicine, etc. [1].

The key to nanotechnology is the imaging and making of various nanostructures. Among commercially available microscopies techniques, conventional OM is widely used in most optical experiments due to its simplicity and low-cost and its specific advantages compared with others. Nowadays, OM becomes a necessary tool of any multidisciplinary laboratory. Moreover, thanks to the use of high numerical aperture objectives, the optical resolution of OM down to sub-wavelength scale will allow one to exploit many interesting physical phenomena and to offer potential applications. The use of an OM to optically address a small object can be distinguished in two ways: it images the nano-object (imaging) and/or it fabricates the nano-object (fabrication). For example, an optical nanofocusing spot increases the capacity of a memory disk from several gigabits to even a terabit by writing (fabrication) bits closer to each other and reading them (imaging) at nanoscale. Though it is still a

long way for this optical nanotechnology to reach its practical applications, it definitely has its place in the nanoscience and nanotechnology research community. The development of a simple and robust OM which can address multiple tasks at the same time would be of great interest.

Together with the ongoing development of a more efficient optical nanotechnology, a great deal of interest has been devoted to working with suitable and inexpensive materials, which would form desired nanostructures. In fact, the major challenge for nanostructure study is the fabrication of these structures with sufficient precision and processes that can be robustly mass-produced [2]. Organic or polymer materials recently appeared as a material of choice for fabrication of photonic devices, such as light emitting diodes, integrated lasers, photovoltaic cells or photodetectors, etc. [3]. Organic molecular systems offer unique opportunities in nanophotonics since both top-down and bottom-up strategies can be pursued towards the nanoscale. Indeed, the nanotechnology approach permits down-scaling the patterning of polymer materials in order to build either single nano-objects (*e.g.*, nanocavity, single quantum device, nanolaser, etc.) or nanostructured materials (*e.g.*, photonic bandgap materials, distributed feedback lasers, resonant waveguides gratings, etc.) [4].

Meanwhile, nano-object or nanoparticle (NP) research is currently of great scientific interest, due to a wide range of potential applications in biomedical, optical, and electronic fields. NPs are effectively a bridge between bulk materials and atomic or molecular structures. They possess size-dependent properties such as quantum confinement in semiconductor particles, surface plasmon resonance in metal particles and superparamagnetism in magnetic materials. These featured properties make NPs the key factor in many recent researches. Specifically, semiconductor quantum dots [5] or color centers in diamond nanocrystals [6, 7] can serve as single photon emitters in quantum optics or quantum information applications [8], magnetic NPs can be used for data storage [9, 10] and biomarkers [11], metallic NPs allow one to obtain thermal nanosources [12, 13] and to strongly enhance local electromagnetic field [14], and nonlinear NPs can be also used as biomarkers [15] or sensitive sensor systems [16].

In many practical applications, functional materials with optical, electric, magnetic or mechanical properties, which common polymers do not exhibit, are highly desirable. Therefore, functional nanostructures began to be designed by doping them

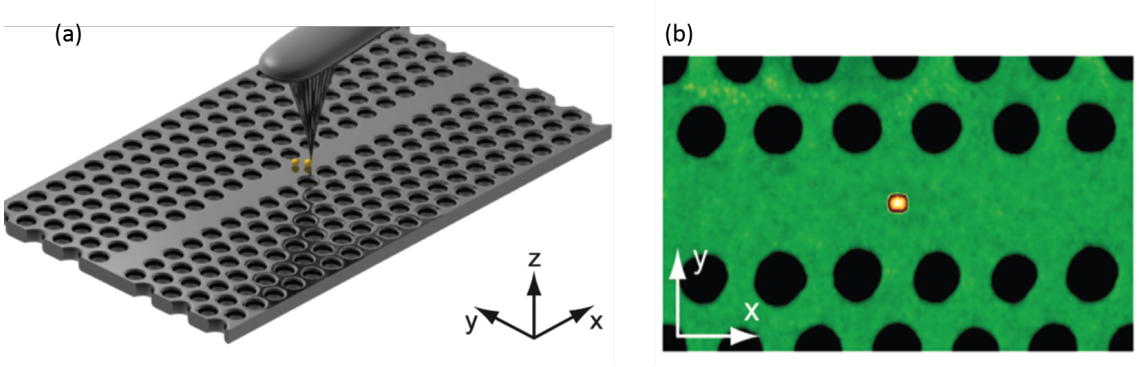

FIGURE 1.1: (a) Illustration of the method used to introduce a single metallic nanoparticle into a photonic crystal cavity. (b) AFM image of a photonic crystal cavity containing a gold nanoparticle on the top surface [26].

with special substances, such as metallic [17], semiconductor [18], or magnetic [19] NPs, into the common polymers to exploit the hybrid properties. The ensemble can be optically structured in a desired way to obtain a polymer-based photonic nanostructure (the host) containing active materials (the guest). This host/guest coupling can have an effect on both sides, depending on specific application. The photonic structure (PS) can, for example, enhance the nonlinear optical property of the guest thanks to field confinement and anormal dispersion effects [20, 27] or modify the fluorescent property through the Purcell effect [22, 23]. In other cases, the guest can also modify the optical property of photonic systems. For instance, the photoinduced effect of doped nonlinear polymer materials can help modify the refractive index contrast of the whole structure, thus tuning the so-called photonic bandgap of the PS [24, 25].

Due to the above reasons, the concept of PS containing fluorescent molecules or active nano-objects has drawn a great attention in the past decades. Figure 1.1 presents a hybrid cavity system coupling with gold nanorods realized by AFM manipulation technique [26]. To realize the hybrid cavity system they used a modified dipping technique in combination with AFM manipulation. They dipped the end of a tapered fiber into a solution of chemically grown gold NPs and brought it into contact with the silicon nitride surface near the photonic crystal structure. By this way, individual gold NPs could be selected and moved into the cavity using the tip of an AFM. The coupling of metallic NPs to photonic crystal cavity can lead to strongly localized fields and enhanced optical feedback provided by surrounding structure.

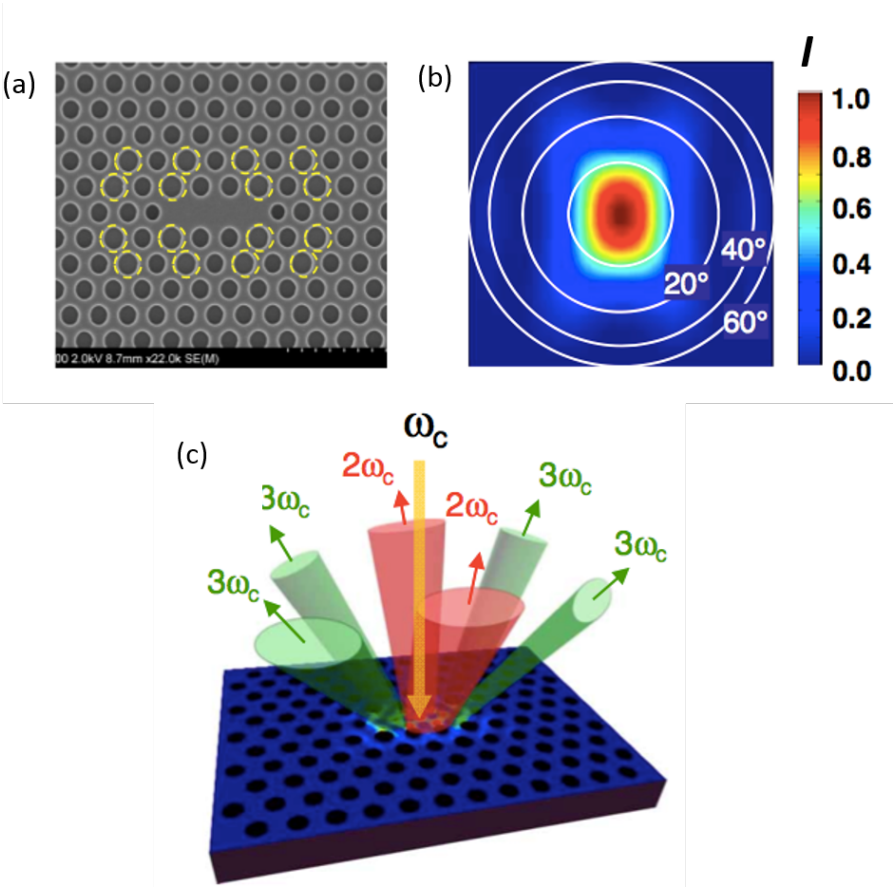

FIGURE 1.2: Photonic crystal cavity enhanced nonlinear optical effects. (a) SEM image of a modified photonic crystal cavity (L3 type): the yellow marks indicate the enlarged holes around the cavity. (b) Far-field intensity profile calculated for the cavity shown in (a) by 3D FDTD simulation. (c) Illustration of the second- and third-harmonic generations emissions from the photonic crystal cavity [27].

Hybrid plasmonic-photonic cavities may find wide application in integrated opto-plasmonic devices for quantum information processing, as efficient single photon sources or nano lasers.

Optical nonlinear conversion such as second- and third-harmonic generation (SHG and THG) was extensively studied using nonlinear materials of different forms, bulk or nanocrystals. Large size nonlinear materials are mainly used to generate strong harmonic light or electro-optics effect. For other applications, such as sensors or biomarkers, nonlinear NPs should be used [15, 16]. Different kinds of nonlinear NPs have been fabricated and studied, such as nano KTP [29, 30], or QDs [31, 32], etc. However, due to the small size of the NPs, the resulting nonlinear effect is very weak, even it was realized by using a strong femto-second laser source. In

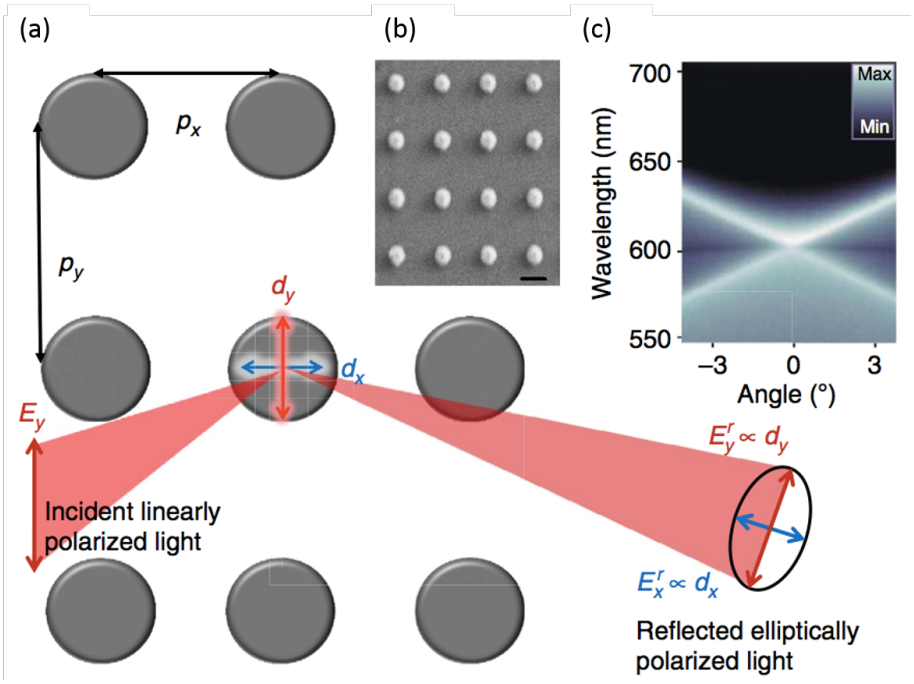

FIGURE 1.3: Magnetic structures enhanced magneto-optical response. (a) Illustration of a 2D magnetic structure and resulting optical response. (b) SEM image of an ordered rectangular array of cylindrical Ni submicro-dots. Scale bar, 200 nm. (c) Theoretical calculation of angle- and wavelength-resolved optical transmission of a sample with $p_x = p_y = 400$ nm and with dots diameter 120 nm [28].

order to optimize the nonlinear conversion, one possible way is to couple these NPs to PSs, as in the case of a single photon source. Actually, optical nonlinear [33] and lasing effects [34] have been observed in simple cavities, such as nanopillars. Recently, it has been demonstrated that nonlinear optical effects, such as SHG and THG, can be realized even in a continuous regime, *i.e.*, by continuous-wave light conversion, by using a photonic crystal nanocavity containing a nonlinear NP [27, 35]. The effective size of the nonlinear particle embedded in the photonic crystal nanocavity is quite small, but the nonlinear effect is giant thanks to a strong local field, fundamental and harmonic, corresponding to the defect mode of the cavity [36]. Figure 1.2 represents the coupling of a nonlinear material to a photonic crystal (PhC) cavity. Both SHG and THG were simultaneously observed by using only a continuous-wave fundamental laser beam [1].

[1]This coupling has been realized by using the same semiconductor material for both nonlinear NPs and PSs. The device was fabricated from a SOITEC silicon-on-insulator wafer using electron-beam lithography and reactive ion etching with a CHF_3/SF_6 gas mixture. The lattice constant of the photonic crystal was 420 nm with r/a = 0.28.

Magnetic NPs (MNPs) commonly consist of magnetic elements such as iron, nickel (Ni), cobalt (Co), or negative charged nitrogen-vacancy color centers in diamond, with a typical size of about 1–100 nm. These NPs can be manipulated by a magnetic field gradient and be optically detected [37–39]. Therefore MNPs have attracted many applications, such as catalysis and biomedicine [11], high sensitivity magnetic resonance imaging and sensors [40, 41], and high capacity data storage [9, 10], etc. Besides, it is also interesting to organise these NPs in micro- and nanostructures, which may possess novel properties, and could be useful for other applications. Various methods have been proposed to fabricate desired magnetic structures. In an effort to realize magneto-optical properties at the nanoscale, Kataja *et al.* [28] have fabricated a periodic rectangular array of cylindrical Ni dots to examine surface plasmon modes in which two directions of lattice are coupled by controllable spin-orbit coupling. It has been shown that the localized surface plasmon resonance supported by the Ni dots hybridized with narrow line-width diffracted orders of the lattice via radiation fields. By breaking the symmetry of the lattice, the optical response shows a prominent Fano-type surface lattice resonance (SLR) that is associated with the periodicity orthogonal to the polarization of the incident field. Consequently, the polar magneto-optical Kerr effect (MOKE) response is strongly modified by the SLR. Figure 1.3 shows the Ni magnetic structure, fabricated by e-beam lithography of a resist followed by e-beam evaporation of a nickel film and lift-off, and the corresponding theoretical and experimental results. The induced dipole moments, d_x and d_y, affect the optical response of the system when an external electric field E_y is applied. As a result, the polarization of reflected light turns into elliptical.

Although various complex photonic structures containing different kinds of NPs have been proposed and realized, leading to a lot of interesting applications, it should be noted that the materials and fabrication methods used for those structures remain expensive and time consuming. *Therefore, an investigation of a simple and low-cost technique which can address various kinds of NP for both fabrication and characterization is a strong motivation.* Figure 1.4 illustrates a general idea of coupling of a single NP with a PS. Different kinds of single NPs (quantum emitter, metallic, magnetic, and nonlinear optics) could be envisoned to be coupled with desired PSs for specific applications.

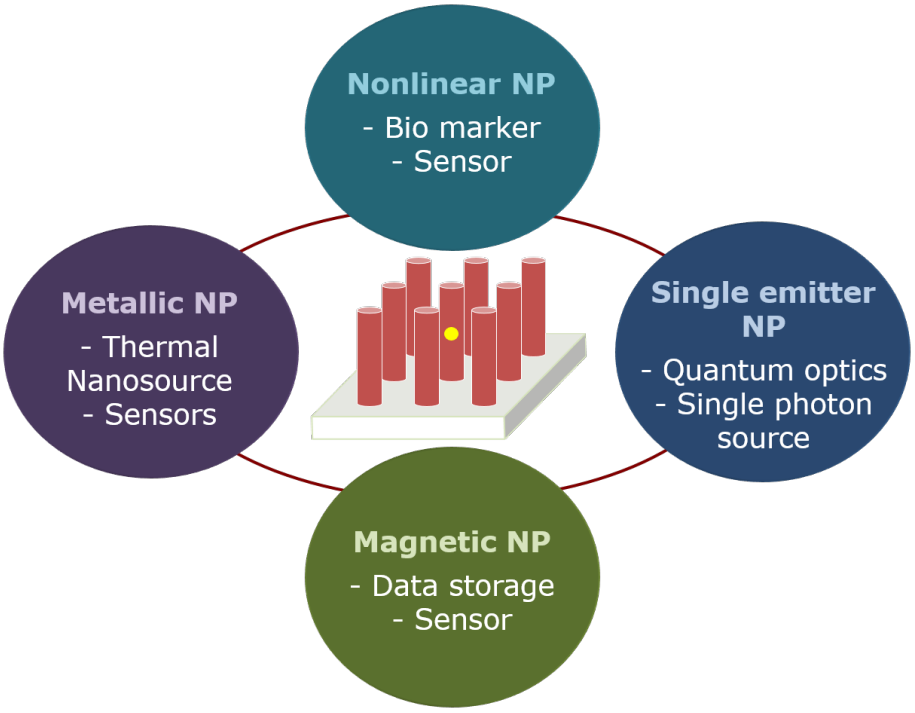

FIGURE 1.4: Illustration of coupling of a single active nanoparticle into a two-dimensional photonic structure. Different kinds of single nanoparticles (quantum emitter, metallic, magnetic, and nonlinear optics) could be coupled for different applications.

Direct laser writing (DLW) is currently one of the most interesting fabrication technologies enabling desired one-, two-, and three-dimensional (1D, 2D, and 3D) structures at sub-micrometer scale [42, 43]. In regular DLW, a femto second laser beam is tightly focused into a photoresist by means of a high numerical aperture (NA) objective lens (OL). Only a tiny volume at the focusing spot is sufficiently polymerized/depolymerized by two- or multi-photon absorption (TPA or MPA) mechanisms. By moving the focus of the laser beam, arbitrary structures can be written into the volume of photoresist. After the development step, desired structures could be obtained.

The TPA-based DLW requires the use of a femtosecond or picosecond laser and a complicated optical system, making it a rather expensive fabrication technique. Recently, we have demonstrated an original method called low one-photon absorption (LOPA) DLW [44,45], allowing one to combine the advantages of both OPA and TPA methods. Indeed, the LOPA method employs a simple, continuous-wave (cw)

and low power laser, as in the case of conventional OPA, but it allows the optical addressing of 3D objects, like the TPA method, by using a combination of an ultralow absorption effect and a tightly focusing spot. Our recent work has demonstrated the capability of the LOPA DLW technique to create desirable multi-dimensional structures on both negative [45] and positive photoresists [46], as well as plasmonic structures [47, 48] using a cw laser at 532 nm-wavelength.

In this thesis, we aim to investigate the use of LOPA-based DLW for the incorporation of various kinds of NP into polymer-based PS and the property enhancement of such structures as well as of the NPs. First, we optimize LOPA-based DLW to become a robust, ideal technique for structuration and characterization of multi-dimensional and multi-functional microstructures. Then, applying this technique, we focus on three different kinds of NP, namely, magnetic NP (MNP) Fe_3O_4, gold NP, and KTP NP. Each of them possesses different properties which can be exploited and enhanced by its coupling with polymer-based PS.

The thesis is organized as follows:

In **Chapter 2**, we introduce the LOPA DLW technique and investigate the thermal effect induced by a CW green laser, which plays a role as a heat assistance for completing the crosslinking process of the photopolymerization of SU8. We demonstrate the fabrication of submicrostructures using LOPA DLW with laser induced thermal effect, also called local post-exposure bake (PEB), and show how it alters the traditional PEB on a hot plate and helps overcome the accumulation effect existing in standard LOPA DLW. By solving the heat equation, in which the laser is considered as a heat source, we explain the working principle of local PEB and the phenomenon observed. Finally, we demonstrate that LOPA DLW with local PEB is an excellent alternative method for TPA method because of the ability to fabricate any desired 1D, 2D and 3D structures of similar quality, but at low cost.

In **Chapter 3**, we implement LOPA DLW to fabricate desired magneto-photonic devices on a photocurable magnetic nanocomposite consisting in superparamagnetic magnetite NPs (Fe_3O_4) dispersed in polymer matrix of negative tone photoresist SU8. We analyse the impact of viscosities of host environments, concentration of MNP, and the preparation time on the quality of the nanocomposite to obtain the

most homogeneous solution. We then employ the LOPA-based DLW to fabricate free-floating magnetic structures and demonstrate their strong response to an applied magnetic field. Different models of magnetic microdevices and micromachines are proposed and realized.

In **Chapter 4**, we report our investigation on the coupling of a single gold NP with a polymer-based PS. Using LOPA DLW with a double step process, we demonstrate the precise incorporation of a single NP to a microstructure as desired. For this, we take advantage of the absorption of materials: strong absorption of NP and low absorption of photoresist. The fabrication of the desired structure is therefore carried out in two steps: first, to identify the position of the NP by LOPA DLW at a very low excitation power, and second, to fabricate the resin structure containing the NP at a higher power. The fabricated samples are charaterized using the same optical setup, and we show an enhancement in the fluorescence signal of the samples, which is explained by a simulation model using the FDTD method.

In **Chapter 5**, we investigate nonlinear KTP NPs and embed them into PSs using LOPA DLW. We use a pulsed laser with the wavelength of 1064 nm, which is integrated into the LOPA setup, to study the nonlinear property of the NPs. First, we prove that KTP NPs do not cause any thermal explosion in polymeric material as gold NPs do, therefore, it is easy to manipulate and incorporate them into structures of any shapes and sizes. The position of the NP in PS can also be controlled. Then, we demonstrate theoretically and experimentally the enhancement of the second harmonic generation (SHG) signal thanks to the coupling of the fundamental light and the PS.

In the last Chapter, we summerize the main results obtained within the frame of the thesis and discuss some prospects for further applications of hybrid structures obtained with LOPA DLW technique.

Chapter 2

Low one-photon absorption direct laser writing with optically induced local thermal effect

2.1 Introduction

In recent years, various fabrication techniques have been proposed and implemented to realize structures at micro and nano scales, opening numerous applications such as micro-machining, optical data storage, nanophotonics, plasmonics, etc. [49–51]. Among those techniques, optical lithography, which includes mask lithography [52, 53], interference or holography photolithography [54–56], and direct laser writing [57–60], is the most popular because of its simplicity, flexibility and capability of producing different kinds of microstructures, addressing a variety of applications.

The fundamental working principle of optical lithography involves the use of a photoresist, a light-sensitive material, which changes its chemical property when exposed to light. Based on the reactions of photoresists to light, they are classified into two types: positive photoresist and negative photoresist. With positive photoresists, the areas exposed to the light absorb one or more photons and become more soluble in the photoresist developer. These exposed areas are then washed away with the photoresist developer solvent, leaving the unexposed material. With negative resists,

exposure to light causes the polymerization of the photoresist chemical structure, which is just the opposite of positive photoresists. The unexposed portion of the negative photoresist is then dissolved by the photoresist developer. Light sources of different wavelengths are used based on the purposes of the fabrication, which involve the absorption mechanisms of the used photoresist. There are two types of absorption mechanisms, namely one-photon absorption (OPA) and two-photon absorption (TPA). The OPA excitation method is an ideal way to fabricate one- and two-dimensional (1D and 2D) thin structures [61]. In this technique, a simple and low-cost continuous-wave (cw) laser operating at a wavelength located within the absorption band of the thin film material is used as the excitation source. Wavelengths in the UV range are commonly used to achieve high resolution [62]. This method is usually applied in mask lithography and interference techniques, where an entire pattern over a wide area is created in seconds. All structures are often realized at the same time; therefore, these techniques are called parallel processes. However, due to the strong absorption effect, light is dramatically attenuated from the input surface. Thus, it is impossible for OPA to address thick film materials or 3D optical structuring. The TPA (or multi-photon absorption) technique presents a better axial resolution. In this case, two low energy photons are simultaneously absorbed inducing an optical transition from the ground state to the excited state of the material, equivalent to the case of linear absorption (OPA). Two-photon absorption is a nonlinear process, which is several orders of magnitude weaker than linear absorption, thus very high light intensities are required to increase the number of such rare events. In practice, the process can be achieved using a pulsed (picosecond or femtosecond) laser. The TPA method is commonly applied for the technique called direct laser writing (DLW), in which a pulsed laser beam is focused into a sub-micrometer spot, resulting in a dramatic increase of the laser intensity at the focusing spot. Hence, TPA-based 3D imaging or fabrication can be achievable [58,59] with high spatial resolution.

Indeed, DLW has been proved to be an ideal way to fabricate sub-micrometric arbitrary structures, offering flexibility, ease of use, and cost effectiveness. As opposed to mask lithography and interference techniques, DLW is a serial process in which a structure is realized by scanning the focusing spot following a desired pattern. Thus any arbitrary 1D, 2D, and 3D periodic or non-periodic pattern can be fabricated on demand.

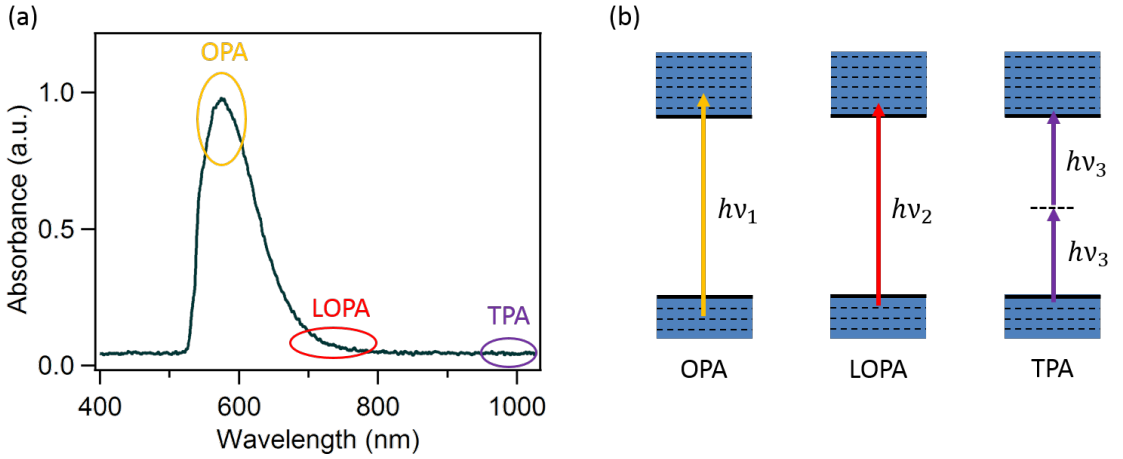

FIGURE 2.1: (a) Illustration of the absorption spectrum of a photoresist. The color rings illustrate three ranges of wavelength corresponding to (b) three absorption mechanisms: standard one-photon absorption (OPA), low one-photon absorption (LOPA), and two-photon absorption (TPA).

However, as mentioned above, TPA-based DLW requires the use of a femtosecond or picosecond laser and a complicated optical system, making it a rather expensive fabrication technique. Recently, we have developped an alternative and innovative method called LOPA (low one-photon absorption) DLW [44, 45], which allows us to combine the advantages of both OPA and TPA techniques. Indeed, the LOPA method employs a simple, cw and low power laser, as in the case of conventional OPA, but it allows the optical addressing of 3D objects, by combining an ultralow absorption effect and a tightly focusing spot. The illustration of an absorption spectrum of photoresist shown in Figure 2.1(a) represents three absorption mechanisms, which are shown in Figure 2.1(b): conventional OPA (yellow ring), LOPA (red ring) and TPA (purple ring), respectively. If a laser beam, whose wavelength is positioned at the edge of the absorption band where the absorption is ultra low, is applied, the light intensity distribution remains almost the same as in the absence of material. In short, by tightly focusing an optical beam inside a thick material with a very low absorption at the operating wavelength, it is possible to address 3D imaging and 3D fabrication, as what realized by TPA method. As compared to the latter one, this LOPA-based DLW is very simple and inexpensive and allows one to achieve very similar results.

It is worth to mention that for most negative photoresists used in optical lithography, the final structures can only be obtained after the post-exposure bake (PEB)

process, which is conventionally implemented by heating the exposed sample using a hot plate at a temperature of about 100°C for several minutes. Excessive heating can lead to the diffusion of photoacids into non-exposed areas, resulting in a loss of resolution [63]. Besides, in the LOPA-based DLW technique, we note that the energy accumulation effect inherently exists due to the linear absorption mechanism, resulting in the apparent non-uniformity of the fabricated structures, especially when the structure period is smaller than 0.5 μm. A dose compensation technique has been proposed and proved to be able to compensate the size difference in the structures [64]. Nonetheless, this technique requires numerous calculation and test in order to find out appropriate dose compensation parameters. In the past decade, thermal effect induced by many kinds of laser has been numerically and experimentally investigated [65–71]. Several reports explained how to use thermal effect to induce the polymerization of polymers and to optimize microstructure fabrication [67–69]. Some others proposed to additionally expose the samples by a laser beam as an alternate heat source for completing the PEB step [65, 71]. Particularly, Seet et al. [65] proposed to use the TPA-based DLW technique in which a femtosecond laser with the wavelength of 800 nm was employed to fabricate microstructures in SU8 photoresist. They observed that structures could be formed without the PEB step. Their results were explained by considering thermal emission of hot electrons during the femtosecond pulse excitation. This is equivalent to a blackbody-type radiation with IR spectral component, which enhances the polymerization of SU8 during the exposure by direct absorption.

In this chapter, we first recall the theory of LOPA-based DLW. We then investigate the thermal effect induced by a cw green laser in the LOPA-based DLW technique, which plays a role as a heat assistance for completing the crosslinking process of the photopolymerization of SU8. By solving the heat equation, in which the laser was considered as a heat source, we explain the working principle of the optically induced thermal effect, also called local PEB. We demonstrate the fabrication of submicrostructures using LOPA DLW local PEB, and show how it alters the traditional PEB on a hot plate, which is in agreement with the theoretical calculation. We prove that it helps overcome the accumulation effect existing in standard LOPA DLW.

2.2 LOPA-based DLW technique

In this section, the vectorial Debye approximation is presented, based on which a new mathematics representation is further established, where the absorption effect of the material is taken into account when a light beam propagates through an absorbing medium. Based on the new evaluation form of vectorial Debye theory, the influence of absorption coefficient of the studied material, the numerical aperture (NA) of the objective lens (OL), and the penetration depth of light beam on the formation of a tight focusing spot are investigated. From that, the crucial conditions for the realization of LOPA microscope and LOPA DLW are established.

2.2.1 Electromagnetic field distribution of a tightly focused beam in an absorbing medium

The mathematical representation of the electromagnetic field distribution in the focal region of an OL was proposed by Wolf in the 1950s [72]. This theory based on the vectorial Debye approximation allows the calculation and prediction of the intensity and polarization distributions of a light beam focused inside a material by a high NA OL. Nonetheless, the influence of material absorption on the intensity distribution and the focused beam shape of a propagating optical wave have not been systematically investigated yet. In this section, the mathematical representation proposed by Wolf [72] will be employed, taking into account the absorption effect of the material through which a focused light beam propagates, in order to investigate the intensity distribution, especially in the focal region.

The schematic representation of light focusing in an absorption medium is shown in Figure 2.2. D is the interface between the transparent material, such as a glass substrate or air, and the absorbing material. To simplify the problem, it is assumed that the refractive index mismatch problem arising at any interface is negligible. d represents the distance between the D interface and the focal plane. The electromagnetic field near the focal plane in Cartesian coordinates (x,y,z) is represented by:

$$\mathbf{E} = -\frac{ikC}{2\pi}\iint_{\Omega}\mathbf{T}(s)A(s)e^{[ik(s_x x+s_y y+s_z z)]}ds_x ds_y, \tag{2.1}$$

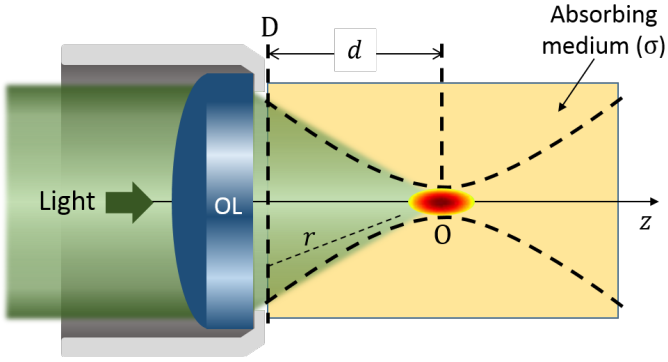

FIGURE 2.2: Schematic representation of a tightly focused light beam inside an absorbing medium. σ is the absorption coefficient of the medium, O is the focal point, D is the interface between the transparent and the absorbing media, r is the distance from a random point on the D plane to an observation point located in the focusing region, d is the distance between the D plane and the focal plane of the objective lens.

where C is a constant, k is the wave number ($k = 2\pi n/\lambda$), n is the refractive index of the absorbing medium, λ is the excitation wavelength, Ω is a solid angle corresponding to the objective aperture, $\mathbf{S} = (s_x, s_y, s_z)$ is the vector of an arbitrary optical ray, and $\mathbf{T}(s) = \mathbf{P}(s)\mathbf{B}(s)$ is a transmission function where $\mathbf{P}(s)$ is the polarization distribution and $\mathbf{B}(s)$ is the amplitude distribution at the exit pupil. $A(s)$ represents the absorption effect of the material, which is expressed as $A(s) = \exp(-\sigma r)$, where σ is the absorption coefficient and r indicates the optical path of each diffracted light ray in the absorbing medium, which is defined as the distance from an arbitrary point located in the D interface to the corresponding observation point, as shown in Figure 2.2. For numerical calculations, r is determined in Cartesian coordinates by:

$$r = \sqrt{(x' - x)^2 + (y' - y)^2 + (d - z)^2}, \tag{2.2}$$

where (x',y',d) gives the position of an arbitrary diffracted light ray located on the D interface. Essentially, Equation 2.1 gives the light distribution resulting from the interference of all light rays diffracted by the exit pupil of the OL. However, in practice, the light intensity and the focus shape at the focus region depend strongly on the absorption term $A(s)$ since light is absorbed by the material in which it propagates and its amplitude decreases along the propagation direction.

The relevant intensity distribution of light, also called point spread function (PSF), in the focal region is defined as:

$$I_{PSF} = \mathbf{E}\mathbf{E}^{*}. \tag{2.3}$$

This theory is applicable for any cases, OPA, LOPA, or TPA. It can be seen that the EM field distribution in the focal region depends on various parameters, such as the polarization of incident light, the NA of OL, the absorption coefficient of the material, etc. It is impossible to have an analytical solution of the light field at the focusing spot of a high NA OL. However, it can be numerically calculated, which will be shown in the next part.

2.2.2 Numerical calculation of point spread function

In order to numerically calculate the light intensity distribution, the I_{PSF} equation was programmed by a personal code script based on Matlab software, with the influence of different input parameters including the absorption coefficient of the studied material, the NA of the OL, and the penetration depth of the light beam.

First, the influence of the absorption effect of the SU8 material, which will be used later for experimental demonstration in the next sections, was investigated. Based on the absorption spectrum of SU8 (see Figure 2.10), three typical wavelengths to calculate the intensity distribution in the focal region were chosen, representing three cases of interest: conventional OPA (308 nm), LOPA (532 nm) and TPA (800 nm), respectively. The corresponding absorption coefficients in each case are: $\sigma_1 = 240720\ \mathrm{m}^{-1}$ ($\lambda_1 = 308$ nm), $\sigma_2 = 723\ \mathrm{m}^{-1}$ ($\lambda_2 = 532$ nm), and $\sigma_3 = 0\ \mathrm{m}^{-1}$ ($\lambda_3 = 800$ nm). The absorption interface (D) was arbitrarily assumed to be separated from the focal point O by a distance of 25 μm, the NA of the OL was chosen to be 0.6, the refractive index n of SU8 is 1.58. As seen in Figure 3(a_1), the incoming light is totally attenuated at the interface D because of the strong absorption of SU8 at 308 nm, which explains why it is not possible to optically address 3D object with the conventional OPA method. However, when using an excitation light source emitting at 800 nm, the absorption coefficient is zero, thus light can penetrate deeply inside the material, resulting in a highly resolved 3D intensity distribution. Note that

the TPA mechanism ($\propto I_{PSF}^2$) is not applied for $\lambda = 800$ nm for this moment. The numerical calculation result derived from the quadratic dependence of the EM field is shown in Figure 2.3(a_3). The size of the focusing spot (full width at half maximum, FWHM) is quite large due to the use of a long wavelength. However, in practice, two photons can be simultaneously absorbed only at an intensity above the polymerization threshold. Therefore, a small effective focusing spot below the diffraction limit can be achieved with the TPA method by controlling the excitation intensity.

The case where the linear absorption is very low (LOPA) was particularly considered. At the wavelength $\lambda = 532$ nm, the absorption coefficient is only 723 m^{-1}, which is much smaller than that at 308 nm. Simulation results show that light can penetrate deeply inside the absorbing material without significant attenuation thanks to this very low linear absorption. As shown in Figure 2.3(a_2), the light beam can be tightly confined at the focusing spot, which can then be moved freely inside the thick material, exactly as in the case of $\lambda = 800$ nm (transparent). Furthermore, LOPA requires a shorter wavelength as compared with TPA, the focusing spot size (FWHM) is therefore smaller. The diagram depicted in Figure 2.3(a_4) shows clearly the difference of the intensity distribution along the optical axis of the three excitation mechanisms. It is important to note that there is no intensity threshold in the case of LOPA, because it is a linear absorption process. Therefore, LOPA requires a precise control of light dose in order to achieve high resolution optical addressing.

The NA of OL is also an important parameter to be taken into account for LOPA case. It was demonstrated that the use of a high NA OL is a crucial condition. The intensity distributions at the focusing spot obtained with OLs of different NA values (with the same low absorption coefficient $\sigma_2 = 723$ m^{-1}) are shown in Figure 2.3(b). It is clearly seen that with an OL of low NA (NA = 0.3), the light beam is not well focused, resulting in low contrast intensity distribution between the focal region and its surrounding. Therefore, the LOPA based microscopy using a low NA OL cannot be applied for 3D optical addressing. However, in the case of tight focusing (for example, NA = 1.3), the light intensity at the focusing spot is a million time larger than that at out of focus, resulting in a highly resolved focusing spot (Figures 2.3(b_3)). For all the above calculations, it can be concluded that the

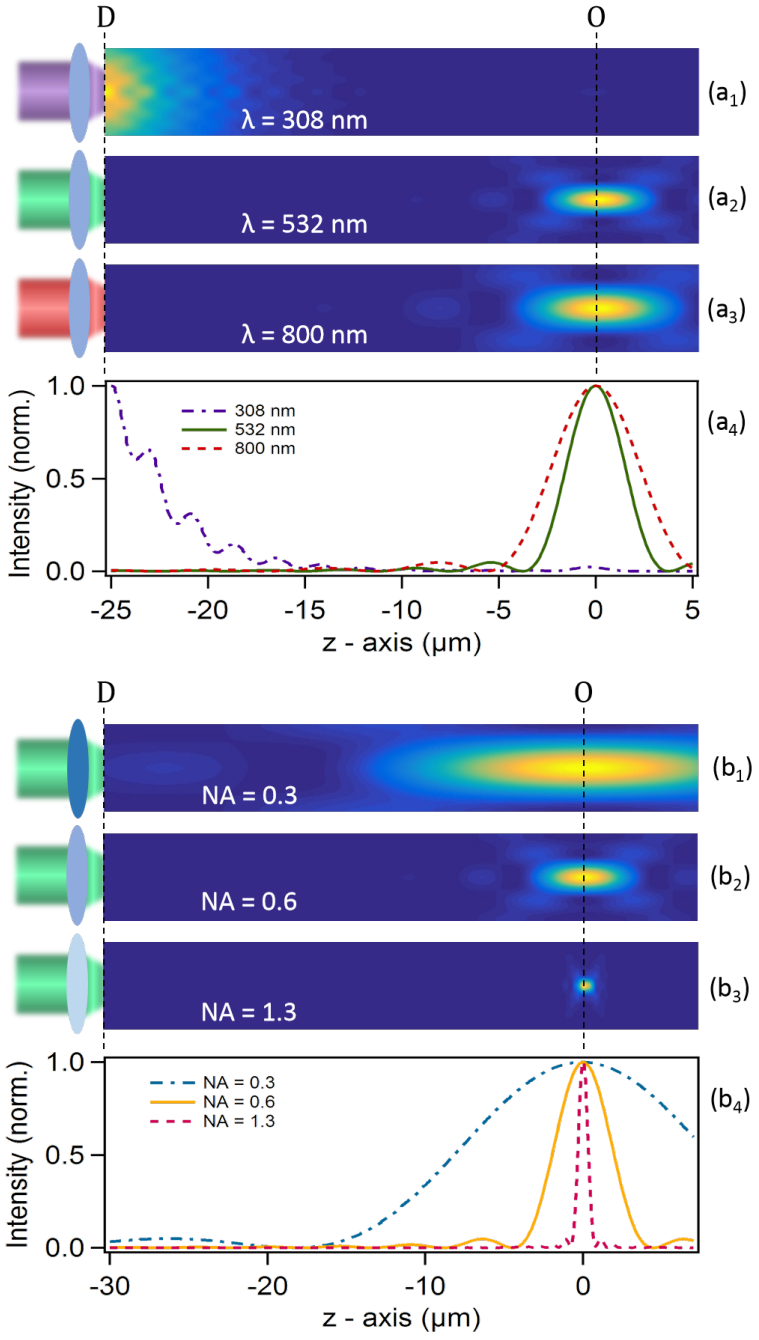

FIGURE 2.3: (a) Numerical calculations of light propagation inside SU8, by using different wavelengths, (a_1) 308 nm, (a_2) 532 nm, and (a_3) 800 nm, respectively. (a_4) Intensity distributions along z-axis of the light beams shown in (a_{1-3}). In this calculation, NA = 0.6, refractive index $n = 1.58$, and $d = 25$ μm. (b) Propagation of light ($\lambda = 532$ nm) inside SU8, with (b1) NA = 0.3, (b2) NA = 0.6, and (b3) NA = 1.3, respectively, $d = 30$ μm. (b4) Intensity distributions along z-axis of the light beams shown in (b_{1-3}).

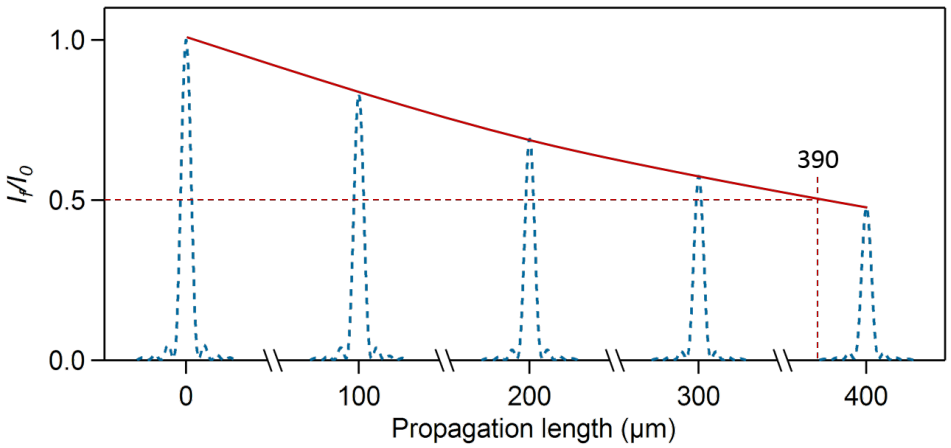

FIGURE 2.4: Red curve: normalization of intensity (I_f/I_0) at the focusing spot as a function of the propagation length. I_f and I_0 are the intensities obtained with and without absorption medium, respectively. Dot curves: zoom on intensity profiles of the focusing spot along the optical axis, calculated at different propagation length. The results are simulated with: σ = 723 m$_{-1}$; λ = 532 nm; NA = 1.3 (n = 1.58).

LOPA based microscopy is promising for the realization of 3D imaging and 3D fabrication, similarly to what could be realized by TPA microscopy. By using the LOPA technique, 3D fluorescence imaging or fabrication of 3D structures can be realized by moving the focusing spot inside the material since fluorescence (for imaging) or photopolymerization (for fabrication) effects can be achieved efficiently within the focal spot volume only. It is worth noting that in LOPA technique, the absorption exists, even if the probability is very small, the penetration depth is therefore limited to a certain level. This effect exists also in the case of TPA, but it is more important for LOPA. Figure 2.4 represents the maximum intensity at the focusing spot as a function of the penetration length. For this calculation, the ultralow absorption coefficient of SU8 at λ = 532 nm, σ = 723 m^{-1} was considered. At the distance of 390 μm, the intensity was found to decrease by half with respect to that obtained at the input of absorbing material (D interface). This penetration depth of several hundred micrometers is fully compatible with the scanning range of piezoelectric stage (typically, 100 μm for a high resolution), or with the working distance of microscope OL (about 200 μm for a conventional high NA OL). In summary, in order to realize the LOPA based microscopy, two important conditions are required: i) ultra low absorption of the studied material at the chosen excitation wavelength,

and ii) a high NA OL for tight focusing of the excitation light beam.

3D PCs were successfully fabricated by means of LOPA DLW [45]. Figure 2.5 shows a 3D woodpile and a chiral structure created using LOPA DLW. The woodpile structure consists of 20 stacked layers, each layers consists of parallel rods with period a = 1.5 μm. The spiral structure was well created and is as good as those obtained by TPA DLW. The structures features are well separated, layer by layer, in horizontal and in vertical directions. The feature sizes are about 300 nm (horizontal) and 650 nm (vertical). The smallest feature size can reach 150 nm corresponding to the smallest lateral cross-section of rod. The best quality of the fabricated structure obtained when the line width of rods is about of the voxel standard size (lateral and axial cross-section size is about 220 nm and 680 nm, respectively. The corresponding aspect ratio (axial/lateral) is about 3.

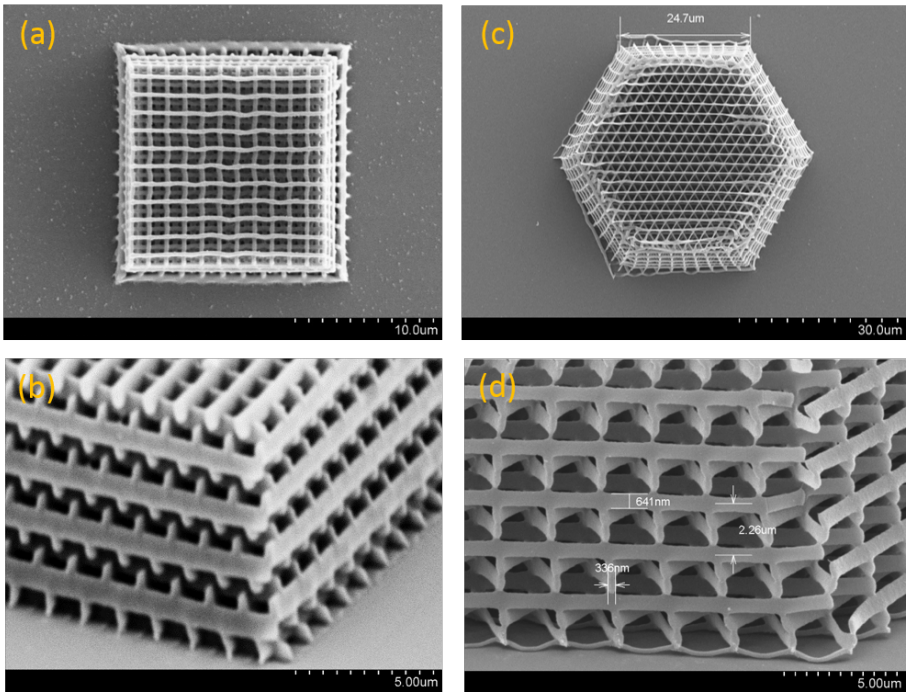

FIGURE 2.5: (a-b) SEM images of a woodpile structure fabricated with the following parameters: distance between rods = 1.5 μm; distance between layers = 0.7 μm; number of layers = 20; laser power P = 4 mW and scanning speed v = 1.5 μm/s. (c-d) SEM images of a chiral structure. Fabrication parameters: lattice constant a = 2 μm; distance between layers = 0.75 μm; number of layers = 28; laser power P = 2.8 mW and scanning speed v = 1.34 μm/s.

However, there are still some existing drawbacks in structures fabricated by LOPA DLW, such as the energy accumulation effect, shrinkage effect, or high aspect

ratio [45]. In the next section, the thermal effect induced by a cw green laser in the LOPA-based DLW technique, which plays a role as a heat assistance for completing the crosslinking process of the photopolymerization of SU8, is investigated. This thermal effect will help overcome those drawbacks and significantly improve the quality of structures fabricated by LOPA DLW.

2.3 Theoretical model of optically induced local thermal effect

In this section, by solving the heat equation, in which the laser was considered as a heat source, we explain the working principle of the optically induced thermal effect, also called local PEB.

First, the heat distribution in the laser-heated SU8 is calculated. When a laser beam propagates through an absorbing material, the temperature distribution in the material can be derived from the equation of heat [73]:

$$\rho C_p \frac{\partial T}{\partial t} = k\nabla^2 T + S, \tag{2.4}$$

where ρ is the mass density (kg.m^{-3}), C_p is the heat capacity (J.kg^{-1}.K^{-1}), k is the thermal conductivity (W.m^{-1}.K^{-1}), and the S(W.m^{-3}) term is calculated as a variation of light intensity along the propagation direction:

$$S = -\left(\frac{\partial I(r,z)}{\partial z}\right)_r = \mu_{\text{abs}}(1-R_c)I(r,z)\exp(-\mu_{\text{abs}}z), \tag{2.5}$$

where *I(r,z)* is the laser intensity, μ_{abs} is the absorption coefficient of the material, and R_c is reflection coefficient. In our case, the light beam is focused into photoresist by a high NA OL. The intensity distribution of the focused laser beam is calculated by:

$$I(r,z) = I(0,0)I_{\text{OPA}}, \tag{2.6}$$

where r is the radial distance from the beam axis, z is the axial distance from the center of the focusing spot, $I(0,0)$ is the peak intensity at the center of focusing spot ($r = 0$, $z = 0$) and I_{OPA} is the normalized intensity distribution of focused

light in the focal region, which is rigorously calculated by using the vector Debye method presented in Section 2.2. By using finite element method with Matlab PDE solver, Equation 2.4 was numerically solved to characterize the optically induced heat profile. The optical intensity distribution at the focal region of a high NA OL for the $xz-$plane and corresponding induced temperature profile, obtained after 50 μs of exposure, are shown in Figure 2.6. Due to the absorption of the photoresist and thanks to the optical intensity distribution (Figure 2.6(a)), a temperature distribution is produced at the focusing region (Figure 2.6(b)). It can be seen that the normalized heat distribution is broader than the optical intensity distribution. However, looking closer at the peak of the temperature profile, we can see that there is only a tiny area where local temperature can surpass the effective temperature for PEB, *i.e.*, 95°C where the complete crosslinking reaction takes place (see inset of Figure 2.6(c)). The size of this area is even smaller than the full-width at half maximum of the optical focusing spot, suggesting that a solidified structure made by optically induced thermal effect could be smaller than the diffraction limit, which usually limits the resolution of DLW technique.

The resolution of the DLW technique along the propagating direction of the laser beam (z-direction), *i.e.*, the voxel aspect ratio, plays an important role in 3D fabrication. As seen in Figure 2.6(a) which shows theoretical calculations of light intensity distribution at the focal region, the longitudinal ($z-$axis) size of the focusing spot is about 3 times larger than the transverse size ($x-$axis). Meanwhile, the temperature distribution along the longitudinal direction ($z-$axis) is quite similar to that of transverse direction ($x-$axis, or $y-$axis) as observed in Figure 2.6(b). It means that the fabrication based on optically induced thermal effect could have an isotropic resolution for 3D structures.

We note that the induced temperature is very sensitive to the exposure dose. Indeed, when a small area of material is strongly excited, the temporal thermal balance is immediately broken due to the change of thermal constants. We also analysed thermal profiles for different values of thermal constants, assuming that we excite a small area of 200 nm-diameter to reach a temperature above 95°C. The thermal conductivity of the exposed part will be reduced from 0.3 to 0.25. The simulation results show that the thermal profile increases slightly and become sharper as shown in Figure 2.7(a). Furthermore, we found theoretically that the absorption coefficient

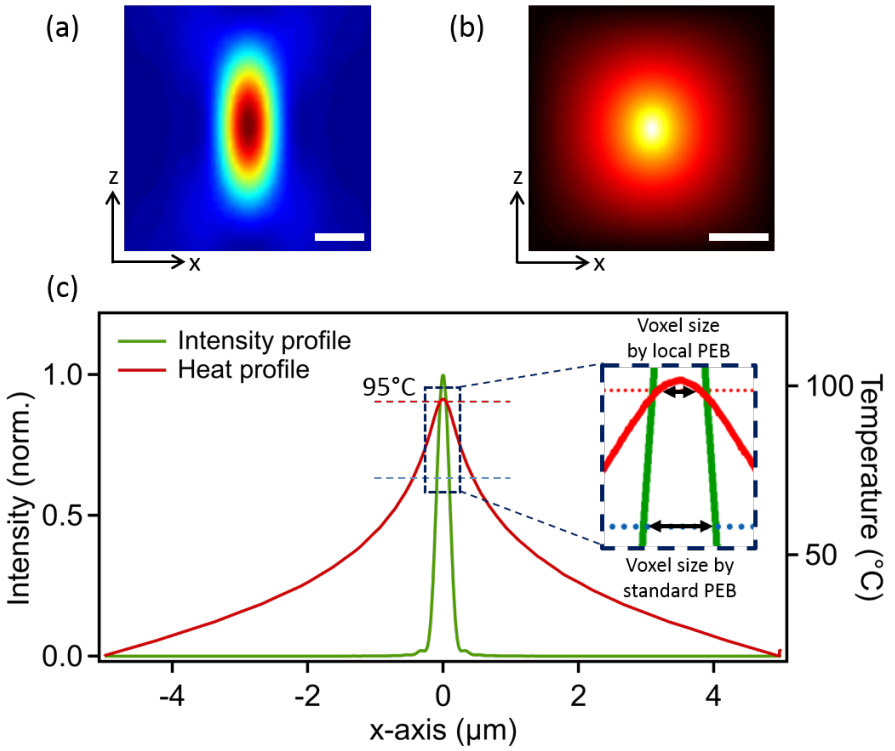

FIGURE 2.6: (a) Theoretical calculation of light intensity distribution at the focal region of a high NA OL for xz–plane. (b) Corresponding heat distribution inside excited material for xz–plane. (c) Cross section of heat profile and light intensity distribution at the focal region for x–axis. The simulations were realized with following parameters: $\rho = 1200$ kg.m^{-3}, $C_p = 1200$ J.kg^{-1}.K^{-1}, $k = 0.3$ W.m^{-1}.K^{-1}, $R_c = 0$, $\mu_{\text{abs}} = 723$ m^{-1}, $S \approx 10^{14}$ W.m^{-3} corresponding to a laser power of 4 mW, and the initial temperature of material is 20°C.

(μ_{abs}) is also an essential parameter to define the transfer rate of the energy from the focusing spot to the absorbing medium. Therefore, a minor modification of (μ_{abs}) can lead to a significant change in the thermal response, *i. e.* induced temperature, as shown in Figure 2.7(b). However, the absorption coefficient of SU8 at the writing wavelength ($\lambda = 532$ nm) does not significantly change for temperature range of 50°C–95°C. Therefore, by limiting the laser power or exposure time to keep the induced temperature in this range, the absorption coefficient is constant. Only, if we extend the exposure process, the temperature at the focusing spot will progressively increase and the cross-linked area will be expanded accordingly.

Solving the heat equation 2.1 with the depth taken into account, we calculated the dependence of the locally induced temperature on the depth of the focusing spot inside the material. Due to the ultra-low absorption of SU8 at the wavelength of

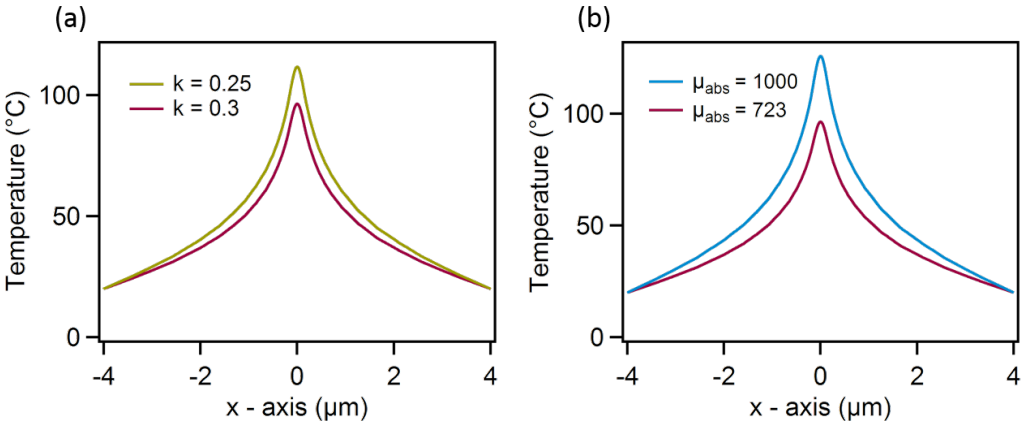

FIGURE 2.7: (a) Comparison of temperature distributions obtained in two possible cases: i) thermal conductivity is 0.3 for whole film (red), and ii) thermal conductivity is 0.25 at focusing center with a diameter of 200 nm and 0.3 on the remaining part (green). The simulations were realized for only x-axis with following parameters: (ρ = 1200 kg.m^{-3}, C_p = 1200 J.kg^{-1}.K^{-1}, μ_{abs} = 723 m^{-1}, the laser power of 4 mW. (b) Comparison of temperature distributions in two cases: i) absorption coefficient is constant (μ_{abs} = 723 m^{-1}) for whole region (red), and ii) absorption coefficient at focusing center with a diameter of 100 nm is μ_{abs} = 1000 m^{-1} and that of the remaining part is μ_{abs} = 723 m^{-1} (blue).

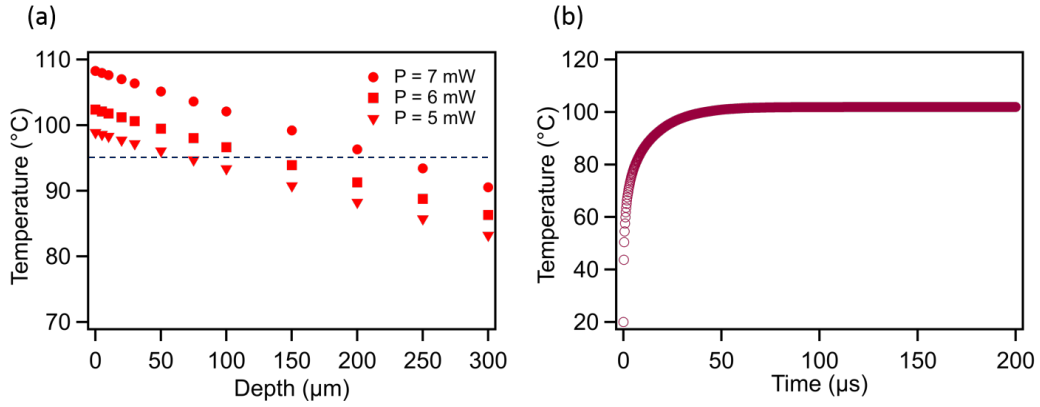

FIGURE 2.8: (a) Simulation result of local peak temperature at different values of focusing depth with different laser powers. (b) The evolution of optically induced temperature as a function of exposure time at the laser power of 5 mW.

532 nm (μ_{abs} = 723 m^{-1}), light can be tightly focused inside the material while the intensity does not decrease much, resulting in a photo induced thermal effect with high temperature even at large penetration depth. This is evident in the calculation result shown in Figure 2.8(a), which presents the local peak temperature as a function of depth with different laser powers. Obviously, the deeper the focusing spot

goes inside the material, the lower the temperature is due to the decrease of the light intensity. However, the induced temperature changes only slightly, for example, with a laser power of 5 mW (intensity of 0.11 W μm^{-2}), the temperature decreases by only 5°C (from 99°C to 94°C) when the focusing spot goes from the interface to a depth of 75 μm. The higher the used intensity is, the deeper the focusing spot can go inside the material with the peak temperature remaining above the required temperature for PEB. Thus, it is possible to fabricate 3D structures using LOPA DLW with local PEB.

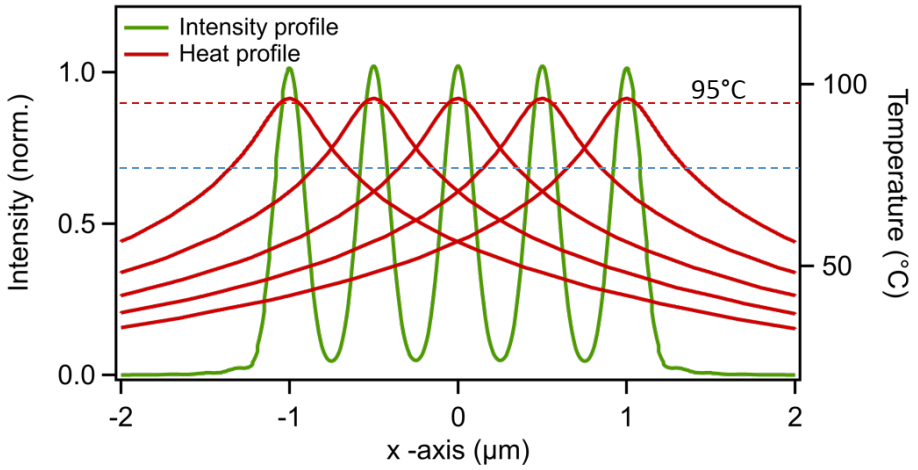

FIGURE 2.9: Intensity distribution (green curve, corresponds to the left axis) and temperature distributions (red curves, correspond to the right axis) of multiple exposures. The red dotted line (corresponds to the right axis) represents the global temperature by the hot plate; The blue dotted line represents the iso-intensity.

More importantly, LOPA DLW with local PEB can help overcome some drawbacks existing in traditional LOPA DLW. Figure 2.9 illustrates the working principle of traditional PEB on a hot plate (green curves) and optically induced local PEB (red curves). In the first case, heat is broadly provided, thus the fabricated structure (voxel size and shape) depends critically on the exposure dose. When the exposures are made too close, the energy will be accumulated, leading to the effect that the central voxel possesses a largest size (due to the most accumulated energy) and the voxels sizes gradually reduce from the center to the edge. Solidification of structure resulting from photothermal process differs from that of photochemical process in term of accumulation. In the second case, although the energy is still accumulated, the voxel size is determined by the local PEB, which resulting from the optically

induced heat distribution. The red curves in Figure 2.9 show the temperature profile generated by a focused laser spot (laser power of 4 mW, or intensity of 0.088 W μm^{-2}) inside the exposed area. With moderate excitation power, the induced temperature is just enough to complete the PEB step and does not damage the fabricated structure. Furthermore, the induced temperature is not only localized but also temporal, *i.e.*, during the exposure time only. In our DLW method employing a cw laser, we found theoretically that the induced temperature at the focusing spot rises up quickly as a function of exposure time and reaches a stable temperature (beyond 100°C) after several 10 μs, depending on the exposure power (see Figure 2.8(b)) and remains at that temperature during the exposure time, which is in between 10 ms and 1000 ms. This time scale is consistent with previous heat models on other polymer materials [74]. Figure 2.9 shows the integrated light intensity profile resulting from multiple exposures at a 500 nm period (green curve) and heat profiles generated temporally during each exposure time. Thus, even when the light energy is accumulated in case of LOPA-based DLW, the localized and temporal temperature profile is the same for every exposure without accumulation, resulting in the uniform solid voxels array. We note that, using a femtosecond laser, the induced temperature increases quickly to one million degrees but also decreases quickly to room temperature [75] (the heating time is the same as the femtosecond pulse duration), which is not suitable to solidify the photoresist. Therefore, DLW using a femtosecond laser does not induce such thermal effect, except the result reported in reference [65], where the femtosecond pulse excitation induced high temperature that plays a role as a blackbody source emitting IR light, which enhances the polymerization of SU8 during the exposure by direct absorption. We also note that the voxel size increases as the exposure time rises since the voxel size depends on both the exposure dose (exposure time) and the PEB time. It is also worth noting that, when using traditional PEB, the exposure step and PEB step are separated, which means the photoacids have sufficient time to diffuse into exposed region, whose overlap is then fixed by PEB, leading to non-uniform structures. On the contrary, optically induced PEB occurs simultaneously with optical exposure, providing a highly localized immediate fixing in a small region inside the focusing spot which is not affected by the diffusion. In summary, we have demonstrated theoretically the working mechanism of the optically induced thermal effect by solving a heat equation. The results prove that it is possible to apply this effect to LOPA-based DLW technique to create 1D,

2D and 3D microstructures, and to optimize the quality of fabricated structures. In the next section, we will implement the experiments to confirm the theoretical calculation results.

2.4 LOPA-based DLW by local PEB

2.4.1 LOPA-based DLW system

The LOPA technique can be used for all 3D applications, including 3D imaging and 3D fabrication. As mentioned in section 2.1, two conditions are required: a photoresist that presents an ultralow absorption at the wavelength of the excitation laser, and a highly focusing confocal laser scanning (CLSM) system. For the first condition, SU8, a commercial photoresist, is an ideal candidate, thanks to its ultralow absorption in the visible range, in particular at 532 nm (Figure 2.10), which is the wavelength of a very popular and low cost solid state frequency-doubled neodymium laser. By using a high NA oil-immersion OL of NA = 1.3 to focus a laser beam into the photoresist, the second condition is then satisfied.

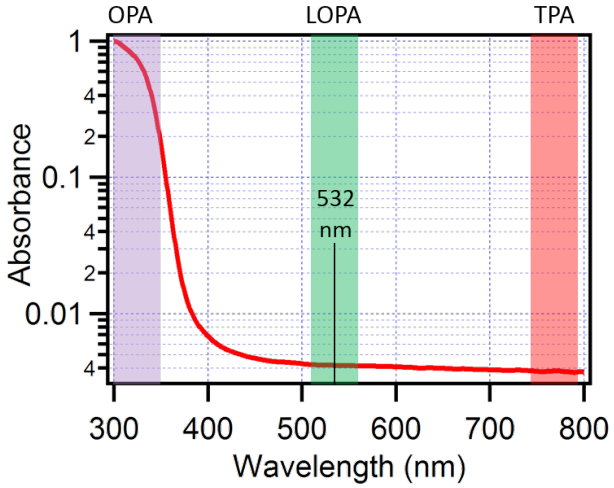

FIGURE 2.10: Absorption spectrum of SU8 photoresist. The color bars indicate three cases: OPA (purple bar), LOPA (green bar), and TPA (red bar). To demonstrate LOPA DLW, a laser operating at 532 nm is used.

In order to implement the LOPA DLW technique, a confocal optical system illustrated in Figure 2.11 was built. In this system, a cw laser operating at 532 nm

is used. In order to adjust the power of the laser beam to the sample, we used a half-wave plate ($\lambda/2$) and a polarizer (PBS). By rotating the half-wave plate, the power of the laser beam can be precisely modified. A powermeter (not shown in the figure) is used to measure the power of the laser beam. The laser beam is directed and collimated by a set of lenses and mirrors. In order to realize mapping or fabrication, samples are mounted on a 3D piezoelectric actuator stage (PZT), which is controlled by a LabVIEW program. A quarter-wave plate ($\lambda/4$) placed in front of the OL allows one to transform the beam of linear polarization to circular polarization before it enters the OL. The laser beam is strongly focused to the sample via an OL with high NA (1.3). The time of exposure of the sample to the laser beam is determined using an electronic shutter, which is also controlled by a LabVIEW program. The fluorescence signal emitted by the samples is collected by the same OL, filtered by a 580 nm long-pass filter (to cut off the excitation wavelength of 532 nm), and detected by an avalanche photodiode (APD). The inset of Figure 2.11 shows the simulation result of the light intensity distribution at the focusing region of the OL. The maximal intensity was normalized and three iso-intensities are shown. This suggests the evolution of the structure size and shape, which is linearly dependent on the exposure doses (excitation power and exposure time) and can be controlled by applying an appropriate dose [45]. By scanning the focusing spot, we can obtain desired multi-dimensional structures, which are similar to those realized by the commercial TPA-based DLW.

Below we describe in detail some optical components of the setup, which are used in all experiments of the thesis.

Laser source: In this work we used a cw laser operating at 532 nm for fabrication of PSs in SU8 photoresist. A pulsed laser operating at 1064 nm was used for second harmonic generation (SHG) measurement of KTP NPs (details in Chapter 5). Besides, cw 532 nm laser source was used for all system characterizations (confocal system, data acquisition calibration, etc.) using a single gold nanoparticle (Au NP).

- Pulsed laser (JDSU): 1064 nm wavelength; maximum averaged power: 300 mW; pulse duration: 1 ns, repetition rate: 24.5 kHz.

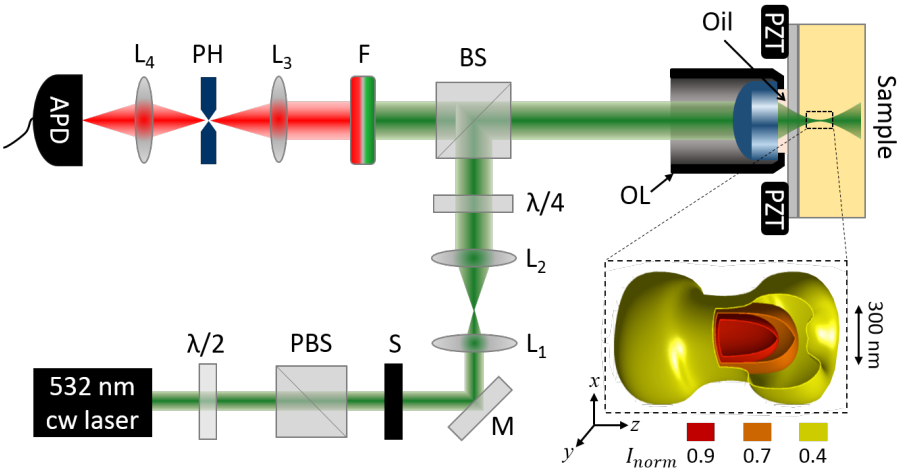

FIGURE 2.11: Experimental setup of the LOPA-based DLW technique. PZT: piezoelectric translator, OL: oil immersion microscope objective, $\lambda/4$: quarter-wave plate, $\lambda/2$: half-wave plate, BS: beam splitter, PBS: polarizing beam splitter, M: mirror, S: electronic shutter, L_{1-4}: lenses, PH: pinhole, F: 580 nm long-pass filter, APD: avalanche photodiode. Inset: Simulation result of intensity distribution at the focus region of a high NA OL. Three surfaces correspond to three isointensities, 0.4; 0.7; and 0.9, respectively. The optical axis of the OL is z-axis.

- Continuous wave laser (Oxxius): frequency-doubled Nd-YAG laser, 532 nm wavelength, maximum power: 300 mW, coherence length: 300 m; pointing stability: 0.005 mrad/C.

Translation system: In order to precisely translate the sample relatively to the focusing spot during fabrication, DLW requires a high-resolution piezo-based translation PZT system. In our experimental setup, a high-precision nanopositioning system for up to six degrees of freedom is used (P365 PIMars Nanopositioning Stage - Physik Instrumente). This piezo-based translation system offers a large travel ranges of 300 × 300 × 300 (μm^3) and very high precision. According to the company specification, this device shows a resolution of 1 nm when operating in open-loop and 2 nm in close-loop. The stability for an accuracy of about 10 nm can maintain within a long period of up to 5 hours. However, the precision and the stability is very sensitive to the mechanical vibration and ambiant temperature. We keep the PZT system remote from mechanical noise source and the room temperature was maintained within 20-25°C.

Detection system: The detection system is used for calibration and optical characterization of the DLW system. The emission of the fluorescent object (glass/photoresist interface, NPs) is collected by the OL and sent to the detection system. A filter is used to selectively transmit the fluorescent wavelengths while blocking the original excitation wavelength. The fluorescent beam is focused into a small spot where a pinhole with a diameter of 100 μm is placed so that only the fluorescence from the focusing point of the OL can pass through the pinhole and all out-of-focus light are blocked. After passing the pinhole, fluorescence is detected by an APD (SPCM-AQRH-13 Perkin Elmer). Optical-electrical signal transformation is performed by a PCI card (6014 M-series, NI). The fluorescence images are then produced by computer software (Labview, Igor).

2.4.2 Sample preparation

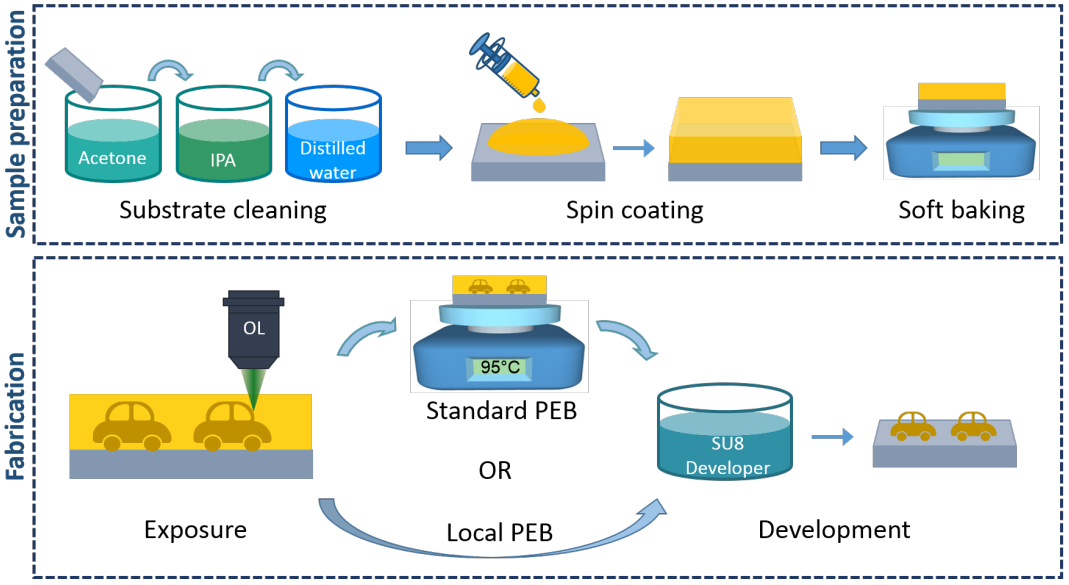

FIGURE 2.12: Sample preparation and fabrication processes (with standard and local PEB.)

The sample preparation process is shown in Figure 2.12 (top), which consists of two steps:

- Substrate cleaning: Glass substrates are treated with a solvent before spin coating.

- Spin coating of resins: SU8 photoresist is deposed on the cleaned glass substrates for fabrication.

2.4.2.1 Substrate cleaning

The glass subtrates must be treated prior to spin coating in order to remove all the contamination. The cleaning process is carried out as follow:

- The glass substrates are dipped in acetone and ultra-sonicated for 10 minutes to remove impurities on their surface.
- Then they are soaked in isopropanol (IPA) to wash away acetone and rinsed in distill water.
- They are dried using Ni gun.
- The glass substrates could be baked at 200°C in order to evaporate all the water left on the surface (optional).

2.4.2.2 Deposition of SU8

Spin coating is a procedure used to deposit uniform thin films to flat substrates. Usually, a small amount of coating material is applied on the center of the substrate. The substrate is then rotated at high speed in order to spread the coating material by centrifugal force.

In this work, we use SU8 2000 as the coating material. SU8 2000 is a high contrast, epoxy based photoresist designed for micromachining and other microelectronic applications, where a thick, chemically and thermally stable image is desired. SU8 2000 is an improved formulation of SU8, which has been widely used by MEMS producers for many years. The use of a faster drying, more polar solvent system results in improved coating quality and increases process throughput. SU8 2000 is available in twelve standard viscosities. Film thicknesses of 0.5 to $>$ 200 microns can be achieved with a single coat process.

For 1D and 2D structures, SU8 2000.5 and 2002, which give a layer thickness of 0.5 and 2 μm, are used. For 3D structures, other types of SU8 at higher viscosity, for example SU8 2005 or 2025, are required. Before spin coating the SU8 layer used for fabrication, we can create a buffer layer in order to assure the firm formation of the structure. The buffer layer is formed by spin coating a SU8 2000.5 layer, then hard baking in the UV oven for 30 seconds.

After spin coating, the samples are put on a hot plate at 65°C and 95°C (Soft baking step). The soft baking time depends on the types of SU8 used. The samples must be protected from the light until the exposure process to avoid the solidification of the photoresist.

The parameters used for the spin coating step and soft baking for different types of SU8 are described in Table 2.1 below:

TABLE 2.1: Sample preparation of SU8 2000 series

Type	Speed (rpm)	Acceleration (rpm/s)	Time (s)	Soft bake (min.) 65°C	Soft bake (min.) 95°C	Thickness (μm)
SU8 2000.5	2000	300	30	1	2	0.5
SU8 2002	2000	300	30	1	2	2
SU8 2005	2000	300	30	2	4	5
SU8 2025	2000	300	30	3	6	25

2.4.3 Fabrication process

The fabrication process following two ways (traditional PEB and local PEB) is described in Figure 2.12 (bottom). It consists of three main steps: exposure with the 532 nm cw laser, post exposure bake, and development.

2.4.3.1 Exposure process

The confocal optical system of the DLW technique is presented in Figure 2.11 and described in Section 2.4.1. Before writing the structure on the photoresist, the interface between the glass substrate and the photoresist layer must be determined. To

determine the interface, we use a very low laser power (several μW) to prevent the solidification of the photoresist prior to the writing step. The laser beam is scanned along an arbitrary vertical (xz or yz) plane (in fact, the PZT will be shifted instead of the OL) and the fluorescence signal can be collected by the APD. We obtain a fluorescence image which indicates exactly the position of the photoresist layer. This step allows us to precisely write the structure at the desired position.

After that, we increase the laser power to several mW to fabricate desired structures. The focusing spot is scanned inside the photoresist along an arbitrary path programmed with the Labview software to create any microstructures. The excitation power and exposure time are important parameters, which directly determine the characteristics of fabricated structures and can be controlled by the fabrication program.

2.4.3.2 Post exposure bake

As shown in Figure 2.12, depending on which way we choose to fabricate our structures: standard PEB or local PEB, the PEB step can be either carried out or skipped. For standard PEB, which takes place directly after exposure, the sample is put on a hot plate at 65°C for 1 minute and then at 95°C for 3 minutes to complete the polymerization process. For local PEB, the heating with hot plates is skipped.

2.4.3.3 Development process

After that, the development step is carried out. SU8 2000 photoresist has been designed for use in immersion, spray or spray-puddle processes with MicroChem's SU8 developer. Here we rinse the sample in a bath of SU8 developer for 3 minutes, then wash with Isopropanol (IPA) for 1 minute and finally soak in distilled (DI) water.

2.4.4 2D and 3D microstructures fabrication enabled by LOPA DLW with local PEB

2.4.4.1 Small featured size structures

For the demonstration of local PEB, we fabricated two sets of 2D structures, each set contains pillar arrays written at different doses (by varying the laser power and the writing speed). One set was realized following the traditional process, *i.e.*, after exposure, the sample is post-baked for 1 minute at 65°C and then 3 minutes at 95°C using hot plate. For the other set, the PEB step was skipped, which means that the exposure process was followed directly by the development process, in which the samples were bathed in SU8 developer and rinsed by IPA and DI water to remove the non-cross-linked resist. All fabricated structures were examined by optical microscopy and scanning electron microscopy (SEM). Figure 2.13 shows the SEM images of two sets of pillar arrays (set 1: traditional PEB; set 2: local PEB; separation between pillars = 2 μm) fabricated at different exposure doses. The fabrication of each pillar was realized by moving the focusing spot through the SU8 film (the film thickness is 0.5 μm and the moving distance was 2 μm). The lowest writing velocity used was 1 μm/s since fabrication at lower speed was time consuming. Conventionally, PEB is an obligatory step in optical lithography dealing with negative photoresist, since the crosslinking reaction takes place mostly during PEB [63, 76]. However, it is observed that structures were obtained even when the PEB step was skipped, which suggests that the PEB was already achieved during light exposure. The heat source can be apparently referred to the laser, which is tightly focused and absorbed by the material. The absorbed energy locally induces the necessary heat for the crosslinking process. We found that, without PEB, polymerized structures were obtained only if the laser power is larger than a certain value. Indeed, with a laser power of 2 mW (intensity = 0.044 W.μm^{-2} at the focusing plane), most structures were created in set 1 (with PEB), while no structure was obtained in set 2 (no PEB). From 3 mW, structures were obtained without PEB step, only at low scanning velocity (1 μm/s).

The above investigation suggests that, in LOPA-based DLW process, the intense light intensity at the focusing spot induces a hot spot with a temperature higher

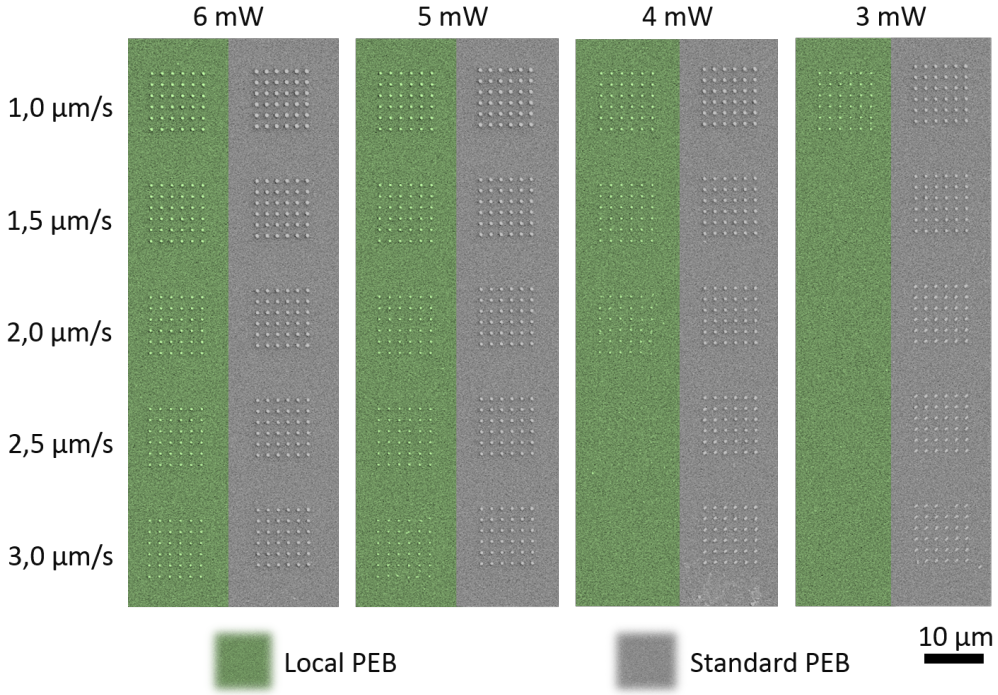

FIGURE 2.13: SEM images of structures fabricated by using LOPA DLW with different exposure doses (the excitation power and writing velocity are varied). Two sets of structures are fabricated with the same exposure parameters: one is directly developed after exposure (local PEB), and the other is developed after a standard PEB process using a hot plate.

than 95°C, which then locally solidifies the SU8 photoresist. This observation hence confirms the theoretical calculation results presented in Section 2.3.

A comparison between the sizes of pillars fabricated in two sets of pillar fabricated with standard and local PEB was made and shown in Figure 2.14. Figure 2.14(a) shows the pillar size as a function of the writing velocity with different laser powers, and Figure 2.14(b) presents two structures fabricated at the same dose (same laser power and writing velocity), one with (standard PEB) and the other without PEB (local PEB). It can be clearly seen that, for the same dose, the pillars fabricated without PEB are smaller than those fabricated with PEB. Due to the fact that the structures are not formed at low power (low light intensity), the applied laser power or intensity must be above a threshold in order to induce enough heat for the crosslinking process, and this threshold should be higher than that of standard LOPA (with PEB) for complete photopolymerization. The calculation of induced temperature presented in Section 2.3 confirms this experimental result, *i.e.*,

above a temperature of 95°C (effective temperature for PEB) induced by the laser at the focal spot, the polymerization is fully completed, leading to the formation of structures. Furthermore, observing the temperature profile (Figure 2.6 inset), only a small region inside the exposed area is heated at the temperature above 95°C, where the complete crosslinking reaction takes place. As a consequence, the voxel size is smaller than that obtained in the case of standard PEB. We also see that the size of voxels increases with the exposure time and laser power. This increment comes from the growth of crosslinking reaction due to the induced temperature. Obviously, we can control precisely the laser power and the exposure time to obtain desired structures.

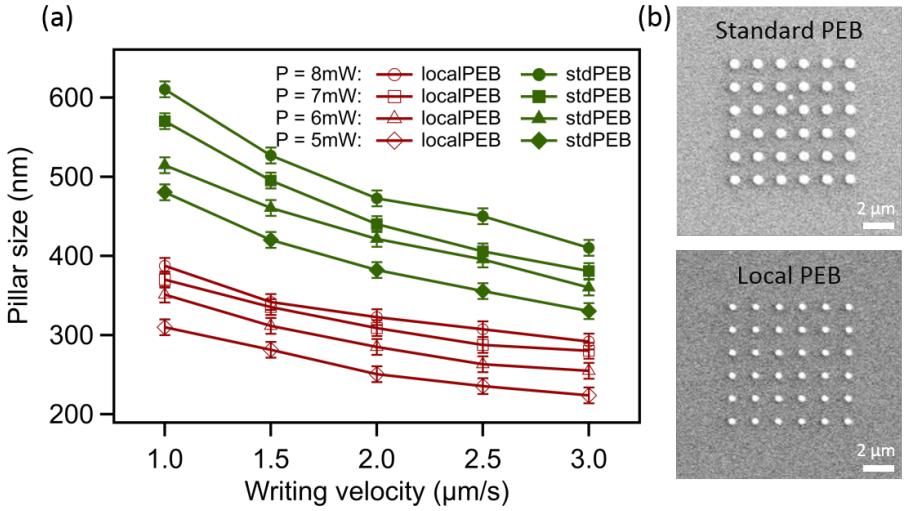

FIGURE 2.14: Comparison between the sizes of pillars fabricated with local PEB and standard PEB. (a) Pillar size as a function of writing velocity with the laser power from 5 to 8 mW. (b) Two structures fabricated with the laser power of 8 mW and writing velocity of 1 μm/s, one with standard PEB, and the other using the local PEB.

We have proved theoretically and experimentally that it is possible to fabricate submicrostructures on negative photoresists using LOPA DLW without PEB process, thanks to laser induced thermal effect. In particular, this optically induced thermal effect is localized inside the focusing spot, which could be advantageous to optimize the structure size as well as to avoid the accumulation effect inherently existing in OPA-based optical lithography, which is shown in the next section.

2.4.4.2 Accumulation-free and short period structures

Experimental realization of LOPA-DLW in fabrication of multidimensional submicrostructures showed evidently the advantage of LOPA-based DLW [45]. With a few milliwatts of a cw laser and in a moderate exposure time, any kind of sub-micrometer structure with or without designed defect could be fabricated. However, some fabricated structures are not uniform or distorted. The physical causes of the distortion can be attributed to two main effects: dose accumulation effect [64] and shrinkage effects [77]. In this section, those effects will be proved to be overcome by applying local PEB.

Light can be tightly confined within a hundred-nanometer spot by using an OL with high NA. If a single exposure and a PEB process are implemented, a single voxel corresponding to a volume in which the spatial exposure dose is above the polymerization threshold can be created. That has been experimentally confirmed in the LOPA fabrication technique.

As a consequence of linear behaviour of OPA mechanism, the dose accumulation effect is the inherent nature of linear absorption material [78, 79]. In contrast to a conventional TPA method, a photoresist operated in OPA regime does not have any threshold of polymerization [80], hence the voxel size can be controlled by adjusting the exposure dose. In principle, polymerization occurs at the focusing spot with a single-shot exposure resulting in a very small voxel (smaller than the diffraction limit) [81]. However, when two voxels are built side-by-side with a distance of about several hundred nanometers, two resulting voxels are no longer separated [45]. This issue evidently originates from the dose accumulation effect in OPA process.

Similar to OPA microscopy where the microscopy image cannot resolve two small objects which localized at about several hundreds nanometers from each other, the fabricated voxels in DLW also cannot be separated. Abbe's criterion states that, the minimum resolving distance of two objects is defined as $0.61\lambda/\mathrm{NA}$, where λ is the wavelength of incident light. This diffraction barrier thus imposes the minimum distance between different voxels, created by different exposures. Moreover, when multiple exposures are applied, although isolated voxel fabrication is ideally confined to the focal volumetric spot, the superposition of many out-of-focus regions of densely-spaced voxels leads to undesired and unconfined reaction. This results in

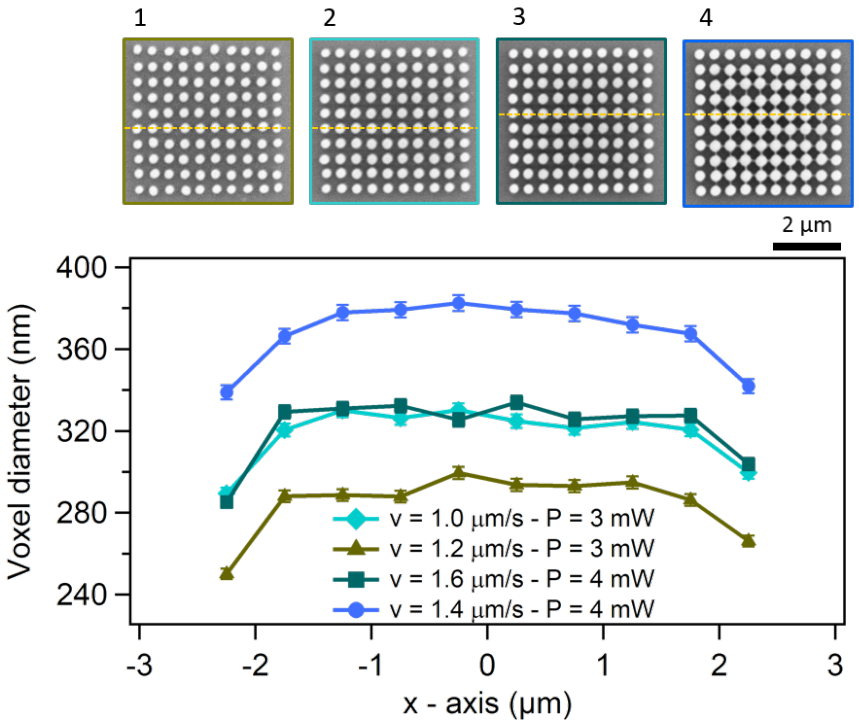

FIGURE 2.15: Structures fabricated with standard PEB. Top: SEM images of fabricated structures. Bottom: sizes of pillars indicated by the dashed line on SEM images plotted as a function of position: the pillars are larger at center of pattern. All structures are fabricated with a period of 500 nm.

the larger effective voxel size, even seperated by a distance far from diffraction limit. Indeed, in the case of OPA, photons could be absorbed anywhere they are, with an efficiency depending on the linear absorption cross-section of the irradiated material. The absorbed energy is gradually accumulated as a function of exposure time.

A dose compensation technique has been proposed and proved to be able to compensate the size difference in the structures [64]. In this technique, outer pillars are compensated by higher dose and it is possible to obtain uniform structures. Nonetheless, this technique requires numerous calculation and tests in order to find out the appropriate dose compensation parameters. For example, for the fabrication of other 2D structures with a sub-micrometer period containing an arbitrary defect, such as a microcavity or a waveguide of arbitrary shape, the dose should be controlled for individual voxel (or pillar) as a function of its position with respect to the defect and to the center or the edge of structure. The dose compensation is different

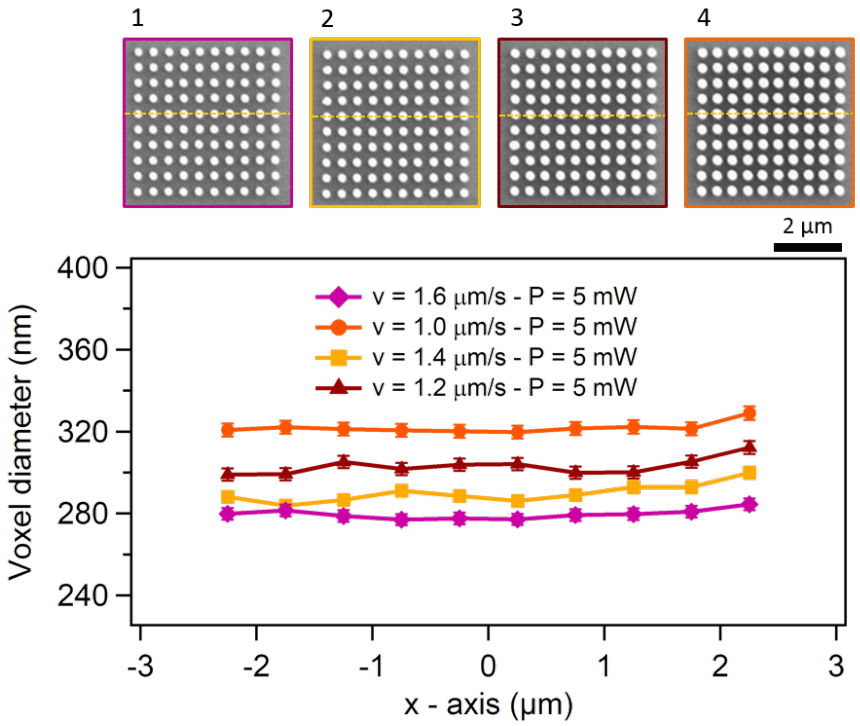

FIGURE 2.16: Structures fabricated with local PEB. Top: SEM images of fabricated structures. Bottom: sizes of pillars indicated by the dashed line on SEM images plotted as a function of position: all the pillars are very uniform. All structures are fabricated with a period of 500 nm.

for different structures, and it requires many attempts to find out the optimized parameters.

Figure 2.15 shows the accumulation effect observed in the structures fabricated using traditional PEB process at different doses. The distance between two pillars is 500 nm, which is considered as a sufficiently short separation to induce noticeable accumulation effect. It can be observed that the pillar size decreases from the center to the edge, with a variation of 10% to 20%, resulting in non-uniform structures. Figure 2.16 shows the SEM images of structures obtained using local PEB. In this case, in order to induce sufficiently high temperature, the laser power (5 mW) was higher than that (3 mW) used with traditional PEB step. In contrast to the structures fabricated using traditional PEB, which shows accumulation effect (Figure 2.15 on the top), the structures obtained with local PEB show nearly perfect uniformity (Figure 2.16 on the top). Moreover, as compared to the dose compensation method,

the LOPA-based DLW using local PEB does not require testing, since the dose applied is constant for all voxels and the range of applicable doses is large. In addition, the PEB step is skipped, which is a great advantage in terms of fabrication time. Furthermore, comparing to structures realized by TPA-based DLW, the period of these fabricated structures is much shorter (only 500 nm or even 400 nm) thanks to the use of short laser wavelength, which can be an additional advantage of this LOPA technique.

Indeed, Figures 2.17(a) and (b) show SEM images of a 2D square photonic crystal fabricated using LOPA DLW with local PEB. The structure was fabricated at a laser power of 6 mW, with the velocity of 2 μm/s, equivalent to nearly 1s of exposure. It can be clearly seen from the SEM images that the structure was well fabricated with the period (distance between two pillars) of 400 nm. All pillars have a uniform shape and size: 350 nm-diameter and 500 nm-height. Figures 2.17(c-f) show two experimental proves of a 3D woodpile and a 3D spiral structure fabricated by this technique. The woodpile structure consists of 18 stacked layers, each layers consists of parallel rods with period a = 400 nm. Due to the shrinkage effect, the line spacing measured at the top surface is reduced. The spiral structure was also well created with a small lattice constant of 600 nm. This is of interest for the fabrication of any photonic crystal with small period, which possess a photonic bandgap in the visible range.

2.4.4.3 Uniform shrinkage structures

Shrinkage is a fundamental issue for photopolymerization in the photopolymer. It is difficult to avoid the non-uniformity when the conventional polymerized microstructures are attached to substrates. The origin of this effect for TPA polymerization has been investigated [82]. It was suggested that the origin of the shrinkage is the collapse of this material during the development stage owing to the polymer not being fully cross-linked under an irradiation power close to the photopolymerization threshold. At illumination parameters slightly above the photopolymerization threshold, the photopolymerization yield is not 100 %. Thus, during the development process, the non-polymerized material is removed, leaving a sponge-like material behind. The

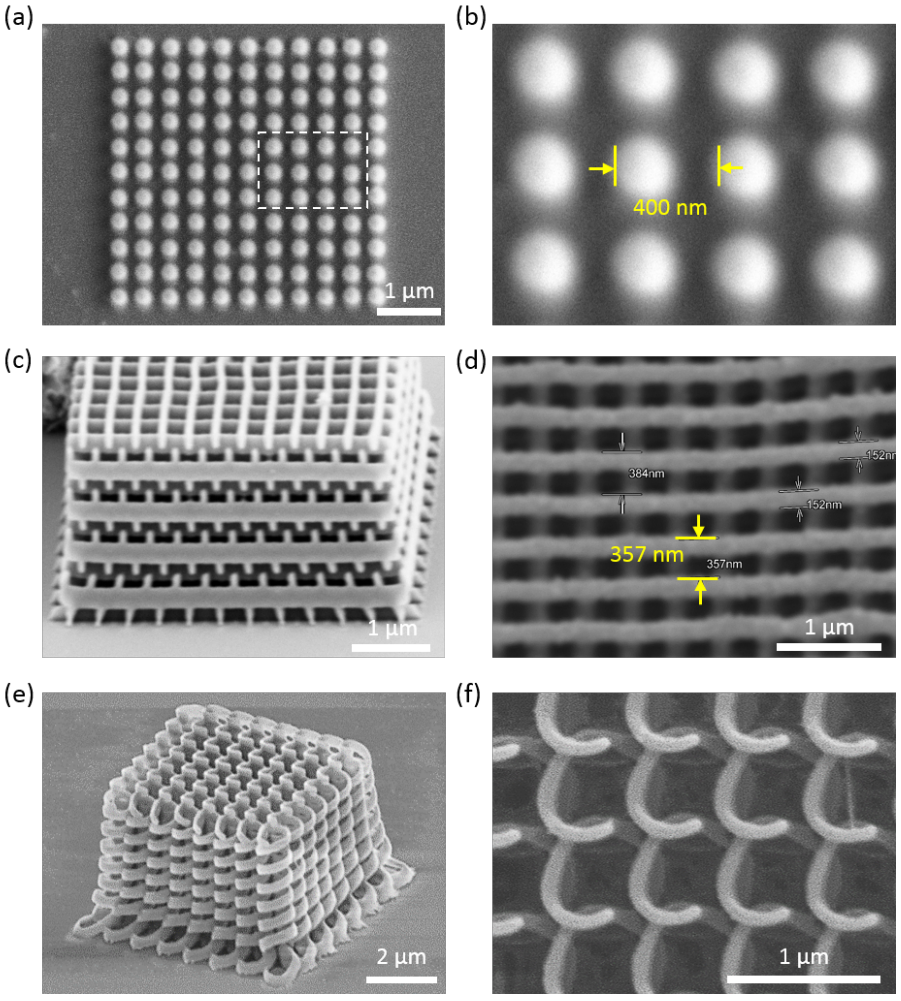

FIGURE 2.17: 2D and 3D structures fabricated by LOPA-based DLW with local PEB. (a-b) SEM images of a structure fabricated at the laser power of 6 mW, writing speed = 2 μm/s, period = 400 nm. (c-d) SEM images of a woodpile structure fabricated with the following parameters: distance between rods = 400 nm; distance between layers = 0.6 μm; number of layers = 18; laser power P = 7 mW and scanning speed v = 2 μm/s. (e-f) SEM images of a spiral structure. Fabrication parameters: diameter of a spiral D = 800 nm; spiral pitch C = 2 μm; lattice constant a = 600 nm; laser power P = 8 mW and scanning speed v = 2 μm/s.

collapse of this material at a molecular level results in the structural shrinkage observed at low average laser powers [82]. However, it has also been confirmed that, although the sponge-like materials are formed during the development because of the incomplete polymerization at low laser power, the shrinkage indeed occurs due to the capillary forces and the dramatic change of surface tension during the drying process [83]. For LOPA 3D fabrication, this shrinkage effect is also observed, with

different levels of distortion for different exposure doses, i. e., the lower the exposure dose is the higher the shrinkage is. Figures 2.18(a-d) show the shrinkage effect observed in 3D woodpile structures fabricated at different doses (P = 9 mW, writing speed v = 4 μm/s, 3 μm/s, 2 μm/s, and 1 μm/s, from left to right, respectively). It can be clearly seen that the degree of shrinkage at different exposure doses is different, i.e., from left to right, the writing speed decreases (the dose increases), the shrinkage decreases. This result is also in agreement with previous report on the shrinkage in the case of TPA polymerization [82], which suggests that in both cases, the shrinkage effect might have a similar origin.

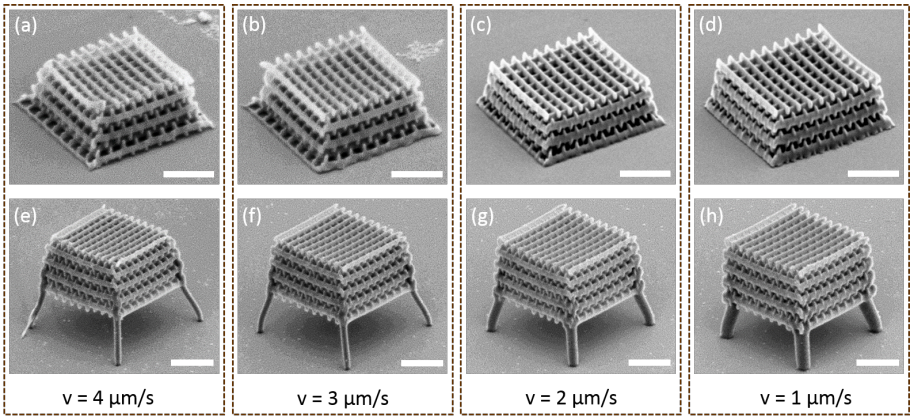

FIGURE 2.18: 3D woodpile structures (number of layers = 16, rod spacing = 1.5 μm and layer spacing = 0.65 μm) fabricated without (a-d) and with "legs" (e-h), at laser power of 9 mW and different writing speeds: v = 4 μm/s, 3 μm/s, 2 μm/s, and 1 μm/s, from left to right. Scale bars: 5 μm.

Non-uniform shrinkage might destroy the structural periodicity of a photonic crystal, resulting in the degradation of its optical quality. While shrinkage is an intrinsic problem, which cannot be avoided, non-uniform shrinkage problem can be positively resolved. Several approaches have been reported on how to overcome this non-uniform shrinkage, including pre-compensation for deformation [84], single [85] and multi-anchor supporting method [82, 86], or freestanding microstructures trapped in cages [87]. All the above methods are investigated for the TPA case. In this work, the multi-anchor supporting method was employed to reduce the deformation caused by the non-uniform shrinkage of 3D microstructures by LOPA DLW. To demonstrate this idea, instead of fabricating woodpile structures directly on glass substrate, four "legs" at four corners of structures were created in order to avoid the attachment of the structures to the glass substrate, which is the direct cause of

the non-uniform shrinkage. These anchors were designed and fabricated as rods of several hundreds nanometers and did not affect the main structure. Figures 2.18(e-h) show woodpile structures with anchors fabricated at different doses. It can be seen that at low dose, the non-uniform shrinkage still remains as shown in Figure 2.18(e). However, when the dose is increased by a small amount, the distortion decreases and disappears. In this case, a laser power of 9 mW and a writing speed of 3 μm/s were sufficient for a considerable uniform structure. Compared to the non-anchored structures, the fabrication speed is reduced by three times to obtain a nearly deformation-free PC, which is remarkable especially for the fabrication of large structures. The shrinkage effect can also be exploited to produce PCs with small lattice constant.

To conclude, the multi-anchor supporting method was successfully applied to reduce the non-uniform deformation of 3D microstructure caused by attachment to the substrate. Since the support with four anchors allows uniform shrinkage of a polymeric microstructure by releasing it from the substrate, the fabricated microstructure shrinks isotropically. The combination of LOPA with local PEB and this supporting method is a promising way of producing small lattice constant photonic structures, which could result in a photonic bandgap in the visible range.

2.5 Potential applications

2.5.1 Hybrid surface-enhanced Raman scattering substrate from gold nanoparticles and photonic crystal

Surface-enhanced Raman scattering (SERS) has been the key for developing ultra-high sensitivity sensors for biochemical molecules since its discovery in 1974 [88]. For practical sensor design, Au or Ag NP decorated surfaces are the first candidates for SERS substrates. The idea is simply to use the SERS effect from NPs, which results from the electric field enhanced by the localized surface plasmon excited by the incident light and its interaction with the individual molecules attached to the surface [89].

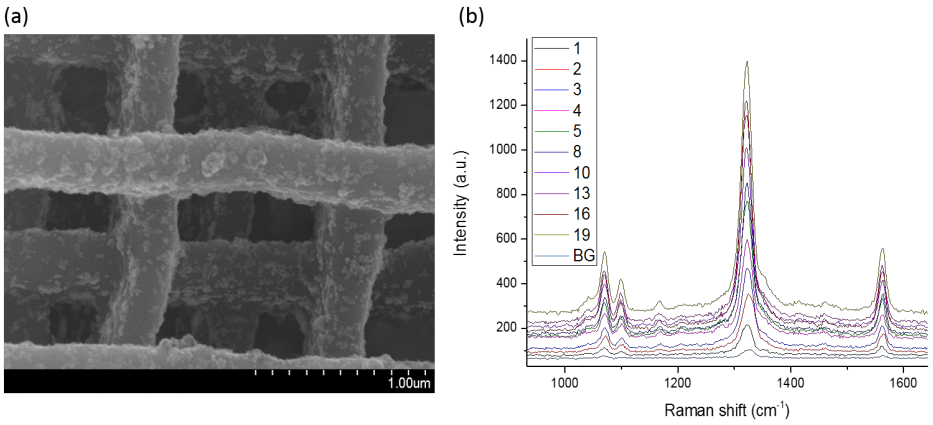

FIGURE 2.19: (a) SEM image of a woodpile structure decorated with Au NPs. (b) Raman spectra from woodpile structures with different numbers of layer decorated with Au NPs.

It is well known that the photonic bandgap (PBG) of a photonic crystal (PhC) provides means of manipulating and controlling the flow of light. Therefore, when the structure of PhC is present in a SERS substrate, similar effects can be expected on the flow of the incident light or that of the SERS signals. For instance, by aligning the PBG of a PhC substrate with peaks in the Raman spectra, one can selectively make some Raman signal to be reflected from the substrate and some to propagate through, leading to selectivity in the detection of the SERS signal.

In the work collaborated with Chung Cheng University (Taiwan), we have fabricated woodpile PhC with different numbers of layer and they have decorated the structures with Au NPs to test with the SERS effect. Figure 2.19(a) shows the SEM image of a woodpile structure decorated with Au NPs. All layers are uniformly covered by Au NPs. Raman spectrum measurement (Figure 2.19(b)) shows higher peak intensities from structures with larger numbers of layer, which indicates the enhancement from the localized surface plasmon excited on the Au NPs with the incident light. Therefore the enhancement observed in the Raman spectra first comes from the Au nanoparticles decorated on the woodpile structures. Due to the 3D nature of the structures, the number of Au nanoparticles illuminated by the incident light per unit area on the structures with more layers is larger than that of the structures with less layers, assuming that they have the same surface number density and the distribution is fairly uniform. This leads to higher Raman signal intensity.

In the future, we aim at fabricating PhC with PBG within which the peaks in the Raman spectra locate. This is not only for the enhancement of the Raman signal intensity but also for the selective detection of the SERS signal.

2.5.2 Optomechanics in polymer for sensor applications

The fields of photonics and phononics, both of which are important for information signaling and storage, have been effectively bridged by the coherent coupling between photons and phonons. In optomechanical devices, transfer of optical momentum into mechanical motion occurs through the pressure exerted by the photons on the oscillating cavity: the photon pressure induces mechanical motion of the device which is detected optically [90, 91]. Materials used to fabricate optomechanical devices are mostly semiconductors, for example InP, GaAs, which are expensive and limited to 2D fabrication. Polymers are reasonable replacement due to the comparable Young's modulus, much lower mass density, and 3D fabrication.

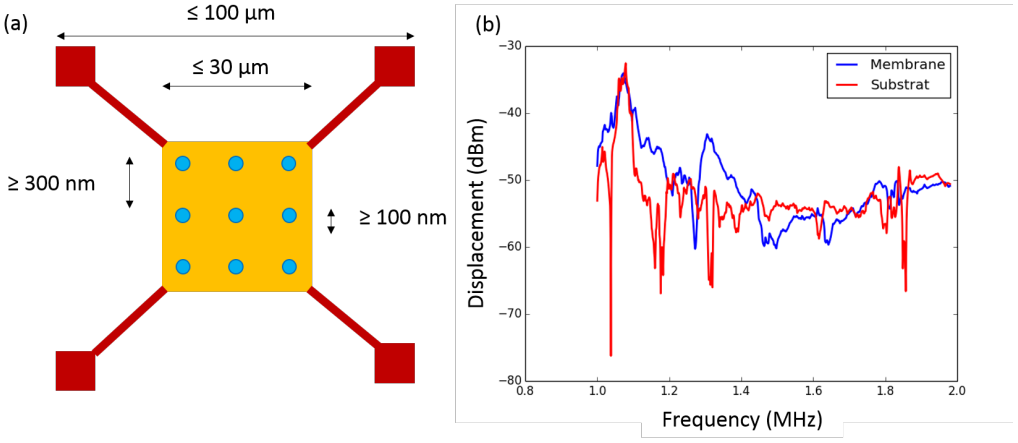

FIGURE 2.20: (a) Design of a 3D membrane for optomechanical oscillation. (b) Optomechanical response of the substrate and the membrane when excited by a laser beam.

In the work collaborated with CentraleSupélec University, we have fabricated 3D polymeric membrane based on their design (Figure 2.20(a)) for optomechanic measurement using Michelson interferometer. A first result showing a mechanical response of the fabricated membrane has been obtained (Figure 2.20(b)).

2.5.3 DFB laser with controllable emitting direction using perovskite material

A distributed feedback laser (DFB) is a type of laser diode, quantum cascade laser or optical fiber laser where the active region of the device is periodically structured as a diffraction grating. The structure builds a one-dimensional interference grating (Bragg scattering) and the grating provides optical feedback for the laser.

DFB laser diodes do not use two discrete mirrors to form the optical cavity (as they are used in conventional laser designs). The grating acts as the wavelength selective element for at least one of the mirrors and provides the feedback, reflecting light back into the cavity to form the resonator. The grating is constructed so as to reflect only a narrow band of wavelengths, and thus produce a single longitudinal lasing mode.

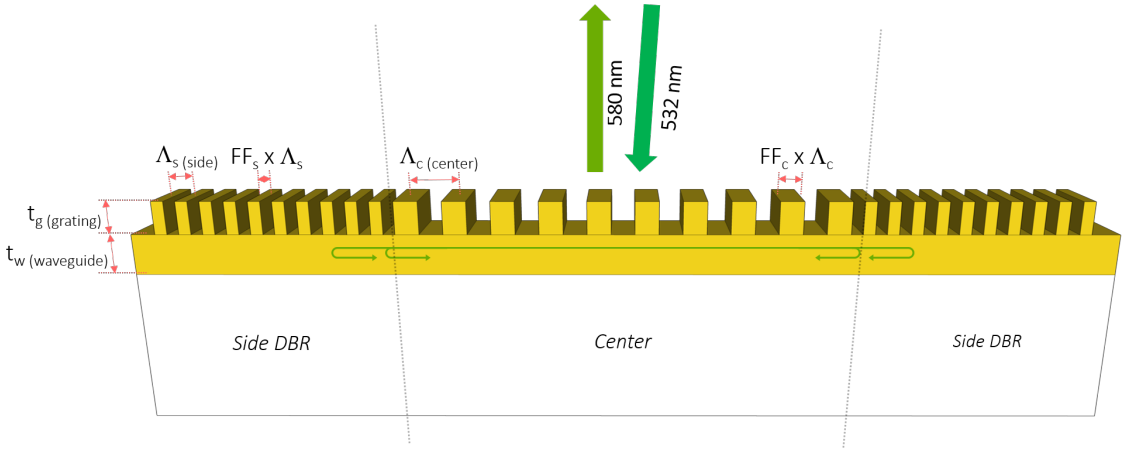

FIGURE 2.21: Design of a DFB laser with controllable emitting direction.

We propose a concept of DFB laser by combining gratings of different periods to enhance the lasing effect (see Figure 2.21). In this design, there are two main parts: the central grating acts as an input/output coupler, allowing the excitation of a guided mode of the stack through one diffraction order, while the Bragg gratings prevent the mode to spread outside the structure. The parameters of the structures are chosen so that the coupler grating presents a resonance peak at a wavelength located in the bandgap of the Bragg grating. A pump laser is incident from the top of the central grating and the emitted beam is collected in the opposite direction.

By changing the incident angle of the pump laser beam, we can control the emitting direction of the emitted beam.

In the work collaborated with Vietnam National University, we have fabricated gratings of different periods on which perovskite materials were deposited for the investigation of lasing effect with controllable emitting direction.

Those results show that LOPA-based DLW is a simple but robust technique which is applicable for many potential applications. However, for the rest of this thesis, we focus mainly on the coupling of NPs into PSs using LOPA-based DLW.

2.6 Conclusion

By using LOPA DLW with optically induced thermal effect taken into account, we have succeeded in fabricating accumulation-free submicrometer polymeric 2D and 3D structures. Solving the heat equation using finite element model realized by Matlab, we demonstrated that the heat induced by high excitation intensity of a 532 nm continuous wave laser confined the crosslinking reaction in the local region where the temperature is higher than the PEB temperature. This resulted in fine and uniform structures, since only the material within the effective temperature region was properly polymerized. Temperature-depth dependence calculation showed that this technique allows the fabrication of uniform 3D sub-micro structures with large thickness. This was then evident by an experimental demonstration of fabrication of a uniform 3D woodpile structure without PEB step, with a period as small as 400 nm. Non-uniform shrinkage effect was also remarkably reduced by applying the multi-anchor supporting method. Compared to the commonly used TPA method, LOPA-based DLW with local PEB shows numerous advantages such as simple, low-cost setup and simplified fabrication process. This technique is an excellent alternative to the TPA method because of the capability of fabricating any desired 1D, 2D and 3D structures with the similarly high quality, but at a lower cost.

Chapter 3

Realization of magneto-photonic microstructures and microdevices

3.1 Introduction

Functional nanocomposites, especially magneto-polymeric nanocomposites have attracted a great attention due to their multifunctionality for a variety of applications, including data storage [92], sensors [93], actuators [94], biomedicine [95], etc.

Microdevices and micromachines with moving parts have now been utilized for environmental applications [96], microfluidics [97], in vivo sensing, monitoring [98], and even inside human body [99]. Unlike photonic crystals which are merely three-dimensional (3D) periodic structures [100], micromachines and devices generally consist of complex 3D components, and therefore are more difficult to fabricate. Moreover, micromachines need mechanical movement of individual parts for an operation, which requires not only well defined, robust microcomponents, but an appropriate machine driving mechanism is also highly desired. Several actuation methods have been proposed, such as an electric field actuation [101], piezo-electric actuation [102], thermal actuation [103], and light-driven actuation [104]. These methods have some challenges, especially for in vivo applications, for example, light-driven [104] is an effective method for manipulating micromachines, but it suffers from high laser intensity, which is not suitable to operate inside human body. The magnetic force

driven technique would be an ideal method for remote control due to its simple, safe and noncontact properties [105].

Magneto-polymeric nanocomposites could be a promising candidate for the fabrication and manipulation of microstructures and microdevices. A number of synthesis and fabrication methods have been proposed to obtain desired magnetic microdevices, for instance, template-assisted method [106,107], self-scrolling technique [108], lancing angle deposition method [109], and direct laser writing (DLW) [110–112]. Among those, DLW has been the most widely used technique thanks to its flexibility and capacity of fabricating arbitrary complex 3D structures. It is worth mentioning that while the TPA-based DLW technique is very powerful for fabrication of desired structures, it requires the use of a pulsed femtosecond or picosecond laser and a complicated optical system [110–112], making it a rather expensive fabrication technique.

In this chapter, we demonstrate the use of LOPA-based DLW as a simple and robust technique for the fabrication of desired multidimensional micro magneto-photonic devices. Superparamagnetic magnetite nanoparticles (Fe_3O_4) were first synthetized and used as nanofillers in a polymer matrix host of SU8 photoresist. We investigated in details the influence of magnetite nanoparticles concentration, of photoresist viscosity, as well as of the preparation duration on the uniformity and the homogeneity of the nanocomposite. We then demonstrated the use of LOPA-based DLW as a simple and robust technique for the fabrication of desired multidimensional micro magneto-photonic structures and devices. Structures with submicro-features were systematically investigated to obtain optimized fabrication parameters and basic concept for their integrations to numerous optical and biological devices. We also demonstrated the fabrication and manipulation of free-floating structures by an external magnetic field showing a strong and controllable magnetic response of the fabricated structures to the external magnetic field, which paves the way for different applications in biotechnologies and optophysics, such as biosensors, actuators and data storage [92–95, 113, 114]. Different models of magnetic microdevices and micromachines are proposed and realized.

3.2 Synthesis of photopatternable magneto-polymer nanocomposite

Nanocomposite made from a photosensitive polymer and magnetic particles (MNPs) has been used for fabrication of magnetic structures with feature sizes larger than 10 μm by using a conventional photolithography [94, 115]. However, when further device miniaturization is desired, the control of nanoparticles dispersion at nanoscale in polymer matrices is critical and challenging. To avoid clustering of particles, the polymer-particle and particle-particle interactions have to be balanced. This issue becomes more difficult with MNPs possessing remnant magnetization. They intrinsically attract each other due to attractive magnetic forces. Therefore, the use of surfactant agent is a typical way to modify MNPs surface for well-mixed nanocomposite materials. However, it usually comes along with challenges related to chemical affinity or toxicity with surrounding environment such as carrier liquids or biological systems. To minimize this occurrence, the superparamagnetic nanoparticles, such as Fe_3O_4, are frequently exploited. Superparamagnetism is a well-known phenomenon exhibited by ferromagnetic single-domain particles with very small size in which no hysteresis and magnetic remanence exist [116]. In this chapter, we present our investigation on the synthesis of photopatternable magneto-polymer nanocomposites by mixing of Fe_3O_4 MNPs and a commercial SU8 photoresist.

3.2.1 Preparation of superparamagnetic nanoparticles

Iron oxide MNPs are widely used in different physical and biological applications owing to their excellent optical and magnetic characteristics. For example, their large surfaces permit strong bonds with the surface of functional molecules or their superparamagnetic nature allows them to be controlled by an external magnetic field. Moreover, their small size (typically 11 nm) are ideal for them to be mixed with polymer materials resulting in homogeneous nanocomposites, which became a subject of intensive research over a decade [117]. The two main forms of iron-based MNPs are magnetite (Fe_3O_4) and its oxidized form maghemite (γ-Fe_2O_3).

In our experiments, we have used Fe_3O_4 NPs, which were synthesized by our colleagues in Hanoi National University of Education (Vietnam). The synthetic procedure can be briefly described as follow [118]: A magnetic fluid is prepared by using the conventional precipitation of Fe^{3+} and Fe^{2+} ions by OH^- at room temperature. In a typical case, 4.17 g of $FeCl_3.6H_2O$ and 1.52 g of $FeCl_2.4H_2O$ are dissolved in 80 ml of distilled water with stirring. Then a solution of 6 ml of 35% NH_4OH was added at a rate of 1 drop per second during a constant stirring. Black precipitates of Fe_3O_4 were formed and isolated from the solution by magnetic decantation method. The water washing and decantation process are repeated several times to purify MNPs. In order to incorporate MNPs with SU8 photoresist, the magnetic decantation process is repeated to exchange solution from water to ethanol. Figure 3.1(a) shows a typical transmission electron microscopy image of Fe_3O_4 MNPs. The average size of MNPs is about 11 nm (Figure 3.1(c)), but they tend to aggregate with an average size of 150 nm or larger, due to their interpartical dipolar interactions. The absorption spectrum of Fe_3O_4 in ethanol solution, recorded by UV-Vis spectrophotometer, reveals a steady decrease from 300 nm to 600 nm as shown in Figure 3.1(b). The absorption at 532 nm-wavelength is quite large, which may have an influence on the fabrication of structures by LOPA-based DLW technique, as it will be discussed in the next chapter. It is also noted in Figure 3.1(d) that there is no hysteresis ($H_C \approx 0$) in the M(H) loop taken at 300 K, indicating the room-temperature superparamagnetic characteristic of the Fe_3O_4 NPs. The MNPs are then ready to mix with SU8 negative photoresist for the fabrication of desired magneto-photonic structures.

3.2.2 Magnetic-polymer nanocomposites

3.2.2.1 Influence of SU8 viscosity and MNPs concentration

The polymer matrix with high viscosity can prevent the inter-diffusion of inorganic substituents such as metallic or magnetic nanofillers. In our work, different types of SU8 negative photoresist and various concentrations of MNPs were used to study the viscosity and concentration effects on the dispersion and the homogeneity of the nanocomposite.

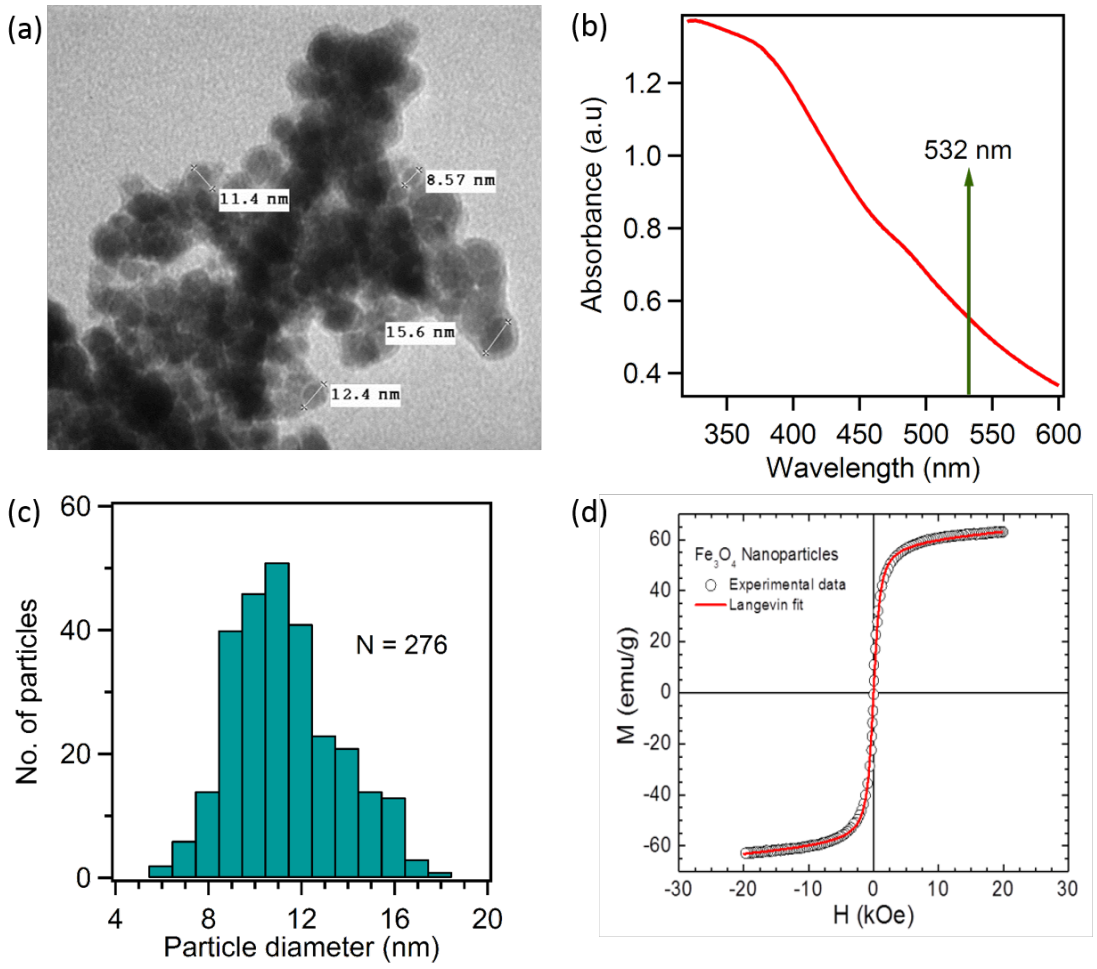

FIGURE 3.1: (a) TEM image of magnetite nanoparticles (Fe_3O_4). (b) Absorption spectrum of Fe_3O_4 nanoparticles in ethanol solution, measured by an UV-vis spectrometer. (c) Statistical results of Fe_3O_4 size distribution. (d) Magnetic hysteresis loop M(H) of Fe_3O_4 NPs taken at 300 K.

For the mixing, MNPs in ethanol were treated with ultra-sonication in a conventional ultrasonic-bath for 30 minutes before being introduced into polymer matrix. Different types of epoxy-based negative photoresist, SU8 2000.5, SU8 2002, SU8 2005, and SU8 2007 (MicroChem Corp.) with different viscosities of 2.49 cSt, 7.5 cSt, 45 cSt and 140 cSt, respectively, were used as candidates for hosting MNPs. Different MNPs/SU8 concentrations ranging from 0 to 10 wt%. were also prepared and analyzed. The mixtures were stirred for 2 hours (typical duration) and followed by 30 minutes of ultra-sonication. Finally, nanocomposite solutions of different viscosities and concentrations were stored in a non-magnetic environment and observed by optical microscopy as a function of time. Figure 3.2 shows photos of four bottles of

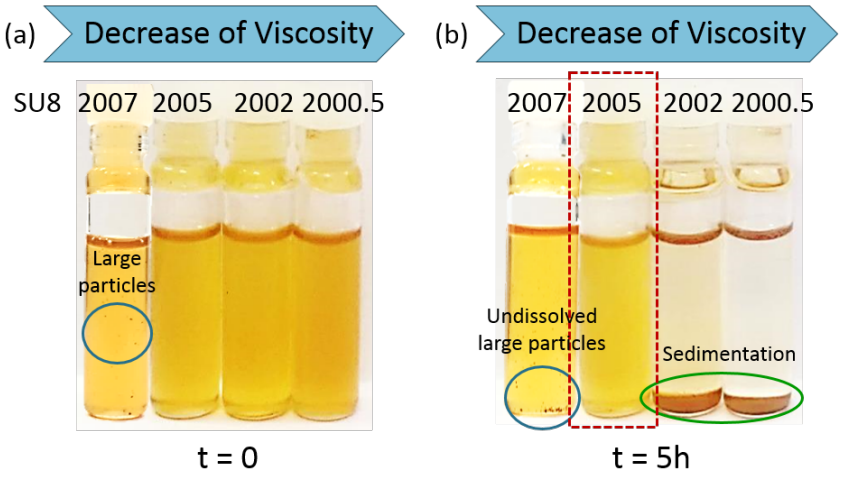

FIGURE 3.2: The dispersion of Fe_3O_4 MNPs in SU8 photoresist with different viscosities, namely SU8 2007, SU8 2005, SU8 2002 and SU8 2000.5. The MNPs/SU8 concentration is 2 wt%. Photos were taken (a) right after mixing and (b) after 5 hours.

nanocomposites prepared with different types of SU8 photoresist and with a MNPs concentration of 2 wt%. The results showed that it is difficult to mix MNPs with SU8 2007 due to its high viscosity (140 cSt). Large remaining clusters can be observed by naked eyes even though they were treated by vigorous stirring for a longer duration. The sedimentation occurred to MNPs in photoresists with low viscosity (SU8 2002 and SU8 2000.5) after few hours of stirring. In contrast, MNPs (2 wt%. - concentration) were completely mixed leaving particles in suspension of SU8 2005. The dispersion is very homogeneous and stable for longtime. However, it is not true for all cases, the sedimentation might occur with higher MNPs concentrations. Indeed, by using SU8 2005 with MNPs concentrations from 2 wt%. to 10 wt%., the observations show that MNPs with a concentration above 5 wt%. quickly deposited on the bottom of containers, and the nanocomposites of lower concentrations, for example, 3 wt%., 4 wt%. and 5 wt%., are partly sedimented as shown in Figure 3.3. Of course, using lower particles contents (< 2 wt%.), the quality of nanocomposites become similar to that of pure SU8 photoresist, but the MNPs quantity is too low to have a strong magnetic response. Hence, we come to a conclusion that the best nanocomposite for realization of magneto-photonic structures and devices is the mixing of SU8 2005 with an appropriate value of viscosity (45 cSt) and MNPs with a modest concentration of 2 wt%.

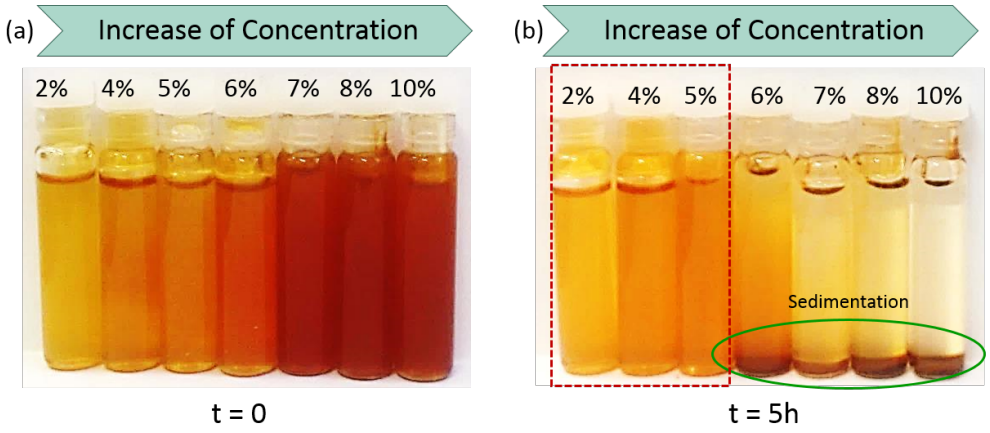

FIGURE 3.3: The dispersion of Fe_3O_4 MNPs in SU8 2005 photoresist at different MNP concentrations, namely 2, 4, 5, 6, 7, 8, and 10 wt%. Photos were taken right after mixing (a) and 5 hours after mixing (b).

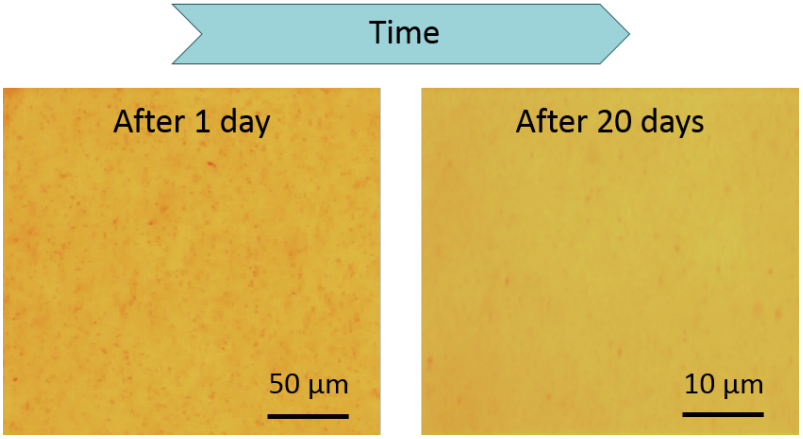

FIGURE 3.4: The dispersion of MNPs at microscale, observed by optical microscopy. The MNPs/SU8 2005 concentration is 2 wt%. Photos were taken after 1 day of mixing (a) and 20 days of mixing (b), without external magnetic field.

3.2.2.2 Influence of time on MNPs dispersion and homogeneity

A remarkable improvement in nanoparticles dispersion was noticed by prolonging the observation time. For that, a small quantity of nanocomposite (2 wt%. - concentration) was dropped onto a glass substrate and examined by an optical microscope. We found that the big clusters of MNPs observed in the "one-day" sample (Figure 3.4(a)) disappeared in the "after 20 days" sample as shown in Figure 3.4(b). It proves that the mixing or waiting time has great impacts on the inter-diffusion of MNPs in suspension, which results in better distribution of particles without using

any surfactant agent. This result opens a possibility for realization of magneto-optical structures at nanoscale. It was further confirmed by fabricating microstructures with nanocomposites prepared at different times. The experimental results show a substantial improvement of structures quality. The microstructures fabricated right after mixing nanocompostite exhibited a rough surface, while those fabricated by the nanocomposite, which was prepared 20 days before, displayed very smooth surface. Moreover, since the nanoparticles were well separated and dispersed in SU8 photoresist, we have further filtered the nanocomposite to obtain a perfect uniform and homogeneous solution, which is crucial for nano-patterning. In fact, just after mixing MNPs with SU8 2005, we have used a filter (450 nm - diameter) to filter the mixtures, but it was very difficult or impossible due to the large size of agglomerations. Twenty days later, we have successfully filtered the mixture to eliminate big particles, if they still exist, leaving the smallest ones in suspension, which are then used for fabrication of nanostructures. In next sections, we will present only the results obtained by nanocomposites, prepared 20 days prior to the fabrication moment.

3.2.3 Typical hybrid properties of nanocomposites

The incorporation of MNPs into polymer matrices of SU8 photoresist allows to exploit both properties of nanofillers and polymer materials, as well as new behaviors due to their mutual interactions. We discuss here only some typical hybrid properties of this nanocomposite, which are the most important for fabrication of functional structures.

3.2.3.1 Absorption spectrum

Due to the excellent transparency and favorable optical parameters, the epoxy negative tone SU8 has been preferred as a special material for fabrication of many optical devices such as waveguide, grating, filter and photonic bandgap structures, etc. On the contrary, the absorption coefficient of Fe_3O_4 MNPs is relatively high at visible range as shown in Figure 3.1(b), explaining the origin of the dark color of MNPs

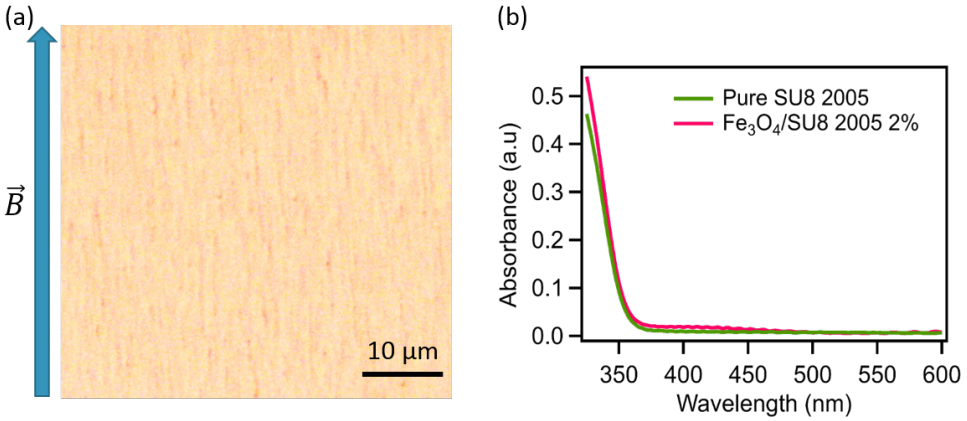

FIGURE 3.5: (a) The chain-like agglomeration of MNPs in nanocomposite with a concentration of 5 wt% under an external magnetic field of 20 mT. (b) Absorption spectrum of the magnetic nanocomposite and pure SU8 2005.

in ethanol solution. When mixing MNPs and SU8 photoresist, the resulting absorption spectrum will be a combination of absorption coefficient of each constituent in the mixture, which may have a strong absorption at the wavelength of LOPA-based DLW technique. However, by testing with different concentrations of MNPs, we found that only nanocomposites possessing high MNPs concentration, usually above 5 wt%., exhibit an observable absorption spectrum in visible range. At very low concentration, 2 wt%. or below, the contribution of MNPs is negligible and the absorption spectrum of Fe_3O_4/SU8 2005 nanocomposite remains almost unchanged, as compared to that of pure SU8 2005 photoresist (see Figure 3.5). It means that the LOPA-based DLW employing a laser at 532 nm–wavelength should allow fabrication of multi-dimensional microstructures with this Fe_3O_4/SU8 2005 nanocomposite.

3.2.3.2 Optically induced thermal effect

The absorption of MNPs, even with very weak contribution, has some effects on the fabrication of magneto-photonic structures. Indeed, when using the nanocomposite, it was observed that the presence of MNPs influences on the exposure power and time of LOPA DLW. The exposure time or power decreased by more than a half when using LOPA-based DLW technique for fabrication of submicrostructures. This is explained by the optically induced thermal effect due to the strong absorption of MNPs at the excitation wavelength (532 nm). This thermal effect allowed

a rapid completion of the polymerization process, thus reducing the exposure time and power.

It is important to note that due to the strong energy absorption of metallic properties as well as their special nature, MNPs show remarkable heating effect that has already been applied for a wide range of biomedical applications, such as hyperthermia [120] and radiotherapy [121].

3.2.3.3 Submicroscale manipulation by an external magnetic field

The ability to response to an external magnetic field of MNPs brings out many unique applications for manipulating objects at microscale, for example, drug delivery [122], cancer treatment [121], and nanomaterial-based catalyst [123]. To demonstrate the presence of MNPs in nanocomposite and their magnetic response to the external magnetic field, a droplet of nanocomposite sample was submitted to an uniform magnetic field of 20 mT and simultaneously observed by an optical microscope. MNPs quickly formed chain-like agglomerations, as illustrated in Figure 3.5(a). It is worth noting that the MNPs moved easily in this case because the nanocomposite still contained a large quantity of solvent. When the nanocomposite thin film was made and the solvent was evaporated, it was more difficult to magnetize those MNPs, thus requiring a stronger magnetic field. In particular, when the structures are fabricated, *i.e.*, the photopolymerization and cross-linking are completed, the magnetization of MNPs in polymer matrices is fixed as permanent, suggesting a lot of ideas for patterning magneto-photonic structures. The fabrication of submicrometer magneto-photonic structures and their interaction with an external magnetic field will be demonstrated in Section 3.4.

3.3 Realization of 2D and 3D magneto-photonic structures on demand

In this section, we show that the LOPA-based DLW allowed us to fabricate 2D and 3D magneto-photonic structures as desired.

In the LOPA operation regime, the excitation power and exposure time are important parameters, which directly determine the characterization of fabricated structures. To study the behavior of the photopatternable magnetic nanocomposite, we first investigated the evolution of structure size as a function of laser power and writing speed. Series of submicropillars were fabricated on a film thickness of 2 μm and analyzed. We note that, in the DLW, a single exposure results in a single polymerized voxel, and a pillar is obtained by scanning the focusing spot along the film thickness. Figure 3.6(a) shows an SEM image of a 2D periodic structure constituted of different pillars, which were created when using different writing speeds, ranging from 1 μm/s to 8 μm/s, and a laser power of 9 mW. The pillar diameter changes as a function of the scanning speed, and very small pillars could be obtained with this magnetic nanocomposite, as shown in the left image of Figure 3.6(a). With a laser power of 9 mW, the pillar size varies between 400 nm and 650 nm, as shown in Figure 3.6(b). By decreasing the laser power to 7 mW or 5 mW, the pillar sizes decrease further to a range of 150 nm–300 nm. Due to the ultralow absorption effect, it was not possible to obtain polymerized structures with further decrease of the laser power and with a reasonable writing speed. This result shows that the fabricated structures on magnetic nanocomposite are quite similar to those obtained by pure SU8 photoresist. By performing many different tests, we have found that the laser power of 7 mW and the scanning velocity of 4 μm/s allow for obtaining small and stable submicropillars. Furthermore, the smallest feature size of 150 nm is even smaller than the minimum focusing spot (a diffraction limit) of the used objective lens. Obviously, the Fe_3O_4/SU8 2005 nanocomposite with a low particle concentration of 2 wt% is an excellent hybrid material to create magnetic nanostructures by the LOPA-based DLW technique.

Based on the above investigations of structure size and periodicity, we now demonstrate the use of a LOPA-based DLW technique to pattern arbitrary magnetic structures by using the magneto-polymer. Figure 3.7(a) shows a SEM image of an arbitrary shape 2D structure, the letter "LPQM". In this experiment, the "LPQM" structure was patterned by a scanning speed of 4 μm/s and with a laser power of 5 mW, which is lower compared to the laser power used for fabrication of other structures such as square and hexagonal structures. It is due to the accumulation of exposure energy at the vicinity of each point when the distance between them was set below 250 nm. An SEM image of a 2D pillar array magneto-photonic pillar array,

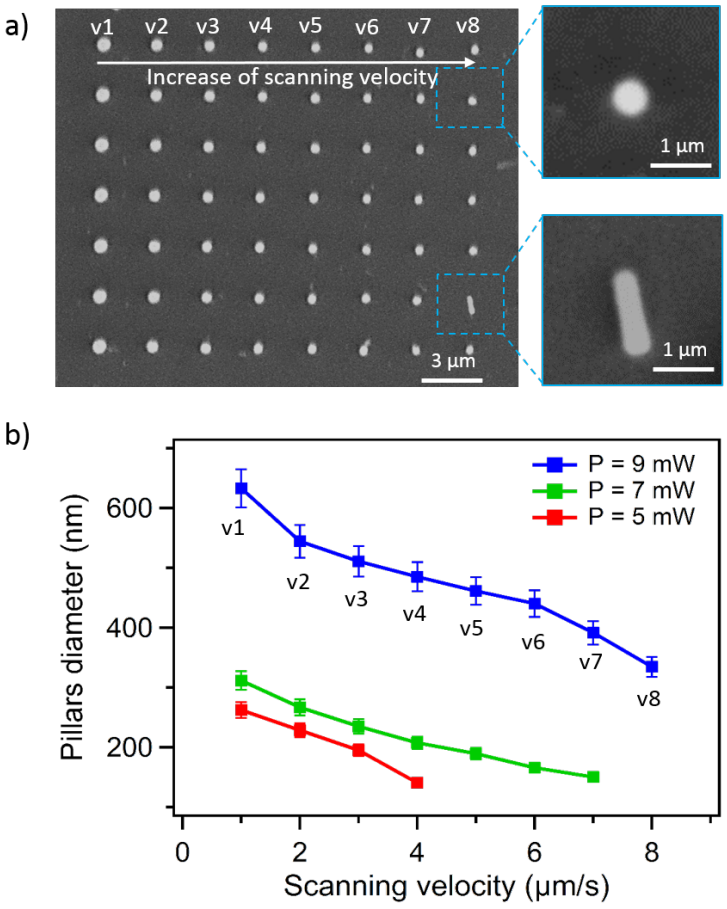

FIGURE 3.6: Dependence of the size of magneto-photonic pillars on exposure doses (laser power and scanning velocity). (a) the SEM image of a pillar array with different diameters realized by different scanning velocities (the laser power = 9 mW). SEM images on the right show side and top views of a single pillar. (b) Plot of pillar diameters as a function of scanning speed for three different exposure powers.

with a period of 1.5 μm is shown in Figure 3.7(b). This structure was fabricated at a laser power of 10 mW and a writing speed of 3 μm/s.

Various 3D structures have also been realized. Figure 3.7(c) shows a SEM image of a 3D woodpile structure, which is made of 10 alternative layers separated from each other by 750 nm. The distance between two lines in x- and y-directions is 2 μm. It is interesting to note that this woodpile structure exhibits no shrinkage effect, which might be due to the presence of MNPs. It opens a possibility in fabrication of 3D structures with an important height for further applications.

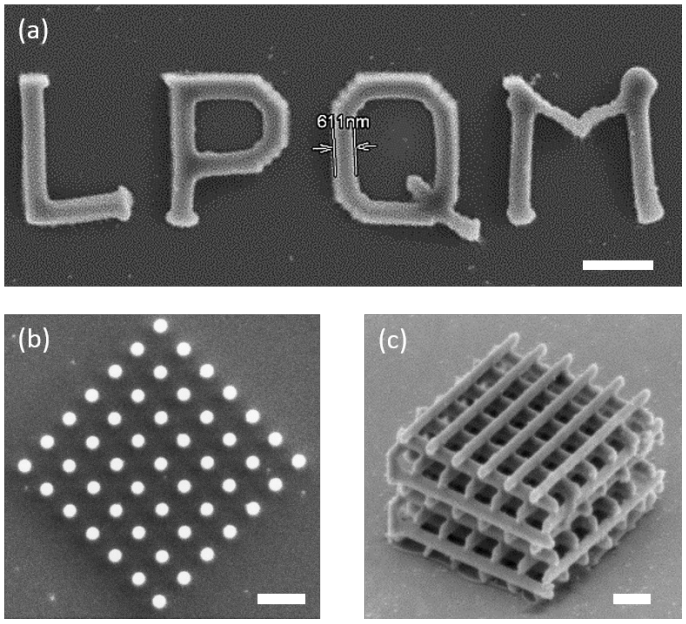

FIGURE 3.7: (a) SEM image of letter LPQM, fabricated at a laser power P = 15 mW, writing speed v = 3 μm/s. (b) SEM image of a 2D pillar array, fabricated at P = 12 mW, v = 2 μm/s. (c) SEM image of a 3D woodpile PC. Fabrication parameters: rod spacing = 2 μm; distance between layers = 1 μm; number of layers = 10; laser power P = 12 mW and scanning speed v = 2 μm/s. Scale bars: 2 μm.

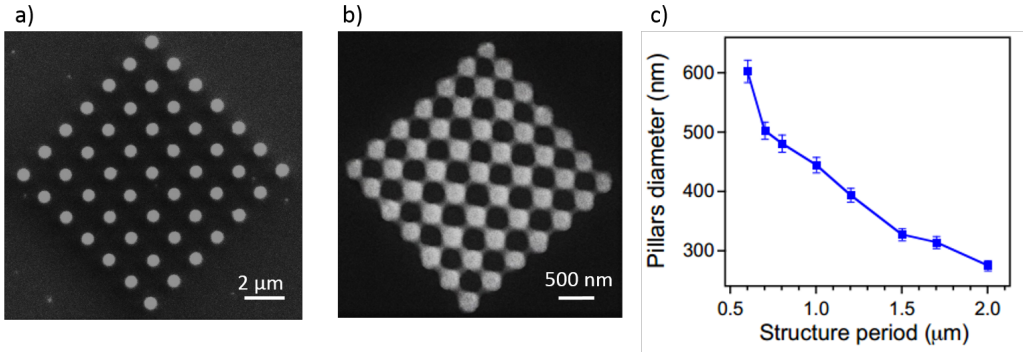

FIGURE 3.8: Influence of the dose accumulation effect on pillars sizes. SEM images of periodic pillars arrays realized with a period of 1.5 μm (a) and with a period of 0.6 μm (b). (c) Pillar diameters as a function of the distance between pillars (the period of the array). The laser power and the writing speed were fixed at 6 mW and 2 μm/s, respectively, for all pillars.

For most applications of PS, the small size is not only a key parameter but also the minimum distance between two features. We have therefore examined the quality of structures as a function of the structure lattice parameter. Different magneto-photonic structures with a periodicity varying from 2 μm to 0.4 μm were fabricated

and depicted, for example, in Figure 3.8(a,b). The size of pillars increased when the distance between pillars decreased as shown in Figure 3.8(c). We found that the good structures were obtained with a periodicity larger than 0.5 μm. Actually, the fabrication relies on an OPA mechanism, and there exists a dose accumulation effect in the case of a small periodicity. The degree of polymerization within the laser spot as well as in the out-of-focus region are completely defined by the number of photons absorbed linearly during exposure, which leads to unwanted structures when pillars are set very close to each other. The mechanism of this accumulation effect was explained in Chapter 2. This result is again similar to that observed with pure SU8 photoresist. In addition, the optically induced thermal effect became more pronounced with the presence of MNPs, which exhibit a thermosensitive property. This thermal effect accelerated the polymerization effect and locally heated up the exposed area, and the PEB process was therefore neglected. Thanks to the local PEB, the minimum distance (0.5 μm) between pillars resulted in a structure of similar quality as that realized with pure SU8 photoresist, by using the same optical setup. The small size and short distance should be good enough for different applications based on magneto-photonic structures.

All these experimental results confirm that any magneto-photonic submicrometer structure or device can be realized by using the LOPA-based DLW on this magnetic/polymeric nanocomposite. We will demonstrate in the next section that those nanostructures contain MNPs, and they can be manipulated by an external magnetic field as desired.

3.4 Fabrication on demand of free-floating submicrostructures by LOPA-based DLW

The performance of devices interacting with environments such as biological system requires a proper selection of materials in term of chemical stability, biocompatibility, etc. For that reason, magnetic nanocomposite with special properties brings out a possibility of manufacturing free-moving magnetic devices. Consequently, magnetic microstructures for remote actuation have attracted a great attention recently. They are potential candidates for interfacing biological environments [124]. With the aid

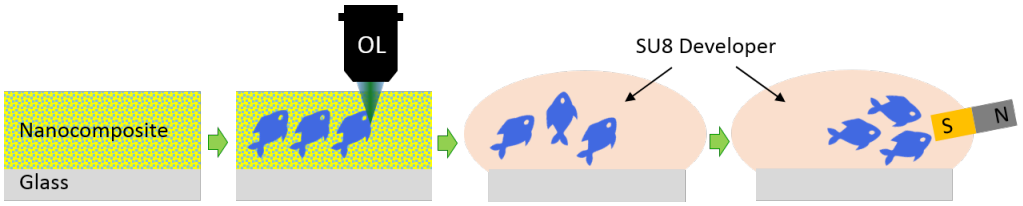

FIGURE 3.9: Illustration of the fabrication and development processes of the micro-swimmers.

of an external magnetic field, the displacement in three dimensions of magnetic structures can be controlled as desired. However, the structure size is still challenging for interaction with smaller targets. In this part, we present the realization of free-floating magneto-photonic microstructures by LOPA-based DLW techniques.

In order to prove the response of magnetic structures to a magnetic field, arrays of "micro-swimmers" were fabricated as an example for demonstration. Figure 3.9 illustrates the fabrication and demonstration of magnetic field-driven processes. First, an array of microswimmers was fabricated. Unlike other fabrication process where good attachment of structures to the substrate is required, the microswimmers were created at a midway position in order to assure the free-floating ability afterward. After that, a developer solvent was dropped directly on the subtrate, washing away all the unexposed areas, leaving the microswimmers which are free to move inside the liquid. We note that these microswimmers were superparamagnetic since they were created from superparamagnetic MNPs. The superparamagnetic microswimmers are more advantageous than conventional ferromagnetic microswimmers, as ferromagnetic microswimmers tend to attract to each other, making them difficult to move freely. By contrast, the superparamagnetic microswimmers can move freely and easily under an applied external magnetic field. A magnetic field generated by a permanent magnet was then applied to investigate the magnetic field response of the magnetic micro-swimmers. Figure 3.10(a) shows an SEM image of the micro-swimmers and the zoomed image of one pattern, fabricated at a power of 9 mW. We note that, for SEM examination, these microswimmers were fabricated attached to the glass substrate. Figure 3.10(b) shows a series of screenshots at 0s, 5s, and 20s of a video captured by an optical microscope to illustrate the whole process from the structural development to the movement toward higher gradient of the external magnetic field. Obviously, all of the micro-swimmers quickly moved toward the

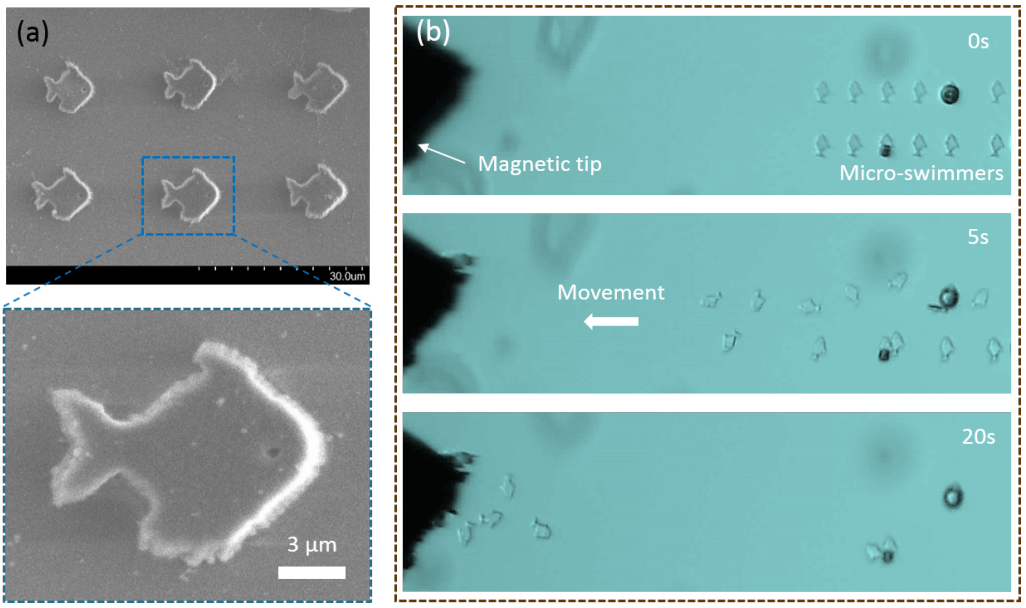

FIGURE 3.10: (a)SEM image and zoomed image of the micro-swimmers fabricated at 9mW. (b) Screenshots showing the movement of micro-swimmers towards the magnetic tip.

magnetic tip, confirming the presence of Fe_3O_4 MNPs inside the structures and their strong response to the applied magnetic field. We also performed a similar process, but without applying the external magnetic field. In this case, the structures just randomly floated in SU8 developer.

Since the magneto-photonic micro-structures response strongly to the external magnetic field, it should be possible to fabricate magneto-photonic micromachines and microdevices with complex components which can be mechanically driven by magnetic force. In the next section, the realization of such microdevices by LOPA-based DLW will be demonstrated.

3.5 Realization of 3D magneto-photonic devices

The great advantage of the DLW method is that it allows the realization of arbitrary structures on demand. The LOPA-based DLW technique has just been demonstrated to be able to pattern magnetic structures from the magneto-polymeric nanocomposite, which show strong response to an external magnetic field. Magnetic micromachines and microdevices have shown their potential for applications in various fields,

such as biomedical fields [110,125], and microfluidics [126], due to the biocompatibility and flexibility of the magnetic actuation. Figure 3.11(a) shows a designed model of a microfan which consists of two parts: the central pillar part with two large ends and two blades. The central pillar prevents the microfan from moving away during the development, and allows the fan to freely rotate around it like a turbine. External magnetic field can be applied to manipulate the rotation of the fan, making it a potential candidate to be incorporated into a microfluidic system as an active part. Figure 3.11(b) shows SEM images of the fabricated microfans, which are about 9 μm long and 5 μm high. Shown in Figure 3.11(c) is a model of a micro-spring, one end of the spring is fixed to a cubic anchor attached to the substrate, and the other end is sticked to a freely moving part. Figure 3.11(d) shows SEM images of the microsprings fabricated using LOPA DLW. These springs were created with the beads attached to the substrate in order to keep their true form for SEM imaging, in practice, these beads should be free to move.

The remote control of these structures can be realized by applying an external magnetic field. As illustrated in the schematic model (Figure 3.11(c)), one end of the spring is fixed to a polymerized cubic anchor attached to the substrate, and the other end is polymerized into a sphere shape as a moving part. The movement process of such microspring with a length of 60 μm has been observed and recorded under a microscope in Ref. [112]. In this work, we target smaller structures, which results in difficulties in observing using a microscope. We propose another method for observation, as illustrated in Figure 3.12(a). After fabrication, the sample is put back to the setup and scanned to identify the position of the microspring. An external magnetic field is then applied, causing the stretch of the microspring, which can be scanned again at this state to observe the difference. Using this method, we expect to estimate the frequency of the oscillation of the spring. The focusing spot of the laser beam is first fixed at the object position when the spring is at the stretched state, at which the photodiode records a high photon count signal. The spring is then released by removing the magnetic field and starts to oscillate at a certain frequency. When the object is out of the focusing spot of the laser beam, the photodiode records a low photon count signal. The movement repeats and we can obtain a time-dependent profile of the oscillation of the microspring, from which we can deduce its frequency. In practice, this frequency can be easily determined from the Young's modulus of the material and the sizes of the spring

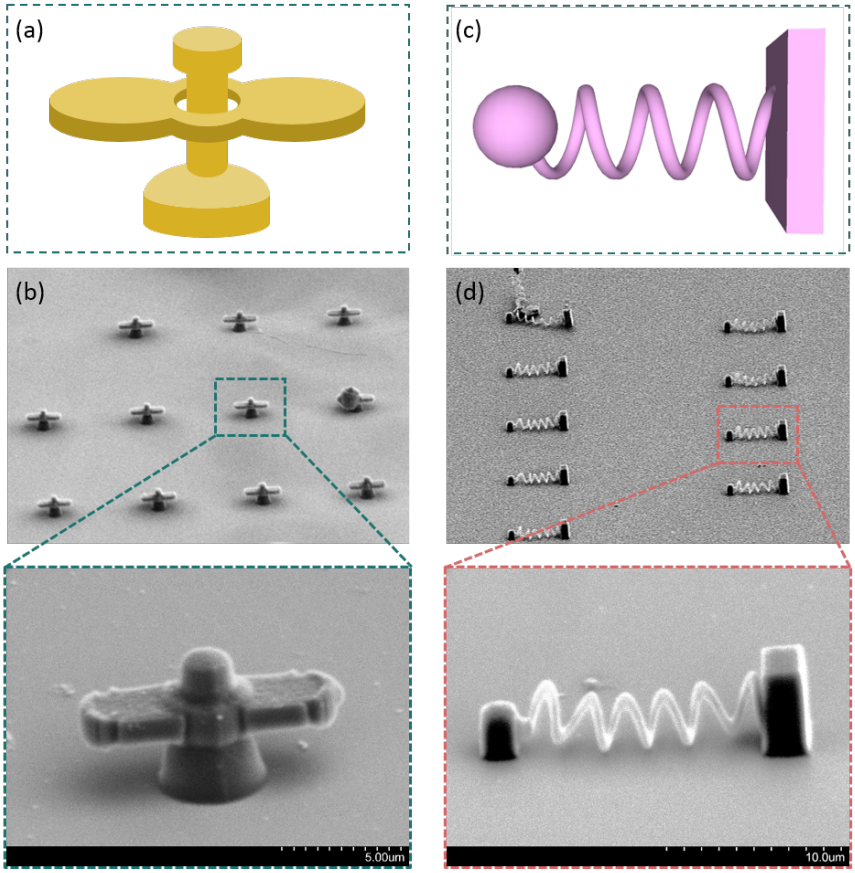

FIGURE 3.11: (a) Design of a microfan. (b) SEM image of an array of microfan and a zoomed image of a microfan (side view). The microfans were fabricated at the power of 8 mW. (c) Design of a microspring. (d) SEM image of an array of micro oscillator and a zoomed image of a micro oscillator (side view). The micro oscillators were fabricated at the power of 8 mW.

and the object. Figure 3.12(b) shows a fluorescence image of a microspring at its rest state. Three parts of the spring including the anchor, the spring, and the object can be easily identified from this image. However, the investigation of the movement of the microspring is still in progress and will not be shown in this thesis.

All of these experimental results confirm that any magneto-photonic microstructures or devices can be realized by using the LOPA-based DLW on this magneto-polymeric nanocomposite. It opens a possibility to go further on development of magnetic nano-devices and micro-robotic tools for a wide range of applications.

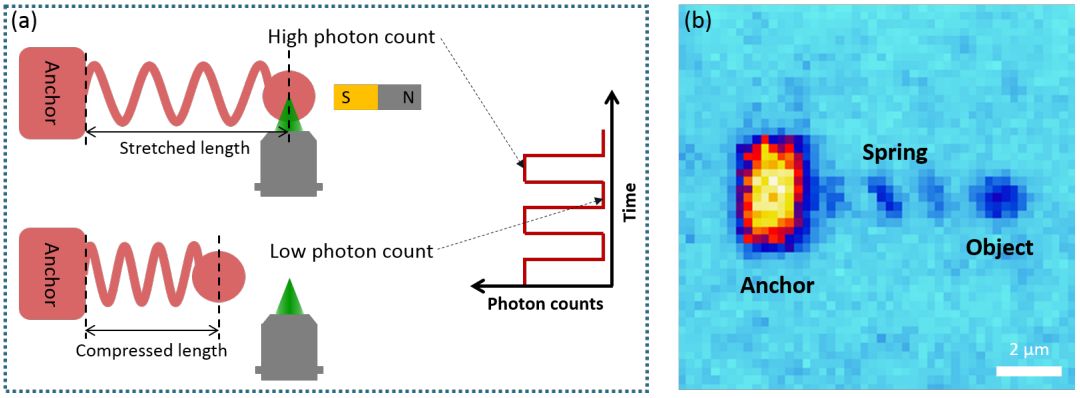

FIGURE 3.12: (a) Illustration of the remote control of a microspring. (b) Fluorescence image of a microspring at its rest state obtained by scanning with the 532 nm laser.

3.6 Discussion

The fabrication of magneto-photonic microstructures by LOPA DLW has been demonstrated. In the future, the fabrication of 2D and 3D magnetic structures with determined orientation of magnetic dipoles as shown in the schematic in Figure 3.13 is highly desirable. This can be achieved by applying tunable external magnetic field during the fabrication process. Particularly, it is interesting to study the coupling of single MNPs with PSs. However, it is quite challenging to optically identify single MNPs since they absorb the excitation light and do not emit fluorescence signal. Attempts have been made to determine single MNPs by measuring the excitation light (532 nm) reflected from samples. Since MNPs show a slight absorption at the wavelength of 532 nm, they will appear on the scanned map as dark spots. However, it has not been confirmed that those dark spots are single NPs. Another solution is to use fluorescent magnetic NPs. We have investigated Ag@Fe_3O_4 core/shell nanoflowers and we have been successful in determining single NPs by detecting the fluorescence signal emitted from the NPs. Nevertheless, we had some difficulties in the fabrication process due to the explosion effect originating from the metal core. Further investigations on other fluorescent magnetic NPs will be implemented.

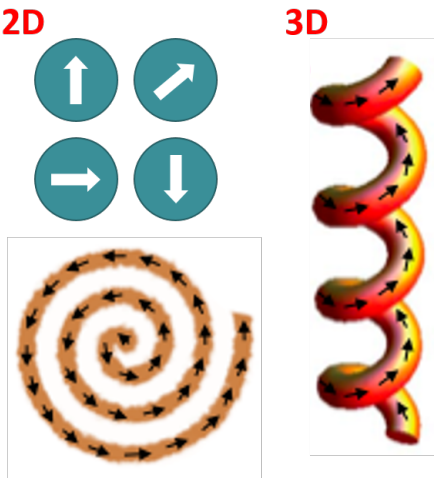

FIGURE 3.13: Schematic of 2D and 3D structures with desired magnetic orientation.

3.7 Conclusion

In this work, we have successfully demonstrated the fabrication of magneto-photonic submicrostructures on demand by use of LOPA-based DLW technique. By incorporating superparamagnetic magnetite nanoparticles (Fe_3O_4) into SU8 polymer matrix with various SU8 viscosities, we have found the most appropriate value of viscosity to host MNPs in order to ensure an uniform distribution of nanoparticles at a concentration of about 2 wt% without sedimentation. The sample preparation time also plays an important role allowing the remarkable improvement in MNPs dispersion resulting in a high quality magnetic nanocomposite. The homogeneous dispersion of MNPs within the polymer matrix enables us to fabricate desired magnetic structures at nanoscale. The LOPA-based DLW technique has been successfully employed to realize any arbitrary 2D and 3D submicrostructures. Furthermore, we also demonstrated a possibility to fabricate magneto-photonic devices by elaborating free-moving magnetic microswimmers and by the examination of their interaction with an external magnetic field. The high magnetic responsive property of hybrid structures enabled us to make unlimited movement. The LOPA-based DLW technique was also successfully employed to realize desired 3D magneto-photonic crystals and microdevices with complex 3D components. Therefore, the combination of LOPA-based DLW technique with nanocomposite and with the aid of an external magnetic field will allow us to obtain any desired magneto-photonic devices. These

results open many promising applications, such as the development of microrobotic tools for transport in biological systems.

Chapter 4

Coupling of a single gold nanoparticle into photonic structures

4.1 Introduction

Noble metal NPs have attracted enormous attention due to the properties related to localized surface plasmon resonances (LSPRs) [127, 128]. When exciting a single metallic NP by a light beam with appropriate wavelength, the electromagnetic field is strongly and locally amplified nearby the NP. This localized plasmonic effect becomes even stronger when those NPs are organized in nanostructures, such as dimers [129, 130] or arrays [127, 128, 131–135]. The LSPR phenomenon has therefore triggered many investigations on the optical responses of integrated metallic/active nanostructures, such as: fluorescence enhancement [131], nonlinear optics enhancement [132], antennas for sensing [136], or organic plasmon-emitting diode [137]. Meanwhile, photonic crystal cavities are of great interest for confining light at resonance frequencies and enhancing electromagnetic field [22, 23, 138]. The resonant mode of a photonic crystal cavity shows a much narrower spectrum than that of the plasmonic resonance mode. Combining plasmonic and photonic cavity modes thus allows a strong modification of optical response of the hybrid system, which

may lead to interesting applications. Similarly to the case of magnetic/PS coupling, the plasmonic/photonic coupling can be realized by an ensemble of metallic NPs [139–141] or by an individual gold NP [26]. All these hybrid structures proved a strong interaction of the cavity mode with the plasmonic NPs. Indeed, Wang *et al.* demonstrated theoretically and experimentally the coupling of the LSPR of Au NPs ensemble with a resonant mode of a 1D cavity [140, 141]. Using a pump wavelength of 550 nm, which matches the LSPR of the Au NPs and the defect mode of the cavity, they obtained a transient optical response enhancement of the NPs up to 30 to 40 times and a strongly sharpened spectral profile. Besides, in order to couple a single metallic NP into a photonic crystal cavity, Barth *et al.* [26] proposed to use a dip-pen technique with AFM manipulation, which pushes a single gold NP towards the photonic crystal cavity, which is previously fabricated by a standard technique on a semiconductor material. The coupling is realized through the evanescent field of the metallic NP and the dielectric photonic crystal cavity mode [26].

In this chapter, we report our investigation on the coupling of a single gold NP with a polymer-based PS. First, using a software called Lumerical based on FDTD method, we build a simulation model which shows theoretically the plasmonics/photonics coupling. Then, employing LOPA-based DLW with a double step process, we demonstrate the precise incorporation of a single NP to a microstructure as desired. For this, we take advantage of the absorption of materials: strong absorption of NP and low absorption of photoresist. The fabrication of the desired structure is therefore carried out in two steps: first, to identify the position of the NP by LOPA DLW at a very low excitation power, and second, to fabricate the resin structure containing the NP at a higher power. The fabricated samples are charaterized using the same optical setup, and we show an enhancement in the fluorescence signal of the samples, which is explained by the simulation model above.

4.2 Localized plasmonic resonance and plasmonics/photonics coupling: theoretical calculations

Plasmonics is the discipline describing the bridging between electromagnetic radiation and electronic oscillations. The excitation, propagation, and localization of the

plasmonic effect can be tailored by controlling particle size and shape. We therefore distinguish three categories of plasmonic effects: i) surface plasmon resonance; ii) localized surface plasmonic resonance; and iii) plasmonic nanostructures. In this section, we focus mostly on the second case dealing with plasmonic effect of single metal NP as well as its coupling to different polymer-based PSs.

4.2.1 Localized surface plasmonic resonance

Plasmons arise from the collective oscillations of free electrons in metallic materials. Under the irradiation of an incident electromagnetic wave, the free electron are driven to coherently oscillate at a frequency relative to the lattice of positive nuclei. For a metallic structure with finite dimensions, such as metallic films, only the electrons on the surface are the most significant since the electromagnetic wave can penetrate a limited depth in metal. Therefore, the collective oscillations of such electrons are called surface plasmon resonance (SPR).

In the case of metallic NPs, the collective oscillations of free electrons are confined to a finite volume defined by the particle dimensions. Such plasmons of NPs are termed as localized surface plasmon resonances (LSPRs) since they are localized rather than propagating. When the free electrons in a metallic NP collectively oscillate at a certain resonant frequency due to the incident electric field, the incident light is absorbed by the NP. Some of these photons will be scattered, *i.e.*, released in all directions with the same frequency, while some others will turn into vibrations of the lattice, which is known as absorption.

The plasmon resonant frequency is highly sensitive to the refractive index of the surrounding environment, a change in refractive index results in a shift in the resonant frequency. We have used a common finite different time domain (FDTD) method to perform simulations of LSPRs of a typical metal NP (gold). First, we considered a spherical Au NP (diameter = 50 nm) immersed in different media, such as air (n = 1), water (n = 1.33), and glass (n = 1.5). Figure 4.1(a) shows the calculated absorption spectra of this Au NP, where we can clearly observe an increase of absorption coefficient and a red shift of the LSPR peaks as a function of the refractive indices.

It has also been known that the number, location, and intensity of LSPR peaks of metallic NPs depend strongly on the shape and size of the NPs. Metallic nanorods are one kind of nonspherical, anisotropic NPs with polarization-dependent response to the incident light. When a nanorod is excited along the short axis, a plasmon band at wavelength similar to that of Au nanospheres, commonly referred to as the transverse band, is induced. If it is excited along the long axis, a much stronger plasmon band in the longer wavelength region, referred to as the longitudinal band, is induced. When Au nanorods are dispersed in a solvent, we can observe a steady-state extinction spectrum containing both bands of longitudinal and transverse plasmons due to the random orientation caused by the Brownian motion of the particles. While the transverse band is insensitive to the size of the nanorods, the longitudinal band is redshifted significantly from the visible to near infrared region with increasing aspect ratio (length/width). Figure 4.1(b) shows the calculated absorption spectra of Au nanorods with different aspect ratios (the diameter was fixed at 15 nm, and R = 1, 2, 2.5, 3). We can see that the transverse plasmon band exhibits a slight blue shift as aspect ratio of the nanorods increases, while the longitudinal peak is continuously shifted from the visible to near infrared spectra as the aspect ratio increases. We note that, in our simulations, the Au NPs are modelled as ellipsoidal particles, while the experimentally fabricated nanorods are more like cylinders. Nevertheless, it has been common to treat small metallic nanorods as ellipsoids in order to adequately calculate their optical properties and their geometry/property relationship.

The plasmonics/photonics coupling has drawn great attention since such combination can induce a modification of optical properties of the cavity as well as the NP introduced inside. Specifically, we are interested in Au NPs and polymeric photonic cavities. In order to clarify the mechanism of such coupling, we have performed various simulations using FDTD method to address different issues: How the excitation light is coupled into a photonic cavity; How the LSPR of the NPs is enhanced due to the coupling of the light in the cavity; And how the emitted light of the NPs is coupled out of the cavity. For all these simulations, we have also considered Au NP as a plasmonic and fluorescent NP, since it can absorb and emit light.

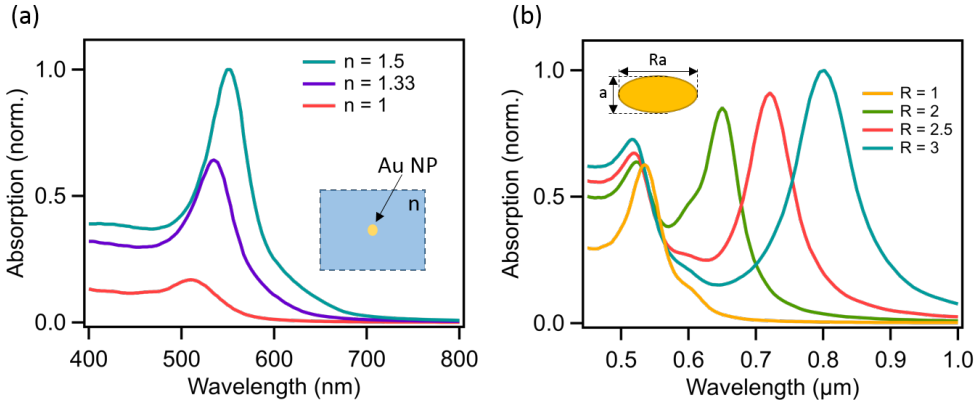

FIGURE 4.1: (a) Numerical simulation of absorption spectra of Au NPs (diameter = 50 nm) in different media (air, water, glass). *Inset*: Illustration of a single Au NP in a medium with refractive index n. (b) Calculated absorption spectra of Au nanorods in water (n = 1.33) with different aspect ratios, R. The diameter of the Au nanorod is fix at a = 15 nm. *Inset*: Design of Au nanorod.

4.2.2 Coupling of light into cavities

First, a simulation addressing the coupling of light into a photonic cavity was carried out. We investigated two types of cavity, without any metallic particle: microsphere and micropillar made of SU8 photoresist (refractive index of SU8 was assumed to be 1.5 for all wavelengths). We built a simple model in which the photonic cavity (a microsphere with the diameter = 1.12 μm and a micropillar with the height = 1.2 μm and the diameter = 0.3 μm) is placed on a glass substrate, as shown in Figures 4.2(a, c). A linear polarized (along x–axis) plane wave source is placed underneath, pointing upward (in z direction). A monitor is set in the (xz)– or (yz)–plane to record the incident light field. We studied the coupling effect of the 532 nm wavelength, which is the wavelength of the excitation laser used in the experimental work. In other words, the coupling of the incident light from the excitation source into the cavities could be properly studied in this calculation.

Figures 4.2(b, d) show the square modulus of the electric field within the microsphere and micropillar when they are illuminated by a plane wave at 532 nm. It can be clearly observed that, for the microsphere, the maxima of the field mostly locate at the two ends of the sphere in the direction of the incident light, whereas in the center, the field intensity is much lower. In contrast, for the micropillar, the field is amplified and localized along the height of the pillar. If a source, which generates a

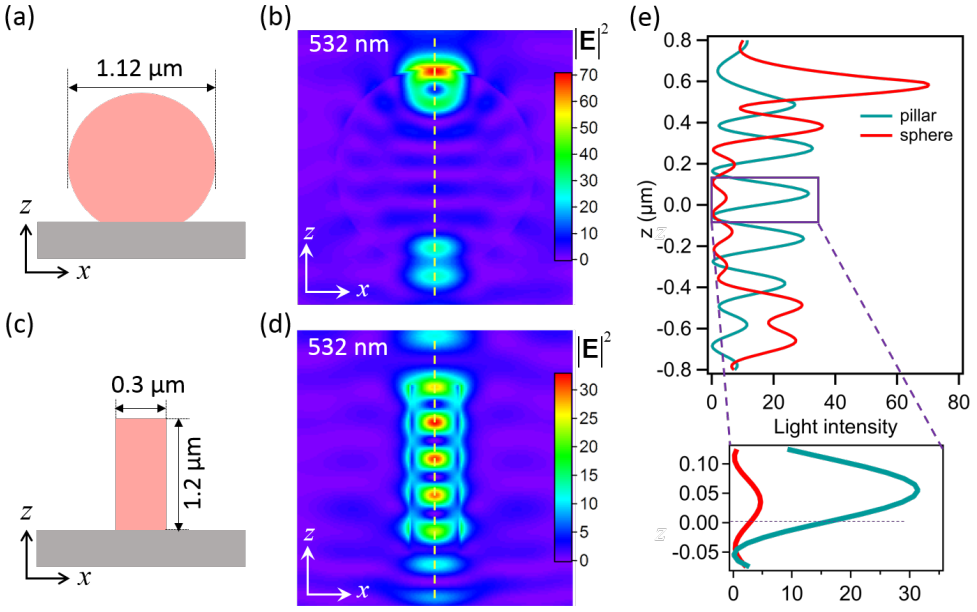

FIGURE 4.2: (a), (c) Design of polymer-based photonic cavities. (b), (d) Simulation result of electric field intensities inside a SU8 microsphere (diameter = 1.12 μm) and in a SU8 micropillar (height = 1.2 μm and diameter = 0.3 μm), respectively. The input light is assumed to be a plane wave and the calculations were realized for the excitation wavelength of 532 nm. (e) Comparison of light intensities distributions along z-axis (data extracted from the yellow dashed lines in (b) and (d)). *Inset* of (e): zoom in of the intensity distribution at the center of the microsphere and the micropillar ($z = 0$).

secondary emission (for example Au NPs) is located at a maximum of the field, its radiation will be largely enhanced. A clearer comparison between the fields inside the sphere and the pillar is made and shown in Figures 4.2(e). We can see that, at the center of the two cavities, the intensity in the sphere is enhanced by 3 times comparing to the incident light, while that in the pillar increases 15 times. It is clear that a small change of position of the NP can lead to a significant change in the coupling of the NP in the cavity.

4.2.3 Plasmonics/photonics coupling

After verifying the coupling of the excitation light into the cavities, we studied further the interaction between the LSPRs of Au NPs and the amplified field inside the cavities. We performed a simulation in which a Au NP with a diameter of 50 nm was

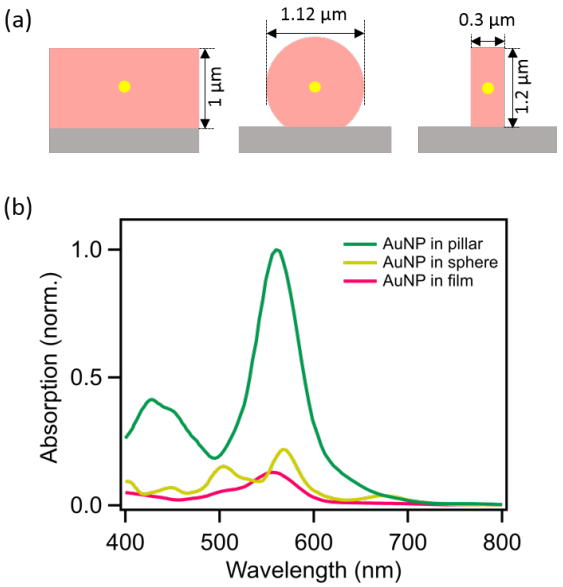

FIGURE 4.3: Theoretical calculation of plasmonic-photonic coupling. (a) Simulation models: a single Au NP (diameter = 50 nm) located in a SU8 film (thickness = 1 μm), a SU8 microsphere (diameter = 1.12 μm) and a SU8 micropillar (height = 1.2 μm and diameter = 0.3 μm). The excitation source is a continuous laser beam (wavelength = 532 nm) placed inside the cover glass. (b) Numerical simulation of absorption spectra showing a coupling between localized plasmonic effect of a single Au NP and a photonic structure.

introduced at the center of the cavities ($z = 0$). A case where a Au NP was embedded inside a SU8 uniform film was also taken into accounted for reference. Figure 4.3(a) illustrates the simulation models in those three cases. In this simulation, the source used is a total-field scattered-field source that surrounds the entire structures. The wavelength of the source ranges from 400 to 800 nm. An analysis group bounds the Au NP, allowing the calculation of its absorption. Figure 4.3(b) shows the calculated absorption spectra of the Au NP embedded in between the structures in three cases. For the Au NP inside the SU8 uniform film, the obtained spectrum is similar to the one shown in Figure 4.1(a), since the SU8 layer of 1 μm-thickness can be almost considered as an infinite medium with respect to the Au NP. The resonance peak locates at 553 nm. However, in the case of sphere and pillar, we found critical changes. The absorption spectrum of the Au NP inside the microsphere possesses two peaks, one at 567 nm and the other at 500 nm, and with enhanced absorption. Meanwhile, it is clear that the spectral profile in the case of micropillar is remarkably enhanced compared to the other cases. These modifications in the optical characteristics of the

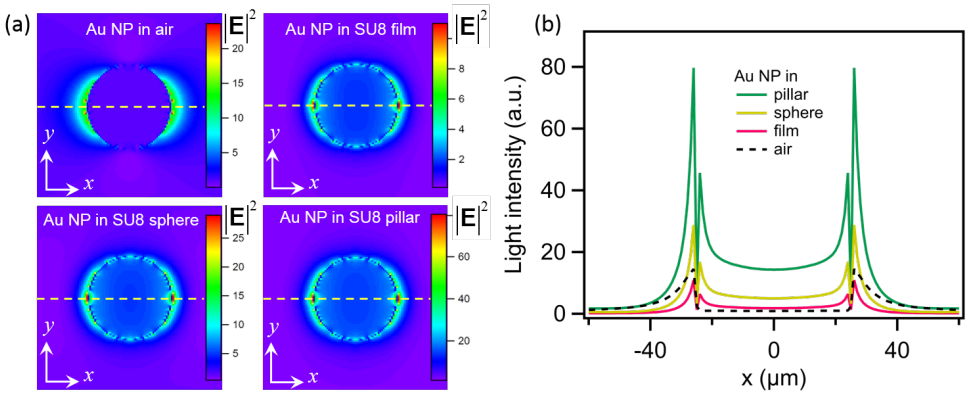

FIGURE 4.4: (a) Electric field distribution around a single Au NP (diameter = 50 nm) that is located in air, in a SU8 film (thickness = 1 μm), in a SU8 microsphere (diameter = 1.12 μm) and in a SU8 micropillar (height = 1.2 μm and diameter = 0.3 μm), respectively. (b) Comparison of light intensity distribution in four cases (data extracted from the yellow dashed lines in (a)), showing a strong light enhancement near the Au NP due to plasmonic/photonic coupling effect.

Au NPs must be attributed to the amplified field within the photonic cavities experienced by the Au NPs, as well as the particle field that is due to the LSPR of the Au NP. More specifically, the Au NP located at the center of the sphere experiences a much lower electromagnetic field compared to the one inside the pillar (as shown in Figure 4.2(e)), resulting in an enhancement of the resonance peak. This is also confirmed by the calculated electric intensity distribution at the position of Au NPs in those structures, shown in Figure 4.4. In this case, a linear polarized (along x–axis) plane wave source with the excitation wavelength of 532 nm is used. The source is also placed under the structure and inside glass substrate, pointing upward in z direction. A monitor bounding the NP is set to record the field in (xy)-plane. It can be seen that the Au NP inside the micropillar experiences the highest field, while that in the case of SU8 film is the lowest, even lower than in the air. This is in good agreement with what we have done so far. Obviously, for the case of microsphere, the best configuration is to locate the Au NP at the edge of the sphere, where the field is maximum. However, within the scope of this work, we limited the investigation to the case where the Au NP was inserted at the center of the microsphere.

4.2.4 Enhanced light out-coupling

Finally, we investigated how the emitted light is coupled out of the cavity. In this case, instead of a Au sphere, the Au NP is modeled as a single oscillating electric dipole (same as a single emitter) whose orientation is parallel to the interface between SU8 and glass substrate, corresponding to the excitation polarization at the focusing spot, since the emission from a small isolated spherical Au NP depends on the excitation field [142]. We also assumed that the emitted wavelength is $\lambda = 650$ nm, which is arbitrarily chosen within the fluorescence spectrum of Au NPs. This wavelength does not necessarily correspond to the maximum fluorescence spectrum, however it does not affect the generality of the calculation method either. Three particular configurations were taken into accounted for simulations: a single Au NP embedded in a SU8 film, a SU8 microsphere, and a SU8 micropillar (structures and parameters are presented in Figure 4.3(a)). For all three cases, we assumed that the oscillating dipole is located in SU8 photoresist at the distance of 500 nm from the interface between SU8 and glass substrate and the detector is located at the objective lens position (glass side).

Figure 4.5 shows the radiation patterns, *i.e.* the electric field intensity distribution in the (a) xz- and (b) yz-planes. It can be clearly seen that in the case of SU8 sphere, a significant portion of the emitted light is located in the vicinity of $\theta_c \simeq \arcsin(1/n_{\text{glass}}) = 41.2°$, which belongs to the collection cone of the microscope objective, and therefore could be detected. This portion is even larger in the case of SU8 pillar, which makes this shape the most desirable structure to couple NPs to. On the contrary, the radiation pattern in case the SU8 film is oriented at a larger angle, resulting in a loss of photons propagating out of the collection cone of the microscope objective. In order to explain these simulation results, we note that for small particles behaving like dipoles close to a dielectric interface, the radiated power is principally emitted towards the denser medium at the critical angle [143]. Since a SU8 film possesses a high refractive index $n_{\text{SU8}} \simeq 1.6$ with respect to that of glass substrate ($n_{\text{glass}} = 1.518$), the emission from the Au NP suffered a total internal reflection (TIR) effect, where all the emitted light at angles larger than the critical angle are completely reflected. In contrast, in the case of a Au NP embedded in a SU8 microsphere or micropillar, the Au NP is bounded by a small SU8 volume,

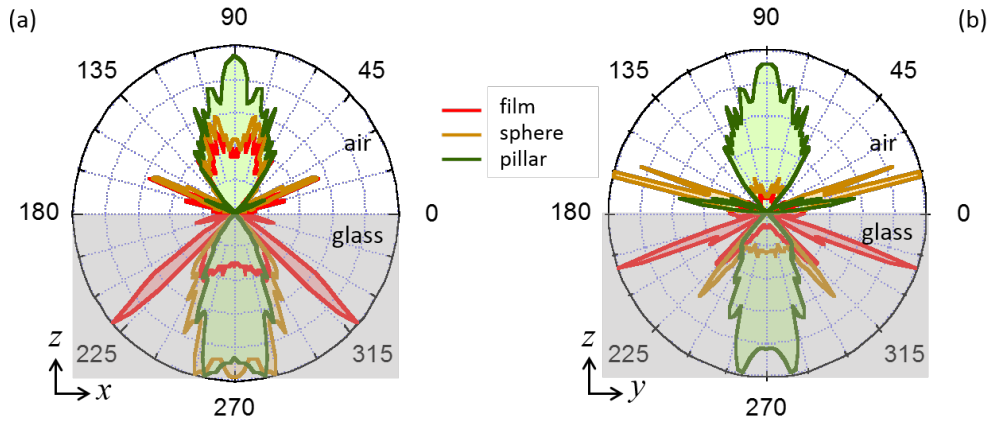

FIGURE 4.5: Simulation results of radiation patterns of a single emitter located in different structures: (a) emission diagram in the (xz)–plane and (b) emission diagram in the (yz)–plane. The emission dipole was assumed to be in $x-$direction.

surrounded by air, resulting in a low effective refractive index, as compared to that of glass substrate. Therefore there is no limitation caused by the TIR effect, the radiated light is transmitted into the glass substrate and most of it is then collected by the microscope objective. Certainly, we cannot directly compare the experimental results with the numerical calculations as we have simplified the coupling by considering a Au NP as a single electric dipole. A complete model and full mathematical calculation may be necessary for future investigation of such coupling of emitted light out of cavities.

4.3 Coupling of a single gold nanoparticle to a polymer-based photonic structure: experimental demonstration

As discussed above, PSs containing active molecules or fluorescent NP have become of great interest and many kinds of coupling structures have been studied and reported. However, the fabrication of such kind of coupling structures still remains a great challenge since it requires complex and expensive techniques. The simple LOPA DLW technique [44, 45] allows us to address most kinds of NPs and to precisely embed them into desired polymeric PSs with a double-step process [144]. In

this section, we describe that experiment process as well as the theoretical and experimental results.

4.3.1 Characterization of gold nanoparticles

The 50 nm-diameter Au NPs used in this chapter were bought from Sigma-Aldrich Corp. The absorption spectrum of Au NPs in water is measured and shown in Figure 4.6(a). The plasmon resonance peak appears at 539 nm. In our investigation, a green laser of 532 nm is ideal to excite the localized plasmon resonance of Au NP, promising a large of interesting phenomena of Au NP/microsphere structure. Figure 4.6(b) shows the fluorescence of Au NPs in water under an excitation light at 532 nm. By using a 580 nm long-pass filter, all the photons with wavelength larger than 580 nm are supposed to be collected by the OL of the DLW setup.

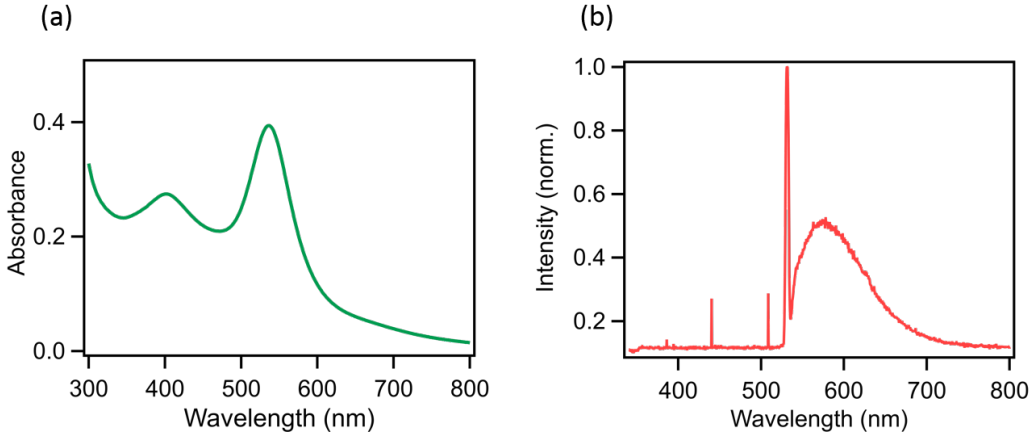

FIGURE 4.6: (a) Absorbance spectrum of 50 nm gold nanopartice in water. The plasmon resonance peak achieved at wavelength of 539 nm. (b) fluorescence spectrum of Au NPs, excited by a CW laser at 532 nm

In this work, due to the plasmonic resonance of gold NPs in the visible spectrum, with the use of a 532 nm laser and a confocal system, a single gold NP position can be easily determined at very low laser power. Hence, using the same LOPA system, the fabrication process of our structure can be divided into two steps as shown in Figure 4.7:

- Positioning Au NPs at low power

- Fabrication of desired structures containing Au NP at high power (due to the low absorption of SU8 at the wavelength of 532 nm)

4.3.2 Sample preparation

The glass substrate cleaning step follows the same process as decribed in Chapter 2. The spin coating process includes three short steps as shown in Figure 4.7:

- Spin coating of layer 1 of SU8
- Spin coating of Au NPs
- Spin coating of layer 2 of SU8

For coating materials, we used SU8 2000.5, and commercial Au NPs presented above. The Au NPs solution was diluted by mixing with distilled water, with a water/Au solution ratio of 3:1. Before spin coating, the diluted Au NPs solution must be ultra sonicated for 15 minutes so that the NPs are uniformly distributed in the solution. The sample consisting in a thin monolayer of Au NPs sandwiched between two SU8 layers was prepared by spin-coating. First, a layer of SU8 2000.5 was spin-coated on a cleaned cover glass. Second, 50 μL of a diluted and perfectly dispersed Au NPs solution was spin-coated on the surface of the first layer. Then, the second layer of SU8 2000,5 was spin-coated on top of the Au NPs layer. Note that, after each step, the sample was soft-baked on a hot plate at 65°C (3 mins) and 95°C (5 mins) to remove the residual solvents. A total film thickness of around 1.0 μm and a smooth surface profile were subsequently confirmed by a profilometer.

The table below presents all parameters for each step of spin coating:

Table 4.1: Sample preparation parameters

	Speed (rpm)	Acceleration (rpm/s)	Time (s)
SU8 (1)	1500	200	30
Au NPs	1000	200	30
SU8 (2)	1500	200	30

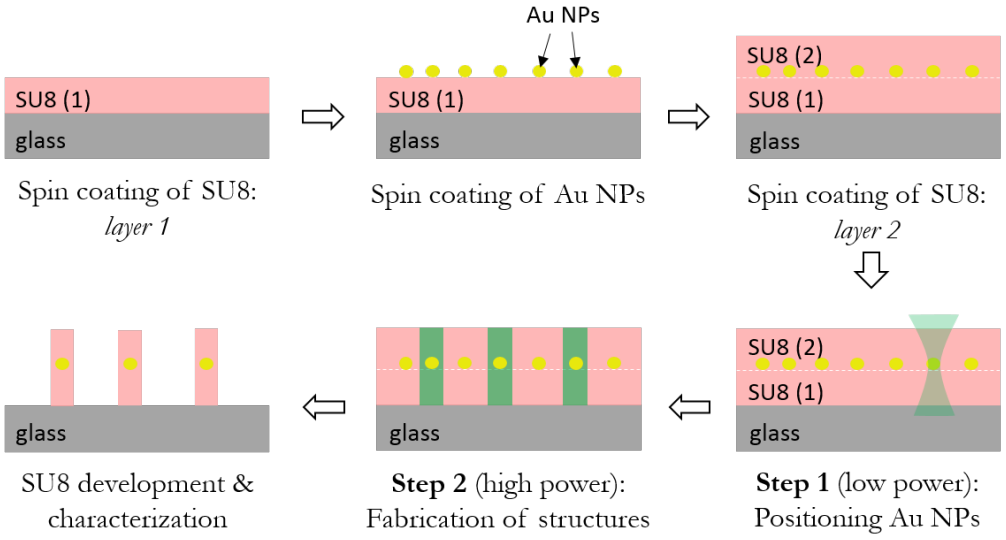

FIGURE 4.7: The process flow of the fabrication of photonic structures containing NPs by LOPA DLW.

4.3.3 Precisely positioning a single NP

The fabrication process starts with the mapping step in which we aim to precisely position single Au NP sandwiched between two layers of SU8. First, as mentioned before in Chapter 2, the interface of the glass subtrate and the sandwiched layers must be determined by scanning an arbitrary xz or yz plane. Then we can get the exact position of the interface, where we will later do the xy scanning. We note that Au NPs emit fluorescence in the visible range when excited by UV or visible (plasmonic resonance) light. Fluorescence images of Au NPs were obtained by raster scanning the sample through the focusing spot. Due to the high absorption of Au NPs at the used wavelength (Figure 4.6(a)), a very low excitation power (less than 0.1 mW, or less than $0.0022\text{W}/\mu\text{m}^2$ at focusing region) was employed. The power used for this step, on one hand, must be high enough so that we can distinguish the fluorescence signal of Au NPs to that of SU8, hence precisely addressing the single Au NP within the diffraction limit ($\approx$ 250 nm at $\lambda = 532$ nm), and on the other hand, must be sufficiently weak in order not to affect the solubility of the working SU8 region, i.e., no structure is formed during the mapping process. The distribution and separation of particles on the site depends mainly on the concentration of the particle in solution and the ultra-sonic processing.

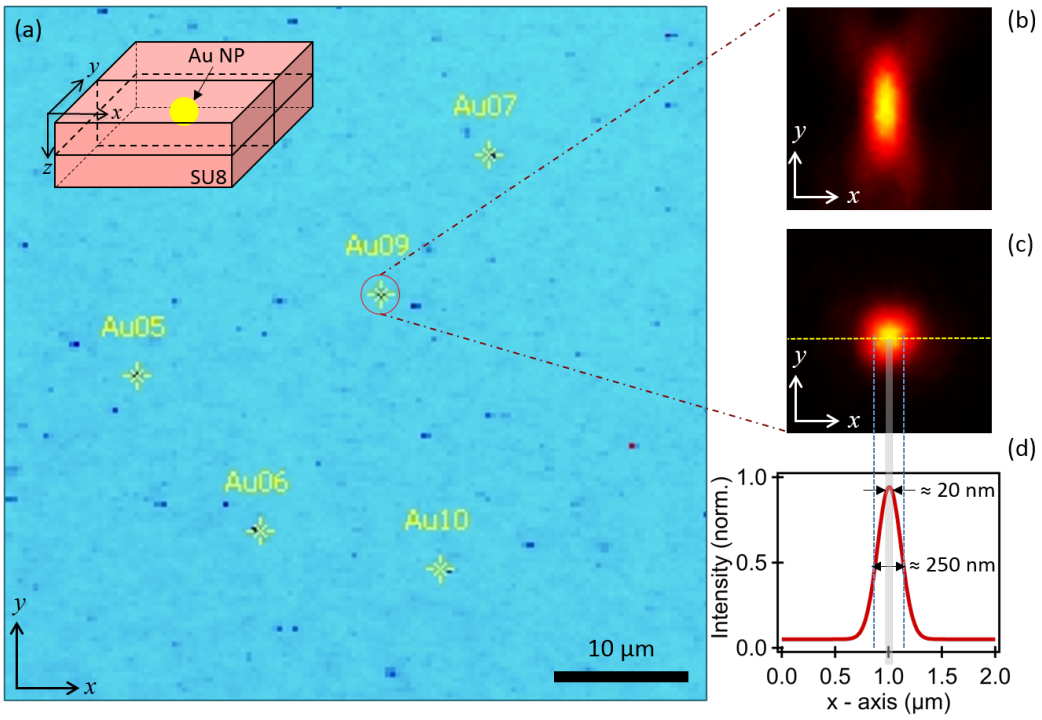

FIGURE 4.8: (a) Mapping in (xy)–plane for a large area. The yellow crosses indicate the position of single Au NPs. The Au NPs, which are selected to fabricate structures, were scanned again individually to determine precisely their positions. Inset shows illustration of a sample area in which a gold NP is sandwiched in between SU8 films. Fluorescence scanning is achieved in the (xy)– and (xz)–planes, as indicated by the red border rectangles. (b) and (c) Fluorescence images obtained by scanning along the (xz)– and (xy)–planes, respectively. (d) Extract of data corresponds to the dotted line shown in (c) showing the fluorescence intensity as a function of the NP position and of the precision of its position determination.

First, a large area (100×100 (μm^2)) of the sample was scanned and many individual Au NPs were found (Figure 4.8(a)). We then pointed out the position of each NP by scanning a small area of 2×2 (μm^2) around the NP, in the (xy)– and (xz)–planes, respectively, as shown in the Inset of Figure 4.8(a). We achieved a lateral resolution of about 243 nm (Figure 4.8(c)), and an axial resolution of 730 nm (Figure 4.8(b)), which actually corresponds to the diffraction limit of the used objective lens. The curve plotted in Figure 4.8(d) is an extract of data corresponding to a scan along the dotted line passing by the center of the NP (Figure 4.8(c)), showing the fluorescence intensity as a function of position. The sharp peak reveals a precision < 20 nm for the position determination.

4.3.4 Embedding single NP into PC

Once the position of a single NP is determined, the fabrication of PSs containing this NP will be realized. For the fabrication step, the excitation power was increased due to the ultralow absorption of SU8 photoresist at 532 nm excitation wavelength. In this work, we have chosen a power of 4 mW for all fabrications. The target structure is made of micropillars arranged in a hexagonal 2D photonic crystal. The NP was chosen to be located at the central pillar of the hexagonal structure. The fabrication of each pillar was realized by scanning the focusing spot along the vertical direction (z–axis) and through the total SU8 film thickness (total moving distance of 2 μm). In this work, we did not aim to investigate the effect of the periodic microstructure, so the geometric parameters of the micropillars pattern were chosen to keep the photonic bandgap (if any) of the micropillars hexagonal structure remote from the emission band of the Au NP embedded inside the structure. The micropillar pattern was made here only to ensure the accurate localization of NPs by identifying the pillar containing the single Au NP. After the exposure step, the sample was post-baked on a hot plate at 65°C (3 mins) and 95°C (5 mins) to finalize the cross-linking process, followed by a development step. We note that the PEB step also affects the quality of the fabricated structures and will be discussed in the next part. The patterned sample was then placed again on the PZT stage, at the same position as in the fabrication step, in order to perform optical characterization and comparison.

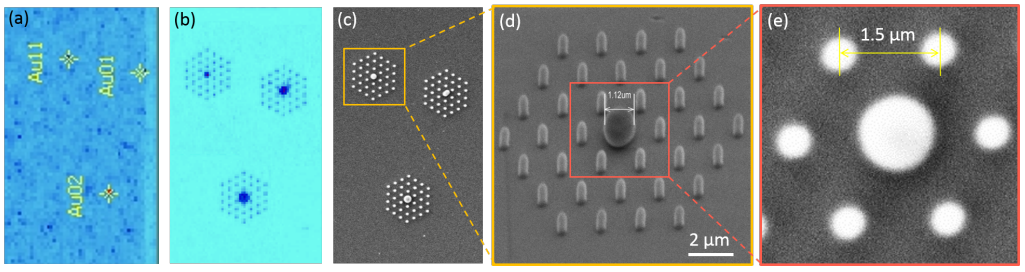

FIGURE 4.9: (a) Fluorescence image of Au NPs before fabrication. (b) Fluorescence image of corresponding fabricated structures. (c) SEM image of fabricated structures, each contains a Au NP at the center. (d) and (e) Zoom in images of a fabricated structure containing a single Au NP.

Figure 4.9(b) shows the fluorescence image of three fabricated patterns corresponding to three Au NPs in Figure 4.9(a). The morphology and surface topography of each structure was subsequently examined by optical microscopy and scanning

electron microscopy (SEM). Figure 4.9(c) shows the SEM image of those three fabricated patterns, each of which contains a single Au NP at its center. We expected to obtain a micropillar containing a single Au NP. From the zoom images of a structure (Figure 4.9(d) and (e)), surprisingly, it can be seen that a microsphere was formed at the position of the NP instead of a micropillar. In our samples, all micropillars patterns have the same parameters (center-to-center distance of 1.50 μm, diameter of each pillar of about 0.32 μm and the height of a pillar = 1.00 μm), the microspheres at the center display different diameters varying from 0.76 to 1.40 μm. Figures 4.9(d) and (e) show SEM images of a hexagonal structure, in which a quasi-sphere with a diameter of 1.12 μm and containing a single Au NP was obtained at the structure center.

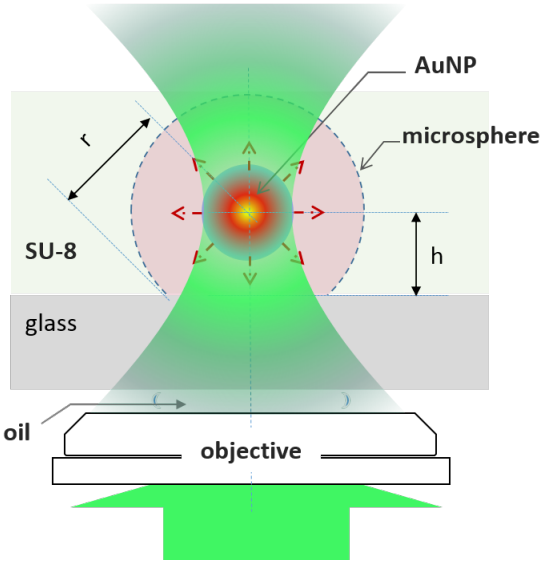

FIGURE 4.10: Sketch of exposure process and thermodynamic model used for explanation of thermal accumulation effect, which induce the polymerization within a spherical shape volume.

The formation of the microsphere can be explained by a thermodynamic model shown in Figure 4.10. During the continuous irradiation by the focused laser beam, Au NP strongly absorbs green light due to the strongly localized surface plasmon resonance. The absorption energy decays mainly non-radiatively via electron-phonon collisions followed by phonon-phonon relaxation. As a result, the NP is continuously heated and radially diffuses heat beyond its surface to the surrounding medium [145, 146]. Meanwhile, SU8 photoinitiators within the focal spot absorb one-photon energies from the incident light to generate a certain number of strong

acids (Lewis acid). The Au NP at that time plays the role as a “hot spot": in the vicinity of the Au NP, the temperature is noticeably increased, then accelerate the generation rate of acids. Since heat is diffused according to a spherical symmetry, the polymerization rate of SU8 is much higher in a sphere centered on Au NP. As long as the temperature is high enough ($> 75°C$), the SU8 polymer chains are continuously formed [147]. As a result, a spherical structure of a polymerized photoresist was obtained during the fabrication process. The amount of heat generated by the plasmonic NP can be controlled by the particle size and shape, as well as illumination strength, wavelength and irradiation duration. Hence the interplay of the Au NP with the excitation light allows the spatial and temporal heat management leading to controllable fabrication processes. With this given experimental setup, there are two possible ways for controlling the sphere size: either by excitation intensity or by exposure time. It is worth mentioning that the formation could be out of control if light intensity is too high, because the temperature at the Au NP position can exceed its deformation point (such as melting point, fragmentation threshold) [146]. In such a case, heat storage may result in a micro-explosion. In this work, fabrication parameters were the same for all structures and weaker than those of damage threshold, but the microsphere diameter varied from 0.76 to 1.40 μm due to the variation of the Au NPs size. It is important to mention that the microsphere is not the PS that we intended to fabricate. However, as it was theoretically predicted in precious sections and will be experimentally shown later, such photonic microsphere could be a valuable PS for the enhancement of NP optical properties. In general, when working with NPs without thermal effects, such as diamond NP, nonlinear NP, etc., this very simple LOPA-based two-step technique should allow one to fabricate structures as desired, including microspheres.

4.3.5 Effect of PEB on the quality of structures

Since the formation of structure containing single Au NP is due to the thermal effect, the fabricated structure was not always spherical. Besides, in the standard fabrication process, the exposure step is followed by a post-exposure bake (PEB) step, in which the sample is put on a hot plate for 1 minute at 65°C and then 3 minutes at 95°C, in order to finalize the crosslinking process of SU8. We found experimentally that a micro–explosion occured frequently at the position of the

Au NP. This phenomenon can be attributed to the excessive heating during the PEB step. As discussed above, due to the localized surface plasmon resonance of the Au NP at the wavelength of 532 nm, the Au NP played a role as a hot–spot and radially diffused heat to the surrounding medium, leading to the higher rate of generation of photoacids. Then the heat provided by the hot plate during PEB contributed to that process, resulting in the excessive diffusion of the photoacids into non-exposed area. In Chapter 2, we have demonstrated that the traditional PEB step can be replaced by the optically thermal induced effect caused by the use of a cw laser (local PEB), which immediately completes the crosslinking process at the exposed area. The local thermal effect allows us to obtain smaller and more uniform structures, as compared to the conventional PEB method. We note that in this case, the structures can only be obtained if the laser power is higher than a certain value.

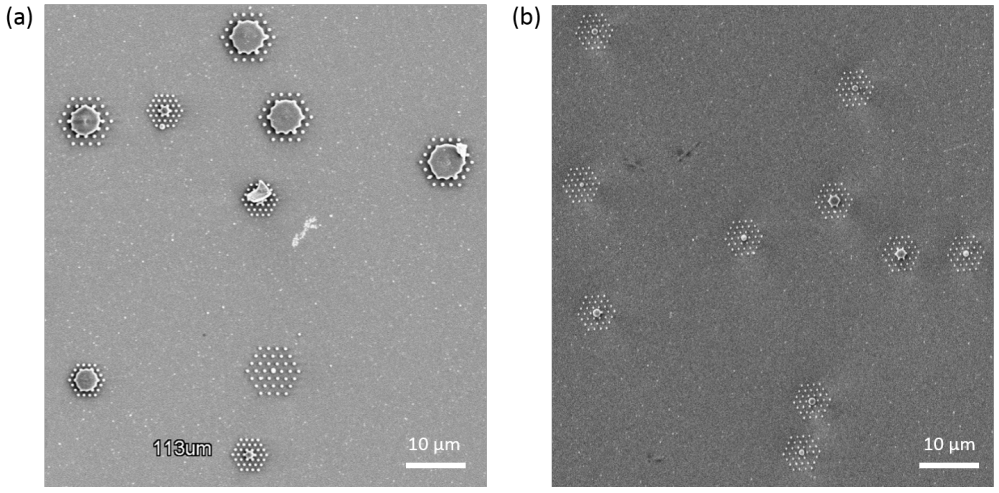

FIGURE 4.11: Comparison of structures fabricated with standard PEB on a hot plate (a) and local PEB (b). Each structure contains a single Au NP at the central pillar.

Figures 4.11(a) and (b) show SEM images of two sets of patterns fabricated with standard and local PEB, respectively. It can be clearly observed that for the sample realized with standard PEB (fabrication power = 4 mW, scanning speed = 2 μm/s), explosion occurred in more than half of the total fabricated patterns, whereas for the other sample, all patterns were well created even if the laser power used for fabrication is higher (fabrication power = 5 mW, scanning speed = 2 μm/s). This implied the advantages of local PEB, *i.e.*, it helps to avoid the excessive heating as

well as to reduce the fabrication time (since the standard PEB step is removed). We note that, despite the advantages of local PEB, a too high laser power can still lead to an explosion, since the temperature at the exposed region arises as the power increases. Moreover, although we have skipped the standard PEB step, the structures containing Au NPs still appear to be in spherical shape, which confirms that the formation of such shape indeed has the origin from the LSPR of the Au NP.

4.3.6 Characterization: Fluorescence measurement

In order to evaluate the NP/PS coupling, after the development step, the sample was placed back to the same position on the PZT stage to measure the fluorescence signal emitted by the NP embedded inside the microsphere. Each pattern was scanned again, using the same excitation power as in the mapping step. By doing this, we could clearly confirm the existence of a single Au NP inside the microsphere. Moreover, by comparing the fluorescence signal obtained before (Au NP embedded in SU8 films) and after fabrication (Au NP embedded in a microsphere), we could verify the fluorescence enhancement, thanks to the NP/PS coupling.

Figure 4.12(a) shows the fluorescence images of the fabricated structures, using the same excitation power as in the mapping step. It is obvious that the emission spot at the structure center is very bright as compared to the weak emission of the surrounding micropillars. Note that SU8 micropillars also emit fluorescence, but with a much lower rate. Figure 4.12(b) shows a zoom on the fluorescence image of the microsphere only. This clearly confirms the existence of a single Au NP inside the microsphere. Furthermore, by comparing the fluorescence signal obtained before fabrication (Au NP embedded in SU8 films) and after fabrication (Au NP embedded in a microsphere), we found a strong enhancement. The green and red curve in Figure 4.12(c) represent the fluorescence intensity of the same Au NP, obtained before and after fabrication, respectively. For a sphere with a diameter of 1.12 μm (Figure 4.9(d)), we estimated a six-fold enhancement of the collected fluorescence rate. For all other structures, the enhancement factor varies between 3.0–fold and 6.0–fold, due the difference of the microspheres sizes. This fluorescence enhancement should be a consequence of different coupling effects (in-coupling, out-coupling, plasmonic

coupling), as shown previously in theoretical calculation section. In practice, it is however difficult to clearly separate the contribution of each coupling.

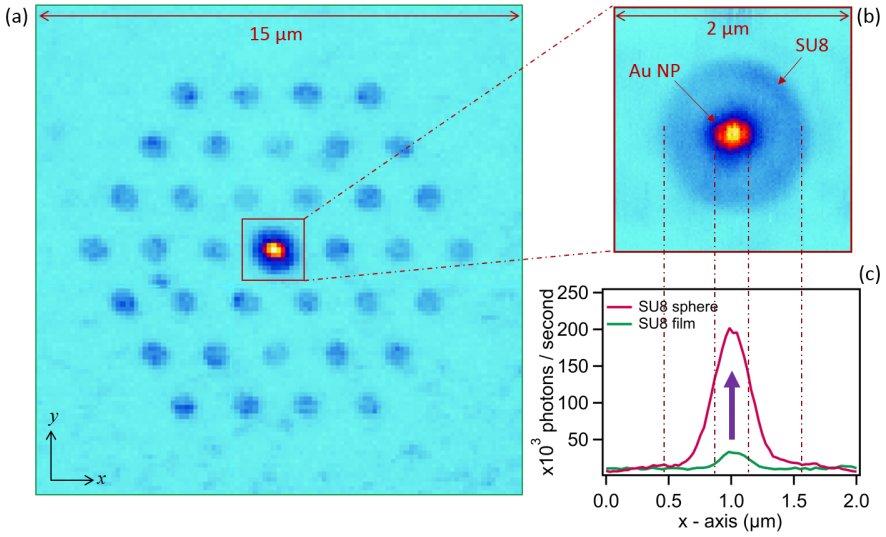

FIGURE 4.12: (a) Fluorescence images of fabricated structures obtained in (xy)–planes. (b) Fluorescence image of the microsphere containing a single Au NP. The single Au NP is locked at the center offers the very high intensity counts with respect to those of nearby SU-8 host medium surrounded by air. (c) Comparison of fluorescence signals in two cases, Au NP in microsphere (red curve) and in unpatterned SU-8 photoresist film (green curve).

4.3.7 Influence of gold particle sizes

We investigated further the influence of the NP size on the NP/PS coupling by realizing the fabrication and measuring the fluorescence enhancement of Au NPs of different sizes: 10, 30, 50, 80, and 100 nm. All fabrication parameters were kept the same for each NP size. Figures 4.13(a-e) shows the comparison of the fluorescence signals collected before (green curves) and after (red curves) fabrication. In other words, it is a comparison of fluorescence signal emitted by the same single Au NP when it is located in an uniform medium and when it is coupled to a microcavity. Figure 4.13(f) shows the average photons number emitted by Au NPs of different sizes in SU8 film (green bars) and SU8 microsphere (red bars) as well as the average gain of fluorescence (black marks). The photon collection enhancements recorded for each particle size are 12.9 ± 2.5, 12.6 ± 5.6, 3.9 ± 2.7, 5.9 ± 4.4, and 6.6 ± 5.1 times, respectively. It can be seen that the highest average photon collection

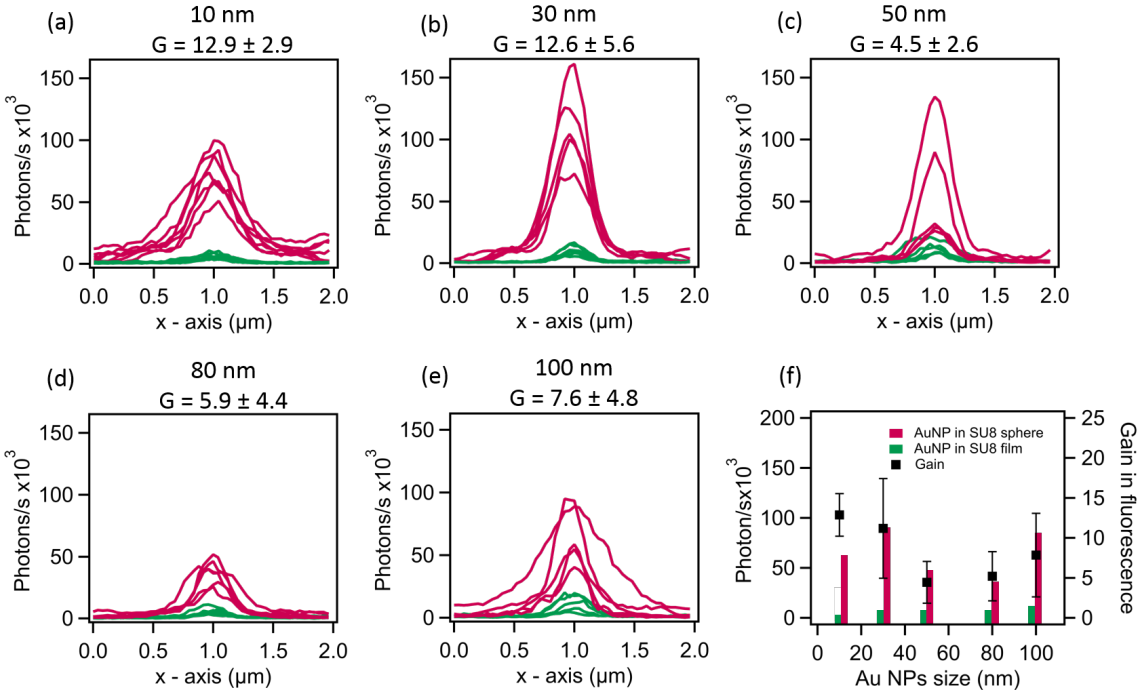

FIGURE 4.13: Comparison of fluorescence signals of Au NP in a microsphere (red curves) and in an unpatterned SU8 photoresist film (green curve). Au NP sizes are: (a) 10 nm; (b) 30 nm; (c) 50 nm; (d) 80 nm; and (e) 100 nm. G indicates the average fluorescence enhancement factor. (f) Comparison of average gain of fluorescence of different sizes of Au NPs in a microsphere.

corresponds to Au NPs of 10 nm-size, while it reaches a minimum value for Au NPs of 50 nm-size. The highest gain in fluorescence that we obtained, corresponding to a 10-nm gold NP, reached up to 36.6 times, which is remarkably high. The trend of fluorescence enhancement in relation with NP size might be related to the surface plasmon resonance spectra of those NPs, as well as the volume ratio between metallic NP and polymeric microsphere. However, due to the thermal induced polymerization effect, the fabrication did not always produced the same result, and it is quite difficult to quantify the influence of different fabrication parameters. This requires more investigations in order to understand correctly about the fluorescence enhancement or plasmonic NP/PS coupling. Certainly, deterministic embedding of a single Au NP into polymeric microstructures by LOPA DLW technique is very interesting to realize fundamental study of ultrafast light modulation effect as well as application in biosensor via plasmonic effect [141]. Besides, fabrication of a polymeric structure containing a single emitter, such as quantum dot or single nitrogen-vacancy color

center in diamond [148,149], should be an ideal way to investigate NP/SP coupling, which opens the way for quantum applications.

4.4 Conclusion

In conclusion, we have demonstrated theoretically and experimentally the precise coupling of a single Au NP into a photonic microstructure using LOPA-based DLW technique. Simulations based on FDTD method have proved the mechanism of the coupling of the excitation wavelength into cavities, the plasmonics/photonics coupling, and the coupling of the emitted light out of cavities, which predict the enhancement of the fluorescence signal of Au NPs. The coupled NP/PS was realized by a LOPA DLW technique, and with a double-step process: ultralow excitation power for determination of NP position, and low excitation power for the fabrication of desired microstructures. We encountered an unexpected effect due to the heat induced by the SPR of the Au NPs during the fabrication: instead of a micropillar containing a NP, we obtained a microsphere. However, the coupling of NP to the microsphere allowed a great enhancement of the fluorescence signal as compared to the case without coupling, which is in good agreement with the theoretical prediction. Au NPs with different sizes have been investigated and the highest gain in fluorescence that we obtained, corresponding to a 10-nm gold NP, reached up to 36.6 times. This LOPA-based DLW with a double-step process is very simple but powerful as compared with other complicated and expensive techniques. It is also very promising to embed other NPs into desired polymer-based PSs, such as diamond NPs containing a single emitter, thus allowing the manipulation of single photon emission, or non-linear NPs to improve second harmonic generation signal.

Chapter 5

Controlled coupling of KTP nanoparticles into photonic structures

5.1 Introduction

Second harmonic generation (SHG) is a nonlinear optical process, in which photons with the same frequency interacting with a nonlinear material are effectively combined to generate new photons with with a frequency at 2ω. Involving exclusively virtual electronic states, SHG does not include energy absorption, then avoiding bleaching usually observed with fluorescent and luminescent nanoparticles. Therefore, it is possible to achieve observations over long durations with no decrease in the signal quality. In contrast to fluorescence, the light emission spectrum of the SH radiation is distinctly separated from the excitation spectrum, allowing efficient spectral filtering and therefore a better contrast in microscopy. Moreover, SHG is a non-resonant process which can occur for a large range of excitation wavelength [150–152]. Thus, excitation wavelengths can be selected in spectral ranges where the biological tissue absorption and scattering are low so that photo-damage is limited and penetration depth increased [153], which can bring several benefits for bio-imaging.

Nanosources emitting SHG signal have been widely studied since no phase-matching is required when working at the nanoscale [154–157]. Besides, for several applications, such as sensor or biomarkers, nonlinear NPs should be used [15,16]. Several studies have been devoted to SHG organic nanosources, such as nanocrystals of CMONS [158–161] and hybrid organic/inorganic-based nanoparticles $MnPS_3$ [162]. The SHG of this type of nanosources is efficient because the 2-photon excitation is close to a resonance of the quantum system, and the radiation emitted by these nanosources comprises both a SHG signal and a two-photon fluorescence. This double emission was analyzed by a technique of nonlinear ellipsometry which makes it possible to characterize these nano-emitters in their environment [163,164]. In particular, it is possible to sort nano-assemblies non-centrosymmetric molecules to study their degree of crystallinity, and evaluate order or disorder within them. However, the resonant excitation at two photons leads to the phenomenon of "photobleaching", which corresponds to a weak change of the molecule structure, but sufficient to change its electronic properties of fluorescence [165, 166]. This photobleaching phenomenon varies the intensity of the second harmonic radiation, making this type of nano-emitter difficult to use.

One of the most popular materials in nonlinear optics is the $KTiOPO_4$ (KTP). The KTP crystal is a very commonly used material in optics thanks to its important nonlinear response, and its ability to realize the condition of phase matching for a wide excitation spectral range [167]. The studies on this material have mainly concentrated on its optimal growth to obtain crystals of large size without defects, leading to many uses in the physics of lasers [167]. Recently Loc Le Xuan et al. [168] have successfully synthesized and characterized KTP nanoparticles (NPs), with the size varies between 30 and 100 nm. The analyses of these NPs were carried out under different conditions, and the result shows that the SH signal, under femtosecond excitation, is perfectly stable, and that the coefficients characterizing the second-order nonlinear response for the massive KTP crystal remain relevant for particles in this size range. It was also demonstrated that, despite their nanometric size, KTP NPs have a very good degree of crystallinity.

In this chapter, we first integrate a pulsed laser at 1064 nm to the LOPA DLW setup to study the SHG signal of the KTP NPs. Then, we investigate the coupling of a single KTP NP into PSs by embedding them into polymeric structures of different

shapes and sizes, with the NP position being controlled. Finally, we demonstrate theoretically and experimentally the enhancement of the SHG signal thanks to the coupling of the fundamental light and the PS.

5.2 Characterization of KTP NPs

In this section, using our own setup, we verify again several characteristics of the KTP NPs.

5.2.1 Experimental setup

In order to measure and to characterize the SHG signal of KTP NPs, we aligned a second laser into the LOPA DLW setup. It is a pulsed laser operating at the wavelength of 1064 nm (pulse duration of 1 ns and repetition rate of 24.5 kHz). This second laser is aligned so that the laser beam coincides with that of the 532 nm laser. A flip-flop mirror allows us to switch easily from one laser to the other. The experimental setup is shown in Figure 5.1, which is basically the same as the LOPA setup. We use a half-wave plate and a polarizer to adjust the power of the laser. A second half-wave plate (not shown in the Figure) can be placed after the polarizer to control the polarization of the excitation beam. The beam is collimated and directed to enter the same microscope. To collect SHG signal at 532 nm, an infrared filter is used to cut off the excitation light at 1064 nm. The signal is then detected by either the APD, which gives a SHG image or a spectrometer which gives a SHG spectrum of the KTP NPs. This home-built setup is very flexible for signal detection as well as structure fabrication at LOPA regime.

5.2.2 Sample preparation

KTP nanocrystals used for experiments were obtained by sorting the nanocrystals from a KTP powder recovered at the end of a flux growth process used for the growth of massive crystals.

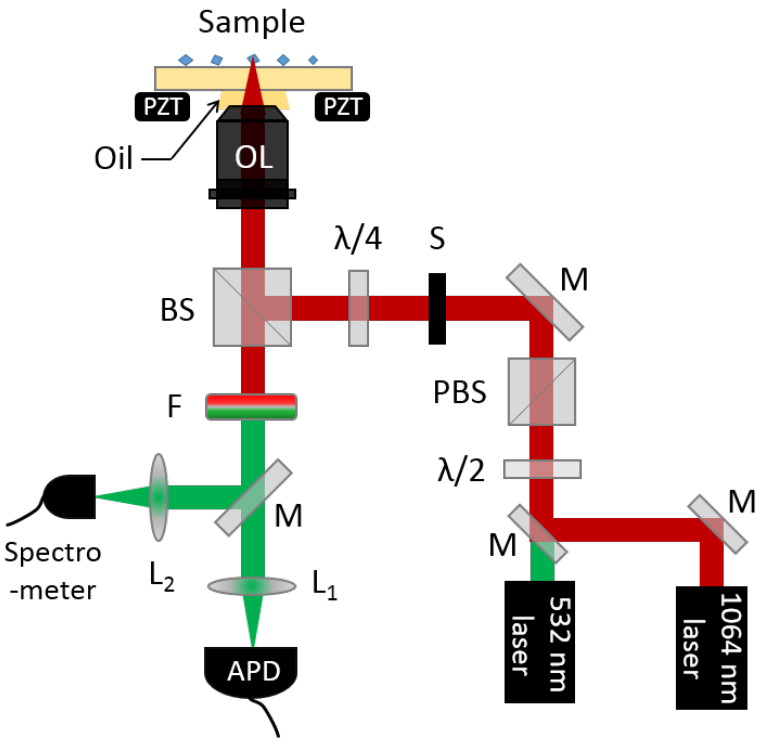

FIGURE 5.1: Experimental setup of the integrated setup for SHG measurement. PZT: piezoelectric translator, OL: oil immersion microscope objective, $\lambda/4$: quarter-wave plate, $\lambda/2$: half-wave plate, BS: beam splitter, PBS: polarizer beam splitter, M: mirror, S: electronic shutter, $L_{1,2}$: lenses, F: infrared filter, APD: avalanche photodiode.

The sample preparation process described below was done by our colleague [168], we used the final solution to conduct our experiments. The synthesis process can be summarized as follows:

The KTP powder is mixed with a polymer (polyvinylpyrrolidone, PVP) in a controlled concentration solvent (propanol, PrOH). The solution is then placed for 20 minutes in an ultrasonic bath, thereby disaggregating the particle assemblies and promoting the formation of a layer of polymer around the particles. This layer prevents the particles from aggregating again. At the end, we obtain a colloidal solution of KTP nanoparticles. The solution obtained is then passed through a particle filter, the diameter of the holes being 1 μm, in order to eliminate the largest particles and then placed in a glass pellet placed in a centrifuge. To obtain a monodisperse solution of controlled size, with particles whose size is between 30 and 150 nm, it is necessary to eliminate the larger particles and also particles too small to be able to

be detected optically and which would distort the estimation of size of the assembly. To eliminate the larger particles, we typically centrifuge for 5 to 15 minutes at 11000 rpm. During this centrifugation, particles larger than typically 150 nm, and therefore the heaviest, will migrate towards the bottom of the pellet, leaving the smallest nanoparticles in the colloidal solution. To remove the smallest particles, the reverse procedure is used: the solution is centrifuged for 60 minutes at 11000 rpm so that only particles smaller than 30 nm remain in the solution. We remove the supernatant from this solution and only the particles with a size between 30 and 150 nm remain in the bottom of the centrifugation pellet. We disperse these particles again in the 0.1% PVP/PrOH mixture, the mixture then being placed in an ultrasonic bath to obtain the final colloidal solution.

To characterize a single KTP NP, we first diluted the solution by adding ethanol with the solution/ethanol ratio of 1:5. The diluted solution was then put into an ultrasonication bath for 30 minutes to well disperse the KTP NPs. The solution obtained after ultrasonication was spin-coated on a clean glass substrate (detailed procedure in Chapter 2), which was then put into our setup for characterization.

5.2.3 Emission signal of a single KTP NP

We use the linear and nonlinear optical properties of KTP given in the reference [169]. At the wavelength of 1064 nm, both one-photon and two-photon absorptions of KTP are negligible [170]. The size of the particles, between 30 nm and 100 nm, is sufficiently small as compared to the excitation wavelength to neglect, at least as a first approximation, the effects due to chromatic dispersion, such as, for example, the effect of the phase tuning, or those due to a possible anisotropic shape of the NP.

For these KTP NPs, we can use the dipolar approximation, as detailed in Appendix C. The emission of a KTP NP will be approximated by dipole associated with the nonlinear second order response induced by the excitation field $\mathbf{E}$, whose expression is given by:

$$\mathbf{p} = \epsilon_0 \chi^{(2)} \mathbf{E}\mathbf{E}, \tag{5.1}$$

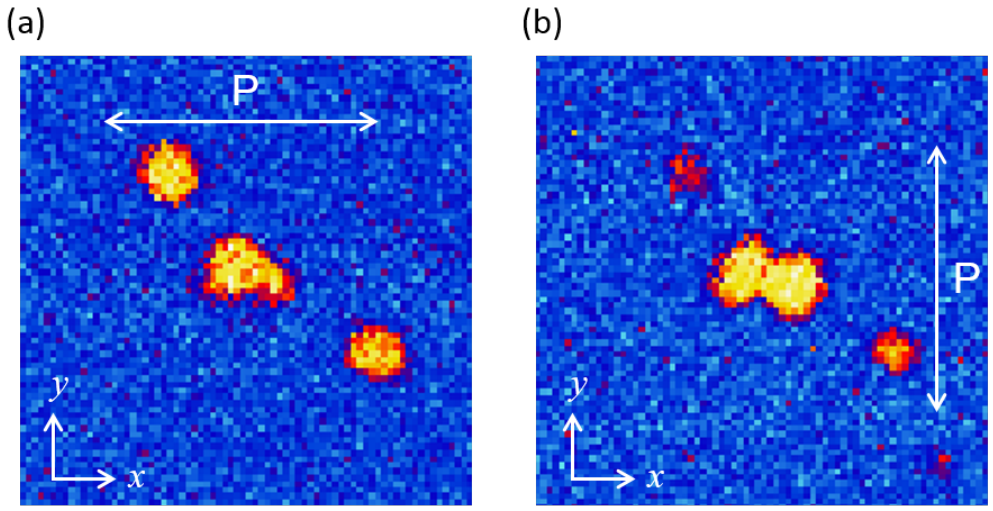

FIGURE 5.2: Scanning image in second harmonic microscopy for a sample of KTP nanoparticles. (a) image obtained with a horizontal polarization, (b) with a vertical polarization. The nanoparticles are revealed differently in the two images.

with spatial components:

$$p_i = \epsilon_0 \sum_{j,k} \chi^{(2)}_{ijk} E_j E_k. \tag{5.2}$$

The second order susceptibility tensor $\chi^{(2)}$ of the KTP has a coefficient which greatly exceeds all other tensor coefficients $\chi^{(2)}_{ZZZ}$, where Z is the 3-fold of KTP. In a first approximation, we can therefore take into account only this $\chi^{(2)}_{ZZZ}$ coefficient. The induced nonlinear dipole is then reduced to:

$$p_Z = \epsilon_0 \chi^{(2)}_{ZZZ} E_Z E_Z, \tag{5.3}$$

and the nanocrystal responds only to the component of the field parallel to its axis Z, an excitation field perpendicular to this axis does not lead to significant SH emission. Therefore, when such a nanocrystal is scanned with a polarization in the focal plane, only the nanocrystals whose Z axis is close to the polarization of the incident field is revealed. A SHG image is shown in Figure 5.2. To reveal the entire distribution of the nanocrystals, it is therefore necessary to realize two scans with two perpendicular polarizations along the X and Y axes, or use a circularly polarized beam. However, for these types of excitation, the nanocrystals whose Z-axis is perpendicular to the plane of the sample can not be detected.

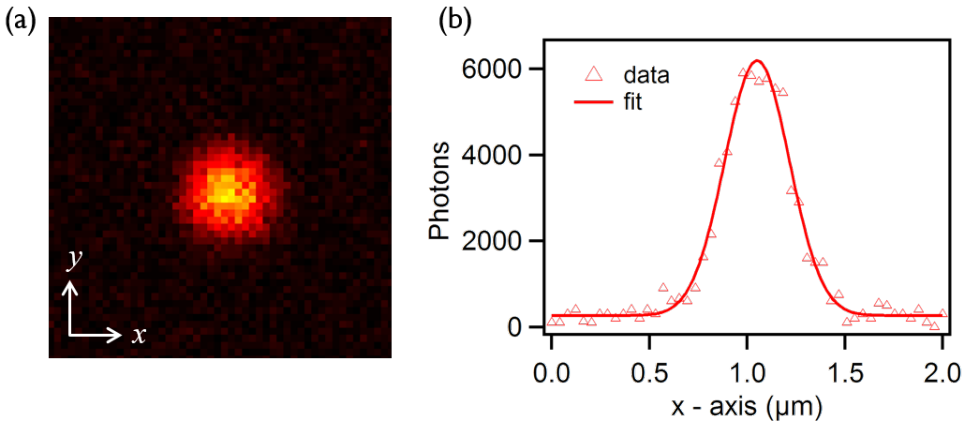

FIGURE 5.3: (a) SHG image of a KTP nanocrystal of size between 30 and 100 nm, obtained by scanning with the 1064 nm laser. (b) The profile in the x-direction with the FWHM of 500 nm.

In reality, KTP has five non-zero nonlinear coefficients (see Appendix C), so that a nanocrystal whose axis Z is perpendicular to the sample plane can also generate a SH signal thanks to the other coefficients of the tensor $\chi^{(2)}$. However this signal is generally low compared to the emission of the other nanocrystals whose axis Z is closer to the polarization of the incident field. In our setup, we use a quarter-wave plate to generate a circularly polarized beam, which allows the detection of the entire distribution of the NPs. Some SHG signals can be lower than in the case where we use linearly polarized beam.

For KTP nanocrystal studies, we typically use an average excitation power of 0.3 mW. A background in the image during scanning may be due to scattering of the excitation laser on the surface of the sample or on other optical elements, due to an emission of the various optical elements in the path of the beams, due to the light insufficiently reduced by the filters, or even by the shots of avalanche photodiodes.

For the infrared wavelength used, 1064 nm, the mid-height width of the focal spot of the infrared laser is d = 480 nm according to equation $d = 0.61 \times \frac{\lambda}{NA}$. This is evident in Figure 5.3, which shows a SHG image of an individual KTP nanocrystal. The profile graph in the x-direction (Figure 5.3(b)) shows clearly the FWHM of approximately 500 nm.

With an infrared filter, we can efficiently eliminate laser scattering and ambient light which is the most important contribution to the substance. This spectral

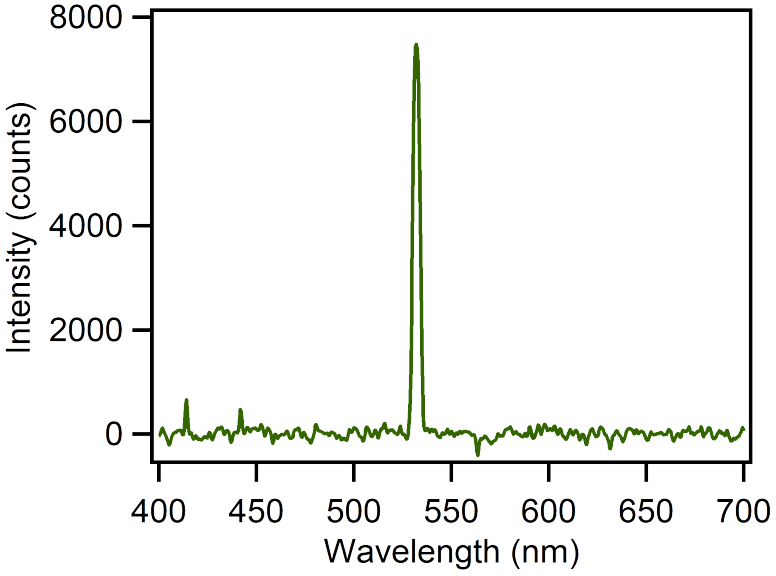

FIGURE 5.4: Spectral analysis carried out on a single nanocrystal of KTP showing an emission peak at 532 nm. The peak at 1064 nm corresponding to the excitation wavelength is cut off by using an infrared filter.

filtering to obtain images of very large signal-to-background ratio. On this typical image obtained in scanning, for an average incident power of 0.3 mW, we obtain a signal-to-background ratio of about 100. This gives us great ease to identify and analyze individual nanocrystals.

We now consider the second harmonic emission of a KTP nanocrystal depending on the excitation conditions.

Spectral analysis: Figure 5.4 shows the spectral analysis of the signal emitted by a KTP nanocrystal, with an infrared filter placed in the setup to cut off the wavelength of the excitation light. The signal collected is directed to a spectrometer by a tiltable mirror placed just in front of the photodiodes. A comparison between the spectrum obtained for a nanocrystal of KTP and the spectrum measured at a neighboring position on the same sample shown clearly the appearance of a single peak centered on 532 nm, corresponding to half of the wavelength of the excitation laser (1064 nm).

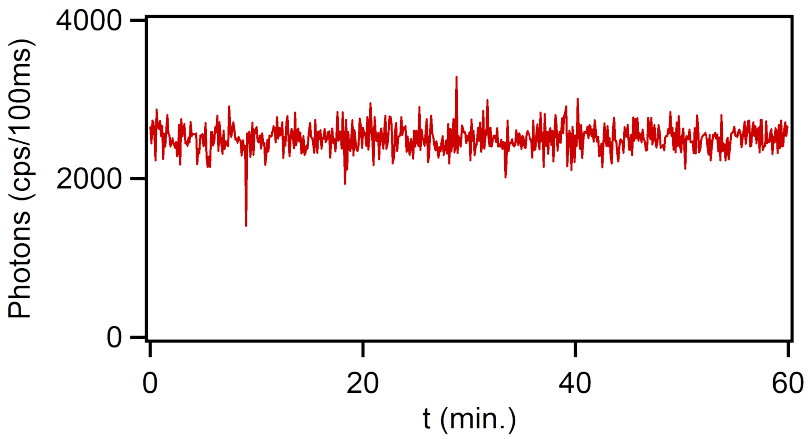

FIGURE 5.5: Time evolution of the SHG signal of a KTP NP under an excitation power of 0.3 mW. The signal is perfectly stable for a duration of one hour.

Stability of the SHG signal: According to the emission spectrum of a KTP nanocrystal excited at 1064 nm, two-photon fluorescence is not present. That means that the KTP nanocrystal is not excited in a real electronic state and that the SHG is non-resonant, as expected. Indeed, the KTP complex refractive index studies show an excellent transparency of this material at 1064 and 532 nm [170]. The non-resonant character of the SHG process is essential for the stability of the signal. Indeed, once the system is in a real excited state, it can generate photoinduced processes that degrade its ability to generate the signal, as is often observed for nonlinear organic crystals [171].

Figure 5.5 shows the temporal tracking of the second harmonic signal of a KTP nanocrystal excited at an average power of 0.3 mW. This experiment, like all the experiments we have carried out, has been carried out under ambient conditions. The graph shows a perfect stability of the signal for a duration of one hour, the small variation of the signal being due to the mechanical instability of the assembly. By using the structure of the sample to locate a given position on its surface, this perfect photostability allows us to find the same nanocrystal, from one time to another, and to perform different types of measurements, experiments that can be separated by several months.

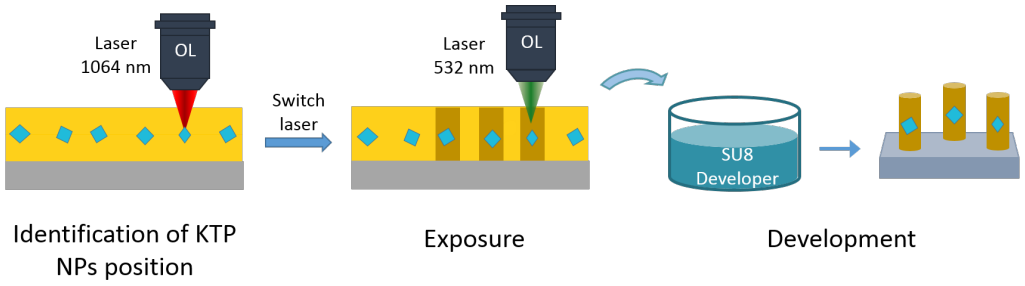

FIGURE 5.6: Fabrication process of polymeric structures containing single KTP NPs.

5.3 Controlled coupling of a single KTP nanoparticle into a polymeric photonic structure

5.3.1 Sample preparation and fabrication process

For fabrication, a sample consisting of a layer of KTP NPs sandwiched between two SU8 layers was prepared by spin-coating. First, a layer of SU8 was spin-coated on a cleaned cover glass. Second, 50 μL of a diluted and perfectly dispersed KTP NPs solution was spin-coated on the surface of the first layer. Then, the second layer of SU8 was spin-coated on top of the KTP NPs layer. After each step, the sample was soft-baked on a hot plate at 65°C (3 mins) and 95°C (5 mins) to remove the residual solvents. SU8 2000.5 was used for the fabrication of thin structures, and SU8 2005 or SU8 2025 for 3D structures.

Basically, the fabrication process of structures containing single KTP NPs shown in Figure 5.6 is quite similar to that with Au NPs. It consists of two main steps:

- Identification of the position of single KTP NP using 1064 nm laser
- Fabrication of the structure containing the NP using 532 nm laser

The only difference is that, the first step is carried out using the 1064 nm laser, and the image obtained is a SHG signal image. The intensity of the SHG signal of KTP NPs is also measured by the spectrometer at this step. After that, we switch to the 532 nm laser to fabricate the desired structures. We note that, the two lasers have

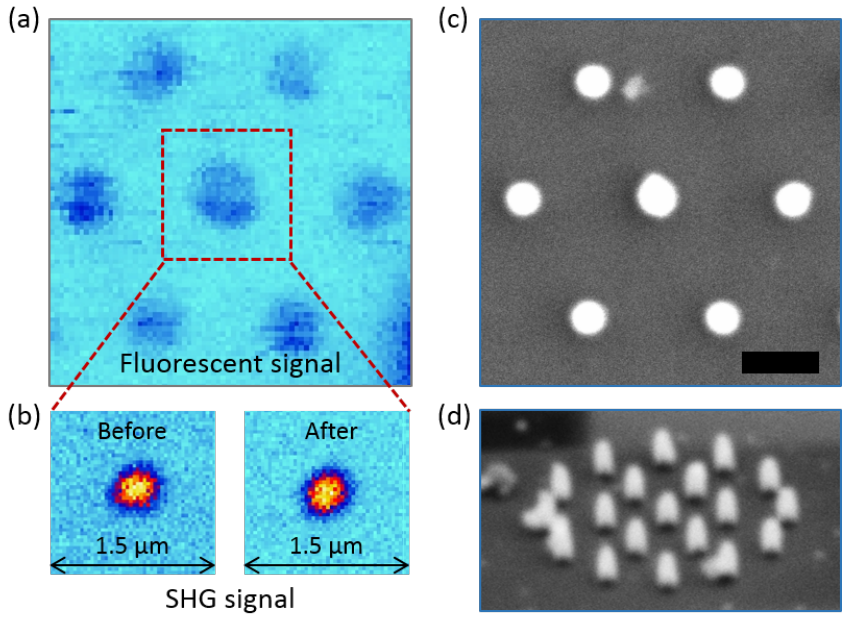

FIGURE 5.7: (a) Fluorescence image of the structure (obtained by scanning with 532 nm laser). (b) SHG image of the KTP NP before and after fabrication (obtained by scanning with 1064 nm laser). SEM images top view (c) and side view (d) of a structure containing a single KTP NP at the central pillar, all pillars were fabricated with the same excitation dose. Scale bar: 1 μm.

been aligned so that their focusing spots have the same x and y coordinates. For z coordinate, there is an unavoidable difference due to the difference in wavelength, but it can be easily overcome by just adjusting the z position in the fabrication program. After fabrication, as usual, samples are developed with SU8 developer to wash away all monomers. The fabricated sample is then placed again on the PZT stage, at the same position as in the fabrication step, in order to measure the SH signal of KTP NPs after fabrication and compare with that obtained before fabrication.

A SHG image obtained to determine the exact position of a KTP NP can be seen in Figure 5.7(b)-Before. This image is obtained with an average laser power of 0.3 mW. As shown in Figure 5.3(b), the sharp peak reveals a high precision for the position determination. After the position of a single KTP NP is determined, the fabrication of structures containing this NP will be realized. For this fabrication step, the 1064 nm laser is shut down and the 532 nm laser is turned on. The excitation power used for fabrication is set around 8 mW (for local PEB process). First, we fabricated a CPC structure with a NP located at the central pillar. The fabrication of

each pillar was realized by scanning the focusing spot along the vertical direction (z–axis) and through the total SU8 film thickness (total moving distance of 2 μm). All pillars, including the one containing the NP, were fabricated with the same exposure dose (P = 8 mW, v = 2 μm/s). After fabrication, the sample is developed and put back to the setup to characterize the SHG signal. Figure 5.7(a) shows a fluorescence image obtained by scanning the 532 nm laser (P = 50 μW). Figure 5.7(b) shows SH images obtained by scanning the 1064 laser at the position of the central pillar before and after fabrication. These SHG images confirm that the KTP NP is well embedded inside the central pillar. Unlike what has been observed with Au NPs in Chapter 4, there is no explosion with the pillar containing the KTP NP, which is evident in the SEM images shown in Figures 5.7(c) and (d). The SEM images (top view and side view) show that all pillars have the same size and height. We note that SU8 photoresist does not emit any fluorescent signal, or it is very weak, therefore, in the image scanned with laser 1064 nm after fabrication (Figure 5.7(b)), we observe only the SHG signal of KTP NP. The non-explosion effect is quite understandable since KTP crystal possesses a wide transparency range (350 nm - 4500 nm) [170]. Therefore, no energy is absorbed during the exposure of the 532 nm laser, leading to similar shapes for all pillars, with or without KTP NPs.

As compared to Au NPs, the fact that structures do not explode under laser exposure is a great advantage which can be exploited to study further the coupling of this NP to different kinds of structure. In the following parts, we demonstrate that using LOPA DLW technique, we can easily manipulate the structures containing single KTP NPs.

5.3.2 Control of size and shape of structures

First of all, the size of pillars containing single KTP NPs is taken into account. We fabricated a set of structures containing KTP NPs at different exposure doses as shown in Figure 5.8. The doses vary from P = 6 mW, v = 4 μm/s; v = 3 μm/s; v = 2 μm/s; v = 1 μm/s, to P = 9 mW, v = 4 μm/s; v = 3 μm/s; v = 2 μm/s; v = 1 μm/s. The diameter of the pillars containing the NPs increases with the step around 50 nm. We note that, the size of the central pillars can be controlled with

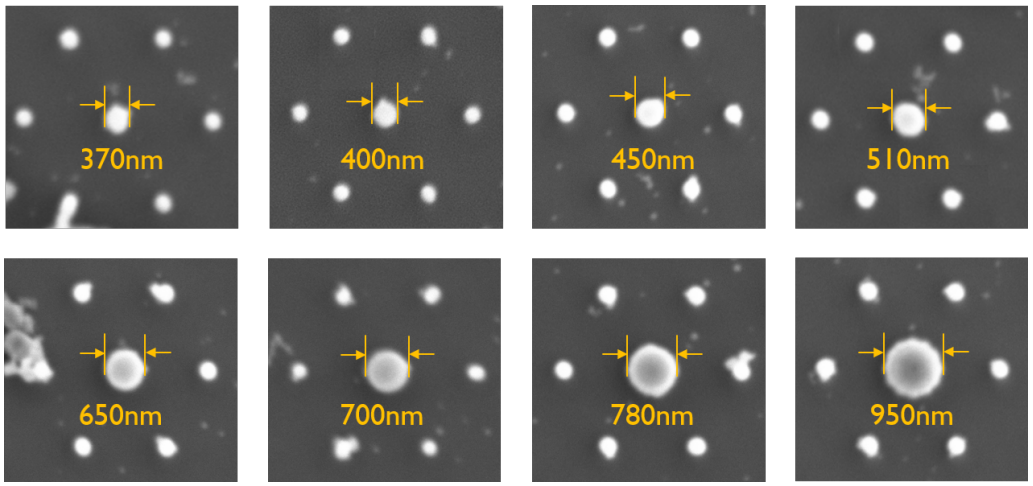

FIGURE 5.8: SEM images of structures containing single KTP NPs at the central pillars. Each central pillar was fabricated at different exposure dose. Top row, from left to right, respectively: P = 6 mW, $v = 4$ μm/s; $v = 3$ μm/s; $v = 2$ μm/s; $v = 1$ μm/s. Bottom row, from left to right, respectively: P = 9 mW, $v = 4$ μm/s; $v = 3$ μm/s; $v = 2$ μm/s; $v = 1$ μm/s.

a step even as small as 30 nm, which is a great advantage due to the non-explosion effect.

We investigate further the coupling of KTP NPs to structures by creating various structures in different shapes. Figures 5.9(c) and (d) show the top and side views of a square structure fabricated by an excitation power of 9 mW and a writing speed of 3 μm/s. This structure was created by scanning the focusing spot through the SU8 layer to form a point matrix arranged in square shape. The distance between two adjacent pillars was set at 150 nm, which resulted in continuous lines. Figure 5.9(a) show the fluorescence image of the square shape obtained by scanning the structure by the 532 nm laser (P = 50 μW), and Figure 5.9(b) presents the SHG image realized by scanning the 1064 nm laser, which shows only the SHG signal emitted from the KTP NP. Both images are taken after fabrication, proving that the fabricated structure contains a single KTP NP. Similarly, Figure 5.10 shows SEM, fluorescent, and SHG images of a triangular structure. This structure was created by the same way as the square structure, and the fluorescent and SHG images also show that it contains a single KTP NP at the center.

Furthermore, we are able to fabricate 3D structures containing a single KTP NP. In order to realize such kind of structure, we used SU8 2005 as the coating material.

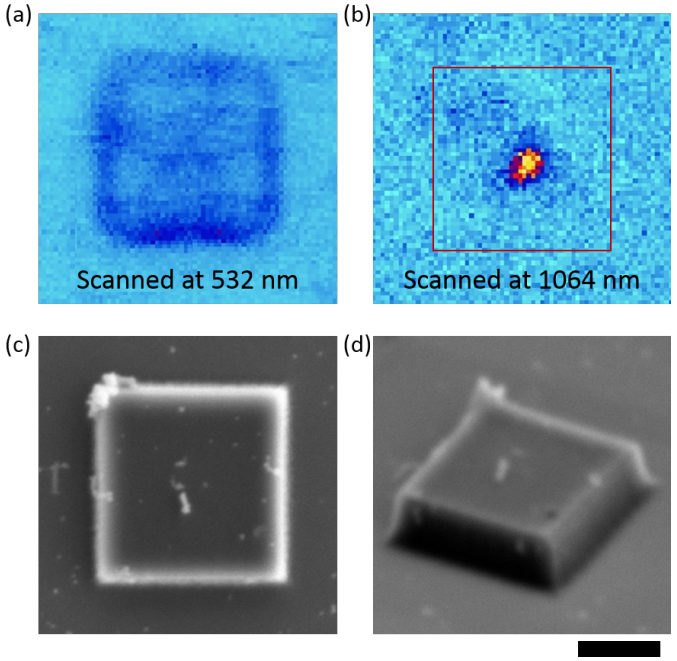

FIGURE 5.9: (a) Fluorescence image of a square structure containing a KTP NP (obtained by scanning with 532 nm laser). (b) SHG image of the square shape showing that it contains a KTP NP (obtained by scanning with 1064 nm laser). SEM images top view (c) and side view (d) of the structure. Scale bar: 1 μm.

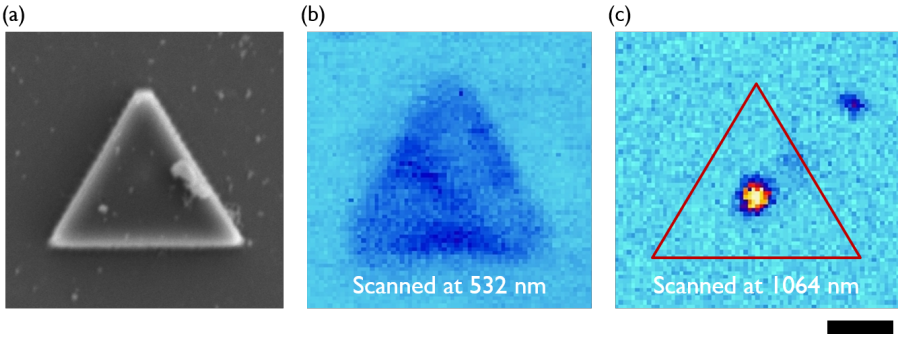

FIGURE 5.10: (a) SEM image of a triangular structure containing a KTP NP. (b)Fluorescence image of the structure (obtained by scanning with 532 nm laser). (c) SHG image of the triangular shape showing that it contains a KTP NP (obtained by scanning with 1064 nm laser). Scale bar: 1 μm.

A layer of KTP NPs was sandwiched between 2 layers of SU8. It is important to know the thickness of the first layer of SU8 in order to precisely determine the position of the NP layer. Figure 5.11(a) shows the SEM image of a 3D hexagonal air-hole membrane containing a KTP NP at the center. The membrane was fabricated at a laser power of 10 mW and a writing speed of 3 μm/s. It is supported with six

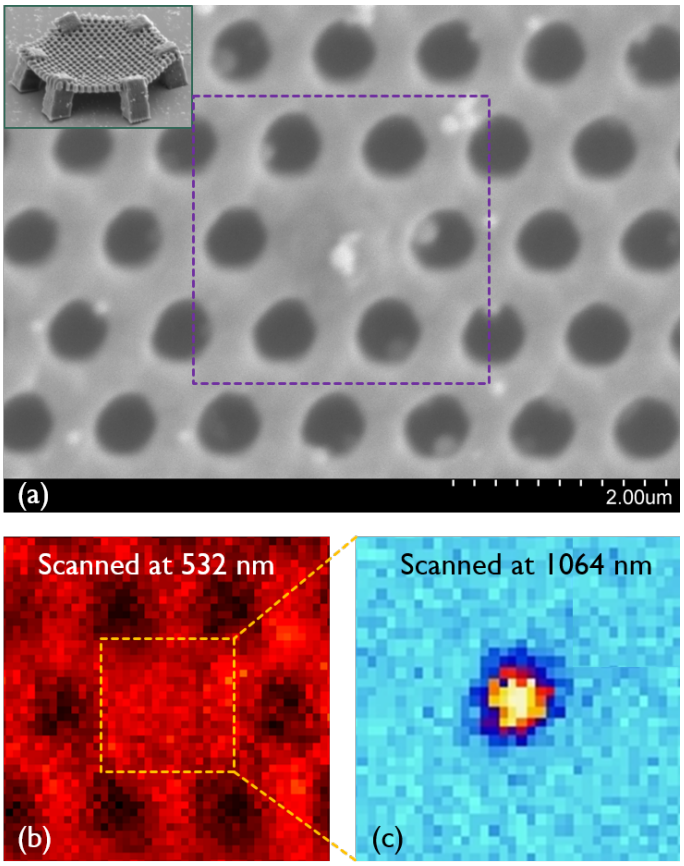

FIGURE 5.11: (a) SEM image of a 3D hexagonal membrane containing a KTP NP at the center; Inset: side view. (b) Fluorescence image of the structure (obtained by scanning with 532 nm laser). (c) SHG image of the structure center showing that it contains a KTP NP (obtained by scanning with 1064 nm laser).

legs in order not to be in contact with the glass substrate (see Inset). The presence of the NP in the structure was also confirmed by the SHG image obtained at the central part of the structure (see Figures 5.11(b) and (c)). It is more challenging to fabricate such 3D structures containing NPs compared to the case of 2D and 1D structures since it is more difficult to determine the position of the NPs in the case of 3D. However, 3D structures offer more interesting applications for the coupling with NPs, such as resonance cavity, photonic crystals, etc., therefore, hybrid 3D structures should be the target in the future. The first success to embed a KTP NP into a 3D structure can open a way to further investigations and more fascinating applications.

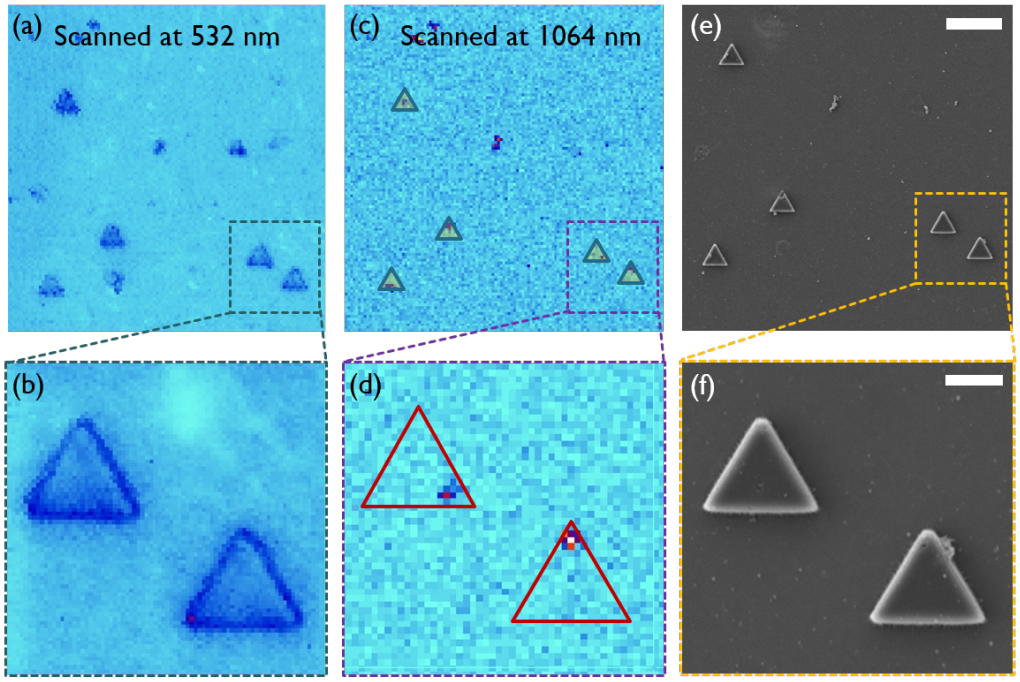

FIGURE 5.12: (a, b) Fluorescence images of a set of miro triangular structures (obtained by scanning with 532 nm laser). (c, d) SHG images of the structures showing that KTP NPs are embedded at different positions (obtained by scanning with 1064 nm laser). (e, f) SEM images of a the structures. Scale bars: 10 μm and 2 μm, respectively.

5.3.3 Control of position of NP in structures

The position of the NPs in structures is also of great importance since it decides the field intensity experienced by NPs in those structures. Therefore, we are also interested in precisely controlling and manipulating the position of a NP in structures.

We have fabricated several structures containing KTP NPs at different positions, which can be controlled by a Labview program. Figure 5.12 show fluorescence image, SHG image, SEM image and their corresponding zoomed images of a set of triangular structures, each of which contains a single KTP NP at a different position: top corner, bottom left, bottom right corner, or at the center. Figure 5.13 show a series of microdisk structures containing KTP NPs at positions from center to edge. Measurements show that the position can be controlled with the step down to 100 nm. Being able to control effectively the size and shape of structures as well as the position of NPs in structures makes LOPA DLW a powerful yet simple technique to embed any kind of NPs into PS.

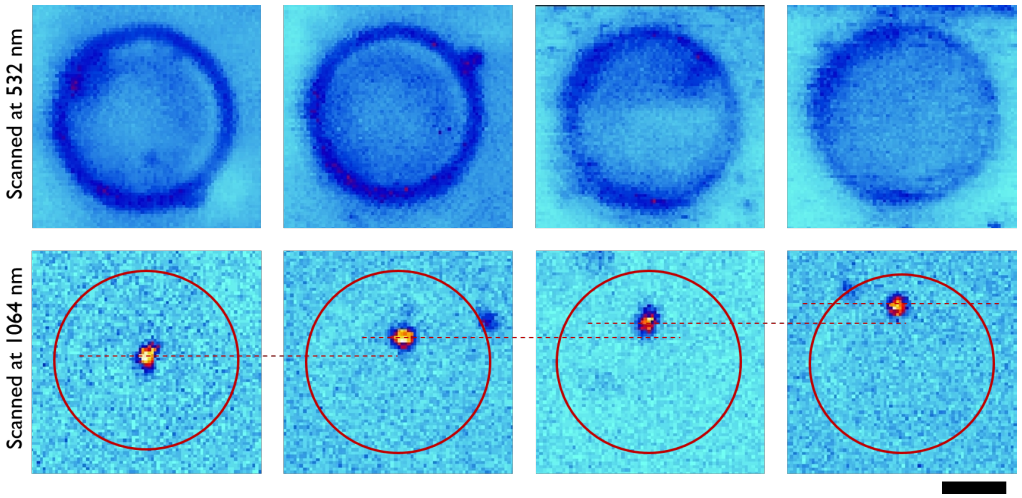

FIGURE 5.13: Top row: Fluorescence images of a set of microdisk structures (obtained by scanning with 532 nm laser). Bottom row: SHG images of the structures showing that KTP NPs are embedded at different positions, from center to edge (obtained by scanning with 1064 nm laser). Scale bars: 1 μm.

5.4 SHG signal enhancement

In this section, we investigate experimentally the enhancement of the SHG signal emitted by a single KTP nanocrystal embedded in a micropillar. We also use a simulation model based on FDTD method to explain the origin of this enhancement.

5.4.1 Experimental measurement

In order to study the enhancement of SHG signal, we are going to compare the signal strength of the KTP nanocrystal before and after being embedded into a structure. Each structure is scanned again using the same excitation power and the SHG signals are detected by both the APD and the spectrometer. Figure 5.14(a) shows the SHG images of a single KTP NP obtained with laser 1064 nm at 0.3 mW before and after fabrication, and a fluorescence image of the fabricated structures. It can be seen from the image scanned with laser 1064 nm after fabrication that the NP still exist inside the micropillar. As mentioned above, since SU8 does not emit fluorescent signal when excited by a wavelength of 1064 nm, we observe only the SHG signal of the KTP NP and we see no sign of the pillar in this image. However, when we compare the SHG signal intensity before and after fabrication,

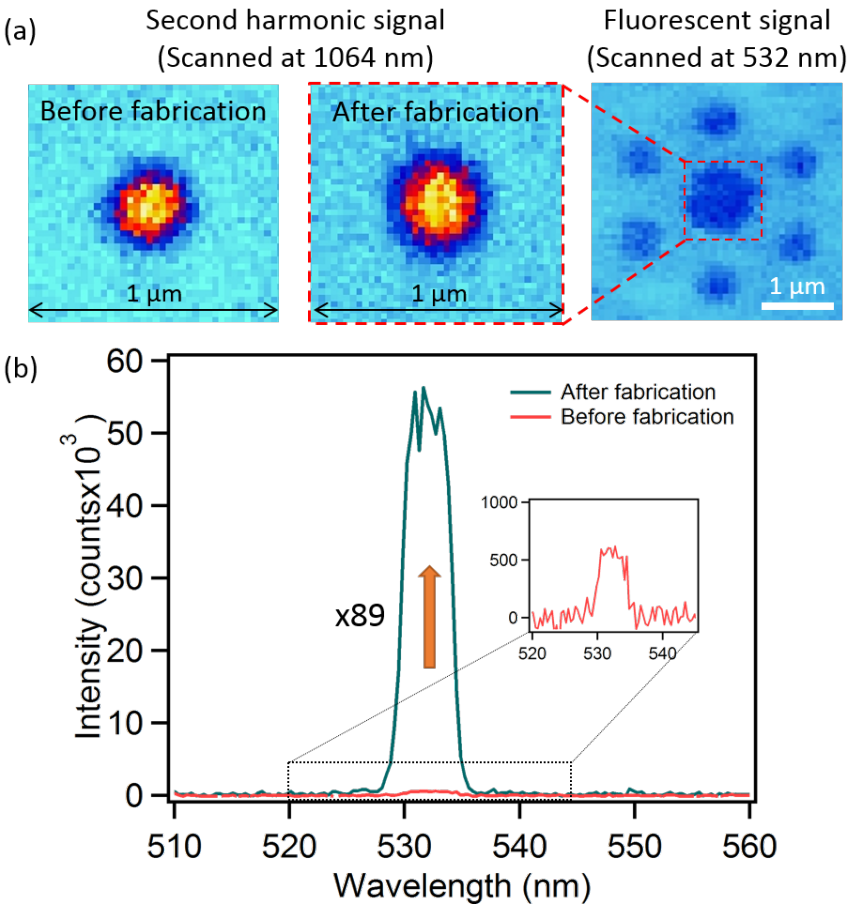

FIGURE 5.14: (a) SHG images before and after fabrication of a KTP NP (obtained by scanning with 1064 nm laser), and a fluorescence image of the fabricated structure (obtained by scanning with 532 nm laser). (b) SHG signal intensity of the KTP NP obtained before and after fabrication; Inset: zoomed graph of the signal before fabrication.

we can see clearly a great enhancement which can be attributed to the existence of the micropillar. Figure 5.14(b) shows the SHG signals intensity obtained with the spectrometer before (red curve) and after fabrication (green curve). For a pillar with a diameter of 800 nm and a height of 1.3 μm, we achieved an enhancement of SHG intensity of a KTP NP up to 90 times, as compared to that obtained with the same NP inside a SU8 film (thickness of 1.3 μm). We also fabricated many structures with the same parameters containing different KTP NPs to see if the structure size is the only factor that affects the SHG enhancement. The result is shown in Figure 5.15, which indicates a variety of enhancement values. This refers to another reason which can contribute to the enhancement of the SHG intensity besides the pillar cavity. Indeed, while the KTP massive crystal has a unique and well-defined orientation, a

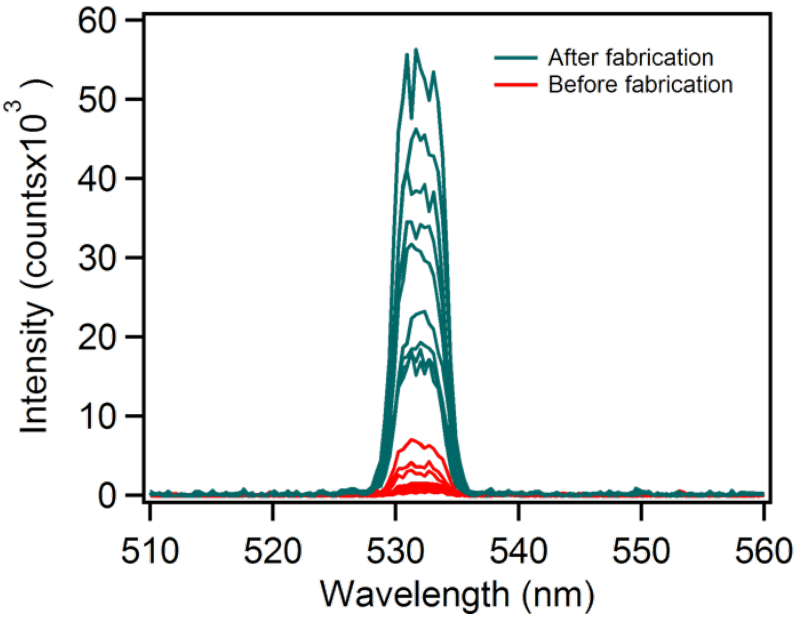

FIGURE 5.15: Comparison of SHG signals of different KTP NPs embedded in pillars with identical parameters before (red curves) and after fabrication (green curves).

KTP nanocrystal can have a perfectly arbitrary orientation in space. The amount of light that is collected in the numerical aperture of the microscope objective strongly depends on the orientation of the emitting dipole and the refractive indices. The signal strength of the spectrometer is therefore the product of the intensity actually emitted by the nonlinear dipole and the corresponding collection efficiency, which is defined as the ratio of the photons collected by the microscope to the total photons emitted by the dipole. In the next part, we will perform several simulations to explain the enhancement in the SHG signal.

5.4.2 Simulation model

5.4.2.1 Influence of the cavity

In this section, we perform various simulations using FDTD method to address different problems: How the fundamental light is coupled and enhanced in a cavity (pillar); How the SHG signal emitted from the NPs is guided out of the cavity, and how the coupling out is affected by the orientation of the NPs. In all these

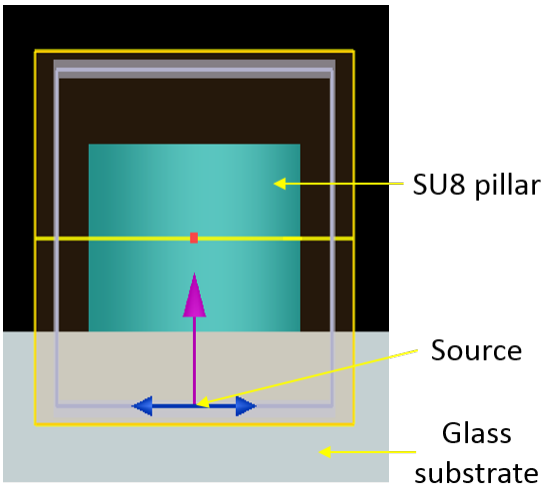

FIGURE 5.16: Simulation model of the coupling of the fundamental light into a pillar cavity. The sources emits a single wavelength at 1064 nm, $n_{glass} = 1.5$, $n_{SU8} = 1.58$.

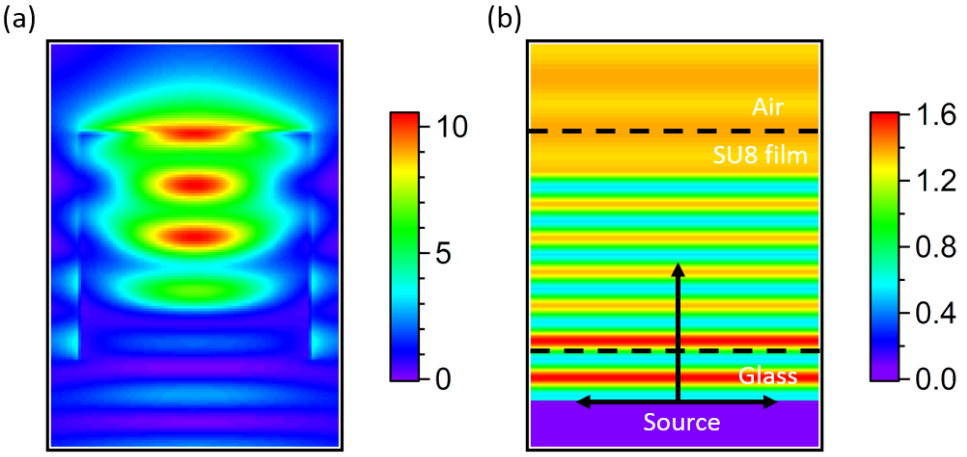

FIGURE 5.17: (a) Calculated field intensity (square modulus of the electric field) at the wavelength of 1064 nm inside a pillar with a diameter of 800 nm and a height of 1.3 μm. (b) Calculated field intensity at the wavelength of 1064 nm inside a SU8 film with thickness of 1.3 μm.

simulations, the emitted signal is simulated as an electric dipole, which radiates a single wavelength at 532 nm. By doing these simulations, we expect to explain the enhancement in the SHG signal observed during experiment.

First, we investigated the coupling of the fundamental light into the pillar cavity. A simple simulation model was built where the pillar cavity is placed on a glass

substrate, as shown in Figure 5.16. A plane wave source emitting wavelength at 1064 nm was placed underneath, pointing upward (in z direction). A monitor was set in the (xz)– or (yz)–plane to record the incident light field. A thin SU8 film on a glass substrate was also investigated using the same simulation model in which the pillar was replaced by a thin film. The coupling of the fundamental light into the cavity could be properly studied and compared with the field inside the film in these calculations. The cavity parameters (diameter, height) are swept in a large range in order to fully investigate the role of the cavity. It has been observed that just a small change in diameter or height (the sweeping step is 100 nm) can lead to a great difference of how the light is coupled into the cavity. These results can help predict the best parameters of any kinds of structure for different wavelengths. Figure 5.17(a) shows the square modulus of the electric field inside a micropillar with a diameter of 800 nm and a height of 1.3 μm when they are illuminated by a plane wave at 1064 nm. Similarly, the field intensity inside a thin film with a thickness of 1.3 μm illuminated by the 1064 nm incident light is illustrated in Figure 5.17(b). It can be clearly observed that, the field is amplified and localized along the height of the pillar. Comparing the field at the center of both structures where the KTP NP locates before and after fabrication, we can see that the field intensity in the pillar is amplified by 7 to 13 times with respect to that inside the thin film. A KTP NP locating at a maximum of the field inside the pillar will experience the fundamental field which is increased by 7 to 13 times, resulting in the enhancement of its SH radiation by 50 to 170 times. Besides, a small change of position of the NP can lead to a significant change in the enhancement of the SHG signal, which explains why the manipulation of the NP position in the structures is of great importance.

As mentioned above, the signal strength detected by the spectrometer is affected by not only the intensity actually emitted by the nonlinear dipole but also by the corresponding collection efficiency of the dipole. The SH intensity emitted by the nonlinear dipole can be enhanced by placing it in an amplified fundamental field originating from the coupling with a cavity as explained above. Meanwhile, the collection efficiency is affected by both the cavity configuration and the orientation of the emitting dipole. We will take these factors into account in the calculations.

To investigate how the emitted light is coupled out of the cavity, we model the nonlinear dipole as a single oscillating electric dipole (Figure 5.20(a)). In this

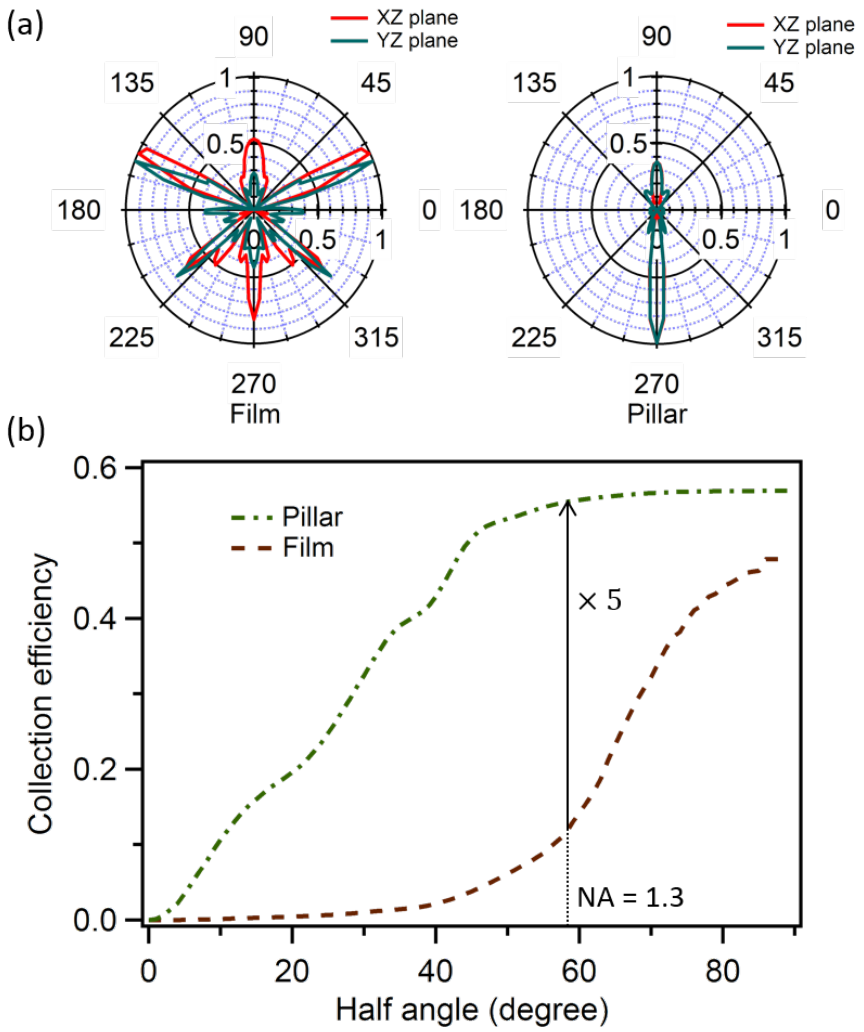

FIGURE 5.18: (a) Radiation patterns of a dipole located in different structures. Left: emission diagram in (xz) and (yz)–plane of a film structure. Right: emission diagram in (yz) and (yz)–plane of a pillar structure. The emission dipole was assumed to be in $x-$direction. (b) Calculation of the SH signal collection efficiency as a function of the half angle of the objective lens in two cases: KTP NP in a pillar and KTP NP in a thin film.

simulation, the dipole orientation is assumed to be parallel to the interface between SU8 and glass substrate, *i.e.*, $\theta = 90°$. Two particular configurations were considered for simulations: a single KTP NP embedded in a SU8 film (thickness of 1.3 μm) and a SU8 micropillar (diameter of 800 nm and height of 1.3 μm). For both cases, we assumed that the dipole is located in SU8 photoresist at the distance of 650 nm from the interface between SU8 and glass substrate and the detector is located at the objective lens position (glass side). Figure 5.18 shows the radiation patterns,

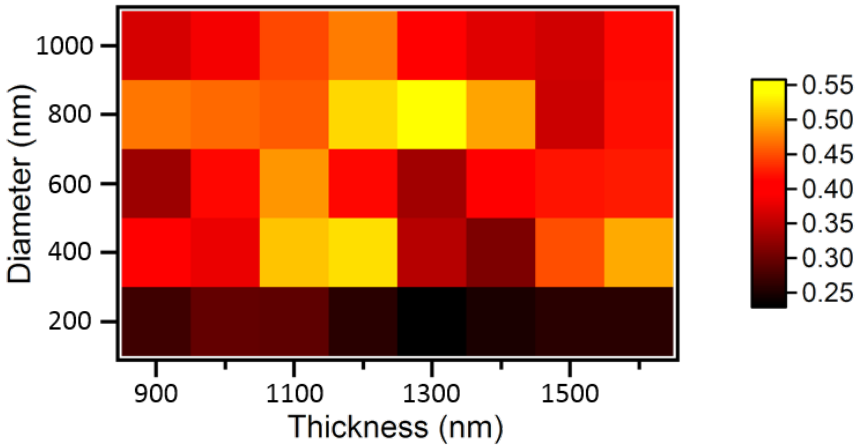

FIGURE 5.19: Collection efficiency calculated at the half angle of 58.8° as a function of diameter and thickness of pillars.

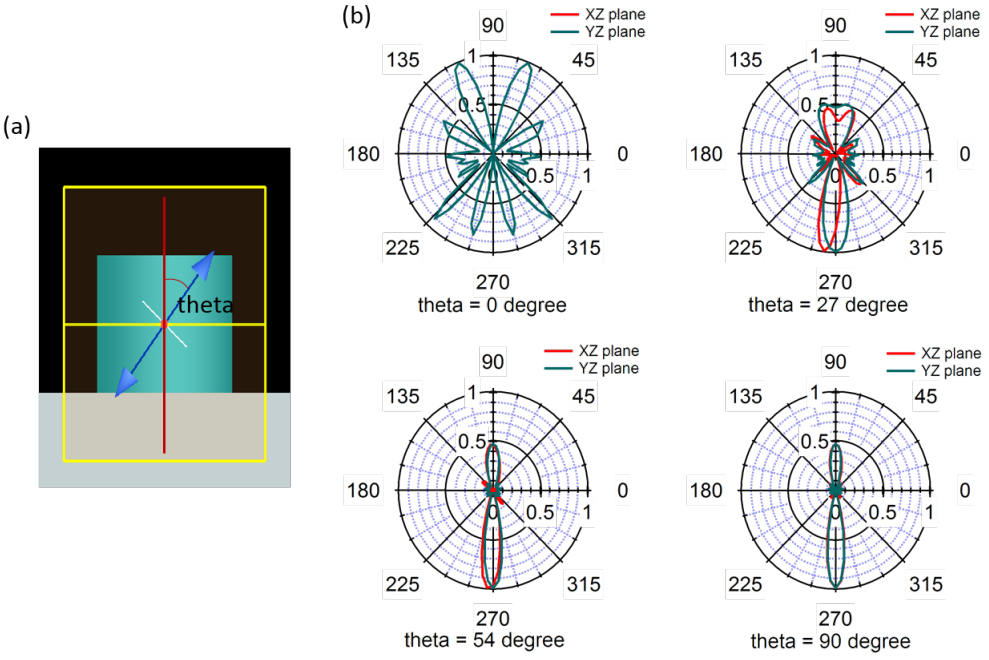

FIGURE 5.20: (a) Simulation model of the coupling of the SH signals out of a pillar cavity. The dipole source emits a single wavelength at 532 nm, $n_{glass} = 1.5$, $n_{SU8} = 1.58$. (b) Radiation patterns of a dipole with different orientation located in a micropillar.

i.e. the electric field intensity distribution in the (xz) and (yz)–planes of a film structure (left) and a pillar structure (right). It can be clearly seen that in the case of the pillar, the emitted light is mostly directed downward and located inside the half angle which represents the collection cone of the microscope objective half

angle= $\arcsin(NA/n) = 58.8°$, where NA is the numerical aperture of the objective lens, n is the refractive index of the immersion oil. Therefore most of the emitted light could be collected and detected. On the contrary, the radiation pattern in the case of the film is distributed in a very large angle, resulting in a loss of signal propagating out of the collection cone of the microscope objective. To be more precise, we evaluate numerically the collection efficiency as a function of the half angle of the objective. Figure 5.18(b) shows the simulation result. It can be seen that, almost 55% of the photons emitted by the dipole embedded inside the pillar can be collected at the half angle of 58.8°, which corresponds to an objective lens NA of 1.3. Meanwhile, only 11% photons is collected at the same angle in the case of film. It can be concluded that, the cavity does not only enhance the fundamental light, which results in the enhancement of the SH signal emitted by the dipole, but also directs the SH signal into the collection angle of the microscope, hence enhancing the collection efficiency. The degree of enhancement of the collection efficiency depends strongly on the size of the pillar. Figure 5.19 presents the calculation of the collection efficiency at the half angle of 58.8° as a function of diameter and thickness of pillars. This pixel map is very useful to predict the best configuration of the pillar for the highest collection efficiency. In this case, the highest collection efficiency belongs to a pillar with a diameter of 800 nm and a thickness of 1300 nm. The simulation can be applied to a larger range of size and any kind of desired structures.

5.4.2.2 Influence of dipole orientation

To study the influence of the emitting dipole orientation on the collection efficiency of the microscope objective, we now consider the parameter θ of the dipole, which is the angle the dipole makes with z-axis (Figure 5.20(a)). This angle is swept from 0° to 90° with a step of 1°. Figure 5.20(b) shows the radiation patterns the dipole with different θ angles located inside a micropillar (diameter = 800 nm, height = 1.3 μm). It can be seen that with small θ, the emitted light is distributed in a large angle, but as θ increases, this angle becomes smaller, which means the collection efficiency increases. We also calculate the collection efficiency as a function of the dipole orientation as shown in Figure 5.21. The best value undoubtedly belongs to the angle $\theta = 90°$, *i.e.*, the dipole orientation is parallel to the sample plane. Therefore, it can be concluded that the dipole orientation also affects greatly the collection efficiency, hence affected

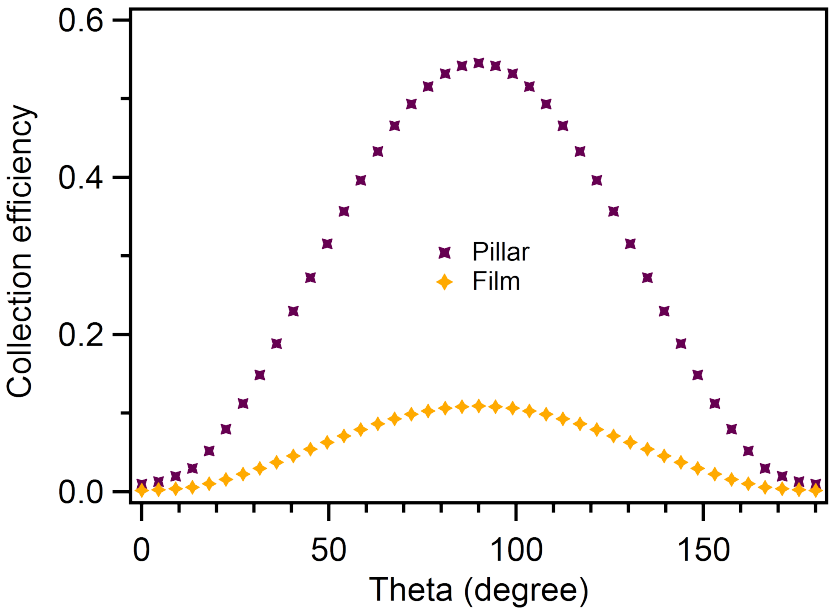

FIGURE 5.21: Collection efficiency calculated at the half angle of 58.8° as a function of the dipole orientation.

the detected SHG signal. In practice, this orientation depends on the orientation of the KTP crystal, which is defined by three angles (θ, ψ, ϕ). These angles can be determined by a method called defocused imaging [168]. However, due to the lack of equipment, we could not carry out the experiments to confirm this simulation.

5.5 Conclusion

In this chapter, we first investigated the SHG of individual nanocrystals of KTP with size ranging from 30 nm to 100 nm. These KTP NPs, under a pulsed laser excitation and off two-photon resonance, efficiently emit a second harmonic signal. The use of KTP, with its high nonlinear coefficients and its transparency for both the wavelength of the excitation laser and the second harmonic signal, leads to a high signal-to-background ratio as well as a perfect photostability. We then employed LOPA DLW to realize PSs containing individual KTP NPs. KTP NPs are found not to cause explosion during fabrication as Au NPs do, hence they are an ideal candidate to be manipulated and coupled to various kinds of PS. We have successfully embedded individual KTP NPs into different kinds of 2D and 3D structures. The

size, shape of the structures, as well as the position of the NPs inside the structures, can be controlled at nanoscale. We found an enhancement up to 90 times of the SHG signal of a KTP NP embedded in a polymeric pillar. The enhancement was different for different NPs, since it is not only due to the resonance of the fundamental light in the cavity, but also due to the orientation of the KTP nanocrystals, which affects the collection efficiency of the OL. A simulation model using FDTD method has been studied and confirmed the experimental results.

Conclusions and Prospects

This thesis has been developed to investigate the coupling of nanoparticles (NPs) and photonic structures (PSs). The first part is devoted to optimize of a simple, low-cost, yet efficient technique called LOPA DLW, and the other parts to employ and develop this technique to fabricate and characterize hybrid polymeric structures containing different kinds of NP. This thesis focuses on the following aspects:

First, we briefly introduced the theory and the fabrication of a simple, low-cost technique called LOPA DLW, which had been demonstrated and developed by our group. This technique allows the fabrication of any desired multidimensional structures. We then investigated the optimization of the LOPA DLW technique to overcome some existing drawbacks. By using LOPA DLW with optically induced thermal effect taken into account, we have succeeded in fabricating small and accumulation-free submicrometer polymeric 2D and 3D structures. Solving the heat equation using finite element model realized by Matlab to explain the optically induced thermal effect, we demonstrated that the heat induced by high excitation intensity of a 532 nm continuous-wave laser confined the crosslinking reaction in the local region where the temperature is higher than the PEB temperature. This resulted in high spatial resolution and uniform structures, since only the material within the cross-linking temperature region was properly polymerized. Temperature-depth dependence calculation showed that this technique enables the fabrication of uniform 3D sub-microstructures with large thickness. This was then evident by an experimental demonstration of fabrication of a uniform 3D woodpile structure without PEB step, with a period as small as 400 nm. Non-uniform shrinkage effect in polymer was also considered and significantly improved by using a method called multi-anchor supporting method. As compared to the commonly used TPA method,

LOPA-based DLW with local PEB shows numerous advantages such as simple, low-cost setup and simplified fabrication process, while producing structures of equal quality.

Second, we used a magnetic/polymeric nanocomposite to demonstrate the fabrication of magneto-photonic submicrostructures on demand by the use of LOPA-based DLW technique. By incorporating superparamagnetic magnetite NPs (Fe_3O_4) into SU8 polymer matrix with various SU8 viscosities, we have found the most appropriate value of viscosity for hosting MNPs to give the uniform distribution of NPs at concentration of about 2% wt without sedimentation. The sample preparation time also plays an important role, allowing a remarkable improvement in MNPs dispersion, resulting in a high quality magnetic nanocomposite. The homogeneous dispersion of MNPs within polymer matrix enables us to fabricate desired magnetic structures at nanoscale. The LOPA-based DLW technique has been employed successfully to realize any arbitrary 2D and 3D submicrostructures. Furthermore, we also demonstrated a prospective application of magneto-photonic devices by fabricating free-moving magnetic microswimmers and by examinating their magnetic response to an external magnetic field. The high magnetic response of these hybrid structures enables controllable movements of the magnetic microswimmers. The LOPA-based DLW technique was also successfully employed to realize desired 3D magneto-photonic crystals and microdevices with complex 3D components. Therefore, the combination of LOPA-based DLW technique with nanocomposite and with the aid of an external magnetic field will allow us to obtain any desired magneto-photonic devices. These results open many promising applications, such as the development of microrobotic tools for transport in biological systems.

Third, we investigated another kind of NP, gold NPs, and used them to study the coupling to PS, not as random NPs like in the previous part, but as single NPs that can be individually localized via their fluorescence. We have demonstrated theoretically and experimentally the precise coupling of a single Au NP into a photonic microstructure using LOPA-based DLW technique. Simulations based on FDTD method have proved the mechanism of the coupling of the excitation wavelength into cavities, the plasmonics/photonics coupling, and the coupling of the emitted light out of cavities, which predict the enhancement of the fluorescence signal of Au NPs. The coupled NP/PS was realized by a LOPA DLW technique, and with a

double-step process: ultralow excitation power for determination of NP position, and low excitation power for the fabrication of desired microstructures. We encountered an unexpected effect due to the heat induced by the SPR of the Au NPs during the fabrication: instead of a micropillar containing a NP, we obtained a microsphere. However, the coupling of NP to the microsphere still allowed a great enhancement of the fluorescence signal as compared to the case without coupling, which is in good agreement with the theoretical prediction. Au NPs with different sizes have been investigated and we obtained the highest gain in fluorescence, up to 36.6 times with a 10-nm gold NP. This LOPA-based DLW with a double-step process has been proved to be a very simple but powerful technique to incorporate individual NPs into PS as compared with other complicated and expensive techniques.

Fourth, in order to avoid the explosion effect during the exposure under laser excitation, we chose to investigate KTP NPs since they possess a wide tranparency range including the used wavelengths. We have studied the coupling of individual KTP NPs and different kinds of structure. First, we investigated optically by second harmonic microscopy individual nanocrystals of KTP with size ranging from 30 nm to 100 nm synthezized by our colleagues. These KTP NPs, under a pulsed laser excitation and without two-photon resonance, efficiently emit a second harmonic signal. The use of KTP, with its high nonlinear coefficients and its transparency for both the wavelength of the excitation laser and the second harmonic signal, leads to a high signal-to-background ratio as well as to a perfect photostability for a very long time of the generated signal. We then employed LOPA DLW to realize the fabrication of PS containing individual KTP NPs. KTP NPs are found not to cause explosion during fabrication, contrary to Au NPs, hence they are ideal candidates to be manipulated and coupled to various kinds of PS. We have successfully embedded individual KTP NPs into different kinds of structure, especially 3D structures. The size and shape of the structures, as well as the position of the NPs inside the structures, can be controlled with high spatial resolution. We found an enhancement up to 90 times of the SHG signal of a KTP NP embedded in a pillar. The enhancement was different for different NPs, since it is not only due to the resonance of the fundamental light in the cavity, but also due to the orientation of the KTP nanocrystals, which affects the collection efficiency of the OL. A simulation model using FDTD method has been studied which confirms the experimental results.

To conclude, we have theoretically and experimentally investigated an optimization method for LOPA DLW, which helps overcome some drawbacks existing in polymeric structures such as accumulation and shrinkage effects. Then employing this LOPA DLW, we have studied three kinds of NPs, each of them possessing featured properties which are enhanced by incorporating them into a PS. These investigations have proved the excellent capability of LOPA DLW, in addition to those demonstrated previously in [45, 47], and also open a new door to many interesting applications based on such hybrid structures.

Outlook

For future work, we emphasize some potential research which can follow this thesis study:

- Local PEB can be investigated under low temperature condition. While the surrounding areas are kept at a constant low temperature and only the area at the focusing spot is heated, it is possible to achieve structures with sizes even smaller than the limit of 100 nm.
- We have successfully fabricated magneto-photonic microstructures using a magnetic nanocomposite with randomly oriented MNPs. It is also possible to study structures made from pre-oriented MNPs by applying an external magnetic field during fabrication. Another possibility is to investigate single MNP to create single domain magnetic structures.
- For KTP NPs, further research on 3D microstructures both theoretically and experimentally is necessary since fundamental light can have higher resonance in 3D cavities which can serve for the great enhancement of SHG signal of KTP NPs.
- Coupling of a single photon source into a 3D cavity into 3D PS is in high demand for quantum device. This is currently investigated by another PhD student in the group.

Appendices

Appendix A

The PSF of high NA OLs

The point spread function (PSF) properties were calculated for an air OL, (NA=0.9) and an oil OL (NA=1.3) based on vectorial Debye approximation [44]. The results are shown in figure A.1.

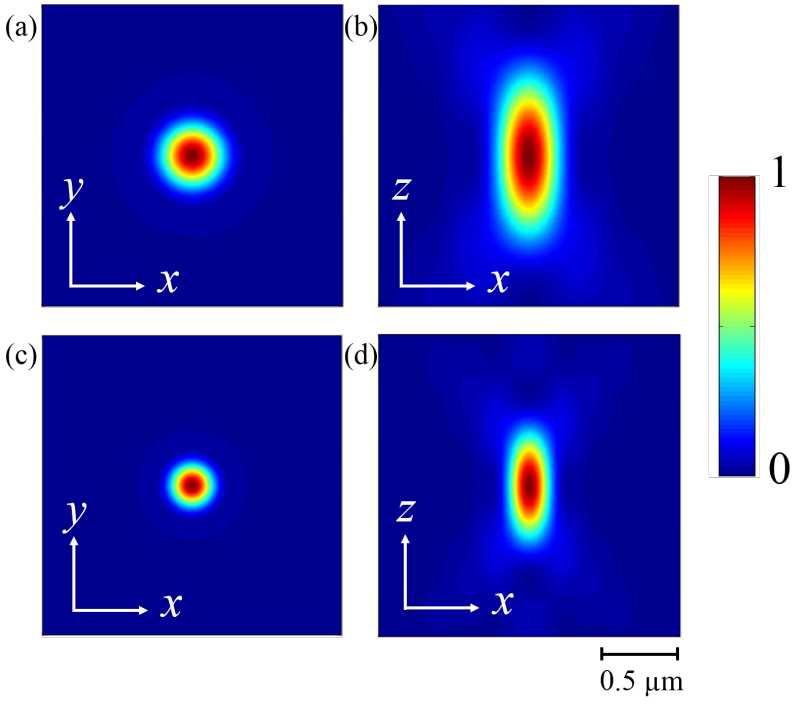

FIGURE A.1: *The intensity distributions in the focusing region of high NA OL. Results are obtained with λ =532 nm. (a,b): OL, NA = 0.9 (air-immersion); (c,d): OL, NA = 1.3 (oil-immersion).*

Appendix B

The calculation of local thermal effect induced by a focused laser beam

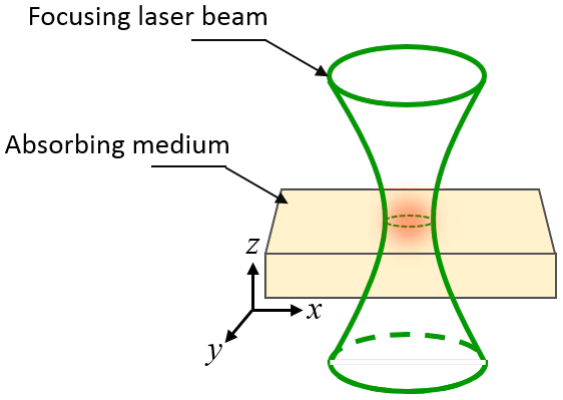

FIGURE B.1: *Simulation model used to calculate the thermal distribution induced by a focused laser beam inside an absorbing medium.*

Matlab example for simulation of heat intensity distribution inside an absorbing medium.

```
function [Zdata] = pdemodel

[pde_fig,ax]=pdeinit;
pdetool('appl_cb',9);
set(ax,'DataAspectRatio',[1 1 1]);
set(ax,'PlotBoxAspectRatio',[832 506.25 15892897959.183657]);
set(ax,'XLimMode','auto');
set(ax,'YLim',[-8.6325953417441067e-08 7.7689467766846696e-08]);
set(ax,'XTickMode','auto');
set(ax,'YTickMode','auto');
pdetool('gridon','on');

% Geometry description:
pderect([-5.0000000000000004e-06 5.0000000000000004e-06 5.0000000000000004e-06
    -5.0000000000000004e-06],'R1');
pdeellip(0,0,1e-08,1e-08,...
0,'E1');
set(findobj(get(pde_fig,'Children'),'Tag','PDEEval'),'String','R1+E1')

% Boundary conditions:pdetool('changemode',0)
pdesetbd(4,...
'dir',...
1,...
'0',...
'20')
pdesetbd(3,...
'dir',...
1,...
'0',...
'20')
pdesetbd(2,...
'dir',...
1,...
'0',...
'20')
pdesetbd(1,...
'dir',...
1,...
'0',...
'20')

% Mesh generation:
setappdata(pde_fig,'Hgrad',1.3);
setappdata(pde_fig,'refinemethod','regular');
setappdata(pde_fig,'jiggle',char('on','mean',''));
setappdata(pde_fig,'MesherVersion','preR2013a');
pdetool('initmesh')
pdetool('refine')
pdetool('refine')

% PDE coefficients:
```

```
pdeseteq(2,...
'k_function(x,y)!k_function(x,y)',...
'0!0',...
'(1e15*heatfunction(x,y))+(0).*(0.0)!(1e15*heatfunction(x,y))+(0).*(0.0)',...
'(1200).*(1200)!(1200).*(1200)',...
'logspace(-2,-1,10)',...
'20',...
'0.0',...
'[0 100]')
setappdata(pde_fig,'currparam',...
['1200!1200                                          ';...
'1200!1200                                         ';...
'k_function(x,y)!k_function(x,y)                   ';...
'1e15*heatfunction(x,y)!1e15*heatfunction(x,y)';...
'0!0                                               ';...
'0.0!0.0                                           '])

% Solve parameters:
setappdata(pde_fig,'solveparam',...
char('0','31056','10','pdeadworst',...
'0.5','longest','0','1E-4','','fixed','Inf'))

% Plotflags and user data strings:
setappdata(pde_fig,'plotflags',[1 1 1 1 1 1 6 1 0 0 0 10 1 0 1 0 0 1]);
setappdata(pde_fig,'colstring','');
setappdata(pde_fig,'arrowstring','');
setappdata(pde_fig,'deformstring','');
setappdata(pde_fig,'heightstring','');

% Solve PDE:
pdetool('solve')

% Change mesh of solutions
[p,e,t,u]=getpetu;
x=linspace(-5e-6,5e-6,10001);y=0;
Zdata = tri2grid(p,t,u(:,10),x,y);

plot(Zdata)
%close all force
```

Appendix C

Optical characteristics of KTP

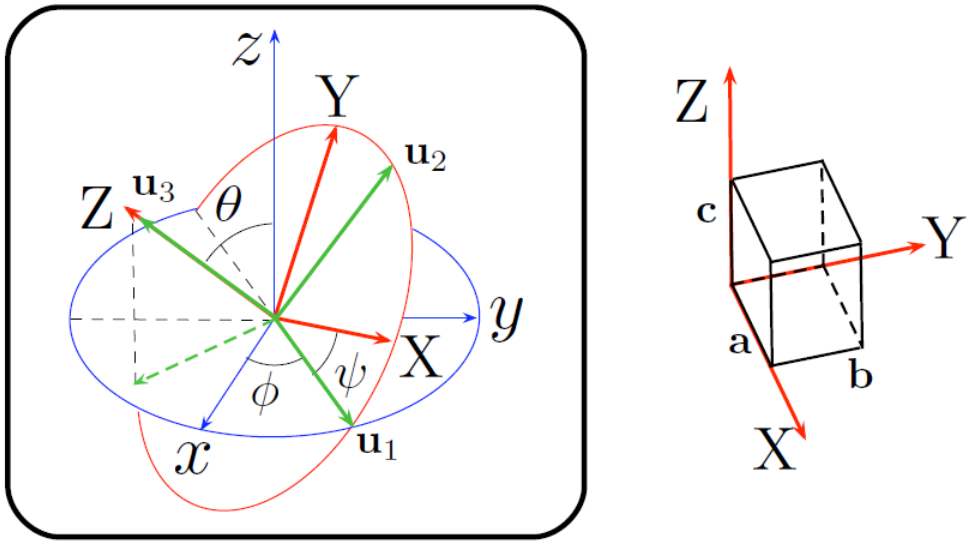

FIGURE C.1: *KTP crystal in its own reference (XYZ) and in the laboratory reference (xyz)*

The crystal of KTP (KTiOPO4) is a nonlinear crystal of point group mm2, with the following mesh parameters [172]:

It is at the same time a piezoelectric crystal and dielectrically biaxed. For this particular crystal, the 3 dielectric axes (x, y, z) merge with its 3 piezoelectric axes

$$\mathbf{a} = 12.814A° \quad \mathbf{b} = 6.404A° \quad \mathbf{c} = 10.616A°$$

$$\begin{array}{llll} n_X = 1.7400 & n_Y = 1.7469 & n_X = 1.8304 & \text{at 1064 nm} \\ n_X = 1.7787 & n_Y = 1.7924 & n_X = 1.8873 & \text{at 532 nm} \end{array}$$

(*X, Y, Z*) and its mesh vectors (a, b, c). We can therefore note (*XYZ*) as the reference linked to the crystal, and we denote (*xyz*) the reference of the laboratory (Figure C.1)

With these notations, the refractive indices of the KTP are given by: And the non-linear polarizability **P** is written in the referential of the crystal:

$$P_I = \sum_{J,K} \chi_{IJK}.E_J E_K, \tag{C.1}$$

with I, J, K replacing X, Y, or Z.

In reference (68), the coefficients are given in the form of a contraction of index: $E_J E_K = E_L^2$, the expression of **P** then becomes

$$P_I = \sum_{L} \chi_{IL}.E_L^2, \tag{C.2}$$

taking as notation $I = 1, 2, 3$ replacing X, Y, Z; $L = 1, 2, 3, 4, 5, 6$ replacing XX, YY, ZZ, YZ = ZY, XZ = ZX, XY = YX, respectively.

The susceptibility of order 2 $d_{IJK}^{(2)} = \frac{1}{2}\chi_{IJK}^{(2)}$ is presented under a matrix form:

$$\begin{bmatrix} d_{11} & d_{12} & d_{13} & d_{14} & d_{15} & d_{16} \\ d_{21} & d_{22} & d_{23} & d_{24} & d_{25} & d_{26} \\ d_{31} & d_{32} & d_{33} & d_{34} & d_{35} & d_{36} \end{bmatrix} = \begin{bmatrix} 0 & 0 & 0 & 0 & d_{15} & 0 \\ 0 & 0 & 0 & d_{24} & 0 & 0 \\ d_{31} & d_{32} & d_{33} & 0 & 0 & 0 \end{bmatrix}$$

with $d_{15} = 1.9$; $d_{24} = 3.6$; $d_{31} = 2.5$; $d_{32} = 4.4$; $d_{33} = 16.9$; and all the other coefficients are null.

These coefficients of d can be expressed in the reference (*XYZ*): $d_{XXZ} = d_{XZX} = 1.9$; $d_{YZY} = d_{YYZ} = 3.6$; $d_{ZXX} = 2.5$; $d_{ZYY} = 4.4$; $d_{ZZZ} = 16.9$; and all the other coefficients are null.

Bibliography

[1] Dupas, C., Houdy, P., and Lahmani, M., eds., [*Nanoscience - Nanotechnologies and nanophysics*], Springer, Berlin (2007).

[2] Sibilia, C., Benson, T. M., Marciniak, M., and Szoplik, T., eds., [*Photonic Crystals: Physics and Technology*], Springer, Milano (2008).

[3] Wong, C. P., ed., [*Polymers for electronic and photonic applications*], Academic Press, Elsevier, Amsterdam (1992).

[4] Charra, F., Agranovich, V. M., Kajzar, F., and North Atlantic Treaty Organization, eds., [*Organic nanophotonics*], vol. 100 of *NATO science series*, Kluwer Academic Publishers, Dordrecht (2003).

[5] Strauf, S., Stoltz, N. G., Rakher, M. T., Coldren, L. A., Petroff, P. M., and Bouwmeester, D., "High-frequency single-photon source with polarization control," *Nature Photonics* **1**, 704–708 (Dec. 2007).

[6] Dumeige, Y., Treussart, F., Alléaume, R., Roch, J.-F., Gacoin, T., and Grangier, P., "Photoinduced creation of nitrogen related colored centers in diamond nanocrystals under femtosecond illumination," *Journal of Luminescence* **109**, 61–67 (2004).

[7] Jelezko, F. and J. Wrachtrup, J., "Single defect centres in diamond: A review," *physica status solidi (a)* **203**, 3207 – 3225 (2006).

[8] Hemmer, P. and Wrachtrup, J., "Where is my quantum computer?," *Science* **324**, 473–474 (Apr. 2009).

[9] Reiss, G. and Hütten, A., "Magnetic nanoparticles: Applications beyond data storage," *Nature Materials* **4**, 725–726 (Oct. 2005).

[10] Chappert, C., Fert, A., and Van Dau, F. N., "The emergence of spin electronics in data storage," *Nature Materials* **6**, 813–823 (Nov. 2007).

[11] Alonso, J., Khurshid, H., Devkota, J., Nemati, Z., Khadka, N.-K., Srikanth, H. Pan, J., and Phan, M.-H., "Superparamagnetic nanoparticles encapsulated in lipid vesicles for advanced magnetic hyperthermia and biodetection," *Journal of Applied Physics* **119**, 083904 (2016).

[12] Lal, S., Clare, S. E., and Halas, N. J., "Nanoshell-Enabled Photothermal Cancer Therapy: Impending Clinical Impact," *Accounts of Chemical Research* **41**, 1842–1851 (Dec. 2008).

[13] Huang, X., Jain, P. K., El-Sayed, I. H., and El-Sayed, M. A., "Plasmonic photothermal therapy (PPTT) using gold nanoparticles," *Lasers in Medical Science* **23**, 217–228 (Aug. 2007).

[14] Clavero, C., "Plasmon-induced hot-electron generation at nanoparticle/metal-oxide interfaces for photovoltaic and photocatalytic devices," *Nature Photonics* **8**, 95–103 (2014).

[15] Davide Staedler, D., Magouroux, T., Hadji, R., Joulaud, C., Extermann, J., Schwung, S., Passemard, S., Kasparian, C., Clarke, G., Gerrmann, M., Dantec, R.-L., Mugnier, Y., Rytz, D., Ciepielewski, D., Galez, C., Gerber-Lemaire, S., Juillerat-Jeanneret, L., Bonacina, L., and Wolf, J.-P., "Harmonic nanocrystals for biolabeling: A survey of optical properties and biocompatibility," *ACS Nano* **6**, 2542—2549 (2012).

[16] Gao, X., Cui, Y., Levenson, R.-M., Chung, L.-W., and Nie, S., "In vivo cancer targeting and imaging with semiconductor quantum dots," *Nature Biotechnology* **22**, 969–976 (2004).

[17] Shukla, S., Furlani, E. P., Vidal, X., Swihart, M. T., and Prasad, P. N., "Two-Photon Lithography of Sub-Wavelength Metallic Structures in a Polymer Matrix," *Advanced Materials* **22**, 3695–3699 (Sept. 2010).

[18] Sun, Z.-B., Dong, X.-Z., Chen, W.-Q., Nakanishi, S., Duan, X.-M., and Kawata, S., "Multicolor Polymer Nanocomposites: In Situ Synthesis and Fabrication of 3D Microstructures," *Advanced Materials* **20**, 914–919 (Mar. 2008).

[19] Gass, J., Poddar, P., Almand, J., Srinath, S., and Srikanth, H., "Superparamagnetic Polymer Nanocomposites with Uniform Fe_3O_4 Nanoparticle Dispersions," *Advanced Functional Materials* **16**, 71–75 (Jan. 2006).

[20] Lu, W., Xie, P., Zhang, Z.-Q., Wong, G.-K.-L., and Wong, K.-S., "Simultaneous perfect phase matching for second and third harmonic generations in zns/yf3 photonic crystal for visible emissions," *Opt. Express* **14**, 12353–12358 (2006).

[21] Galli, M., Gerace, D., Welna, K., Krauss, T. F., O'Faolain, L., Guizzetti, G., and Andreani, L. C., "Low-power continuous-wave generation of visible harmonics in silicon photonic crystal nanocavities," *Optics Express* **18**, 26613 (Dec. 2010).

[22] Noda, S., Fujita, M., and Asano, T., "Spontaneous-emission control by photonic crystals and nanocavities," *Nature Photonics* **1**, 449–458 (Aug. 2007).

[23] Nomura, M., Kumagai, N., Iwamoto, S., Ota, Y., and Arakawa, Y., "Laser oscillation in a strongly coupled single-quantum-dot–nanocavity system," *Nature Physics* **6**, 279–283 (Apr. 2010).

[24] Hu, X., Jiang, P., Ding, C., Yang, H., and Gong, Q., "Picosecond and low-power all-optical switching based on an organic photonic-bandgap microcavity," *Nature Photonics* **2**, 185–189 (Mar. 2008).

[25] Liu, H.-Y., Wang, C.-T., Hsu, C.-Y., Lin, T.-H., and Liu, J.-H., "Optically tuneable blue phase photonic band gaps," *Applied Physics Letters* **96**, 121103 (Mar. 2010).

[26] Barth, M., Schietinger, S., Fischer, S., Becker, J., Nüsse, N., Aichele, T., Löchel, B., Sönnichsen, C., and Benson, O., "Nanoassembled Plasmonic-Photonic Hybrid Cavity for Tailored Light-Matter Coupling," *Nano Letters* **10**, 891–895 (Mar. 2010).

[27] Galli, M., Gerace, D., Welna, K., Krauss, T. F., O'Faolain, L., Guizzetti, G., and Andreani, L. C., "Low-power continuous-wave generation of visible harmonics in silicon photonic crystal nanocavities," *Optics Express* **18**, 26613–26624 (Dec. 2010).

[28] Kataja, M., Hakala, T. K., Julku, A., Huttunen, M. J., van Dijken, S., and Törmä, P., "Surface lattice resonances and magneto-optical response in magnetic nanoparticle arrays," *Nature Communications* **6**, 7072 (May 2015).

[29] Le Xuan, L., Brasselet, S., Treussart, F., Roch, J.-F., Marquier, F., Chauvat, D., Perruchas, S., Tard, C., and Gacoin, T., "Balanced homodyne detection of second-harmonic generation from isolated subwavelength emitters," *Applied Physics Letters* **89**, 121118 (Sept. 2006).

[30] Le Xuan, L., Zhou, C., Slablab, A., Chauvat, D., Tard, C., Perruchas, S., Gacoin, T., Villeval, P., and Roch, J.-F., "Photostable Second-Harmonic Generation from a Single KTiOPO4 Nanocrystal for Nonlinear Microscopy," *Small* **4**, 1332–1336 (Sept. 2008).

[31] Zielinski, M., Oron, D., Chauvat, D., and Zyss, J., "Second-Harmonic Generation from a Single Core/Shell Quantum Dot," *Small* **5**, 2835–2840 (Dec. 2009).

[32] Zielinski, M., Winter, S., Kolkowski, R., Nogues, C., Oron, D., Zyss, J., and Chauvat, D., "Nanoengineering the second order susceptibility in semiconductor quantum dot heterostructures," *Optics Express* **19**, 6657 (Mar. 2011).

[33] Mascheck, M., Schmidt, S., Silies, M., Yatsui, T., Kitamura, K., Ohtsu, M., Leipold, D., Runge, E., and Lienau, C., "Observing the localization of light in space and time by ultrafast second-harmonic microscopy," *Nature Photonics* **6**, 293–298 (May 2012).

[34] Khajavikhan, M., Simic, A., Katz, M., Lee, J. H., Slutsky, B., Mizrahi, A., Lomakin, V., and Fainman, Y., "Thresholdless nanoscale coaxial lasers," *Nature* **482**, 204–207 (Feb. 2012).

[35] Rivoire, K., Lin, Z., Hatami, F., and Vučković, J., "Sum-frequency generation in doubly resonant GaP photonic crystal nanocavities," *Applied Physics Letters* **97**, 043103 (July 2010).

[36] Benisty, H., "Photonic crystals: New designs to confine light," *Nature Physics* **1**, 9–10 (Oct. 2005).

[37] Jelezko, F., Popa, I., Gruber, A., Tietz, C., Wrachtrup, J., Nizovtsev, A., and Kilin, S., "Single spin states in a defect center resolved by optical spectroscopy," *Applied Physics Letters* **81**, 81–83 (2002).

[38] Shi, D., Sadat, M. E., Dunn, A. W., and Mast, D. B., "Photo-fluorescent and magnetic properties of iron oxide nanoparticles for biomedical applications," *Nanoscale* **7**, 8209–8232 (Apr. 2015).

[39] Gimenez, A. J., Ramirez-Wong, D. G., Favela-Camacho, S. E., Sanchez, I. C., Yáñez Limón, J. M., and Luna-Bárcenas, G., "Optical detection of magnetic nanoparticles in colloidal suspensions," *Journal of Magnetism and Magnetic Materials* **402**, 150–155 (Mar. 2016).

[40] Waldherr, G., Beck, J., Neumann, P., Said, R.-S., Nitsche, M., Markham, M.-L., Twitchen, D.-J., Twamley, J., Jelezko, F., and J. Wrachtrup, J., "High-dynamic-range magnetometry with a single nuclear spin in diamond," *Nature Nanotechnology* **7**, 105–108 (2012).

[41] Maletinsky, P., Hong, S., Grinolds, M. S., Hausmann, B., Lukin, M. D., Walsworth, R. L., Loncar, M., and Yacoby, A., "A robust scanning diamond sensor for nanoscale imaging with single nitrogen-vacancy centres," *Nature Nanotech* **7**(5), 320–324 (2012).

[42] Hohmann, J. K., Renner, M., Waller, E. H., and von Freymann, G., "Three-Dimensional μ-Printing: An Enabling Technology," *Advanced Optical Materials* **3**, 1488–1507 (Nov. 2015).

[43] Maruo, S. and Fourkas, J., "Recent progress in multiphoton microfabrication," *Laser & Photonics Reviews* **2**, 100–111 (Apr. 2008).

[44] Li, Q., Do, M. T., Ledoux-Rak, I., and Lai, N. D., "Concept for three-dimensional optical addressing by ultralow one-photon absorption method," *Optics Letters* **38**, 4640 (Nov. 2013).

[45] Do, M. T., Nguyen, T. T. N., Li, Q., Benisty, H., Ledoux-Rak, I., and Lai, N. D., "Submicrometer 3d structures fabrication enabled by one-photon absorption direct laser writing," *Optics Express* **21**, 20964 (Sept. 2013).

[46] Tong, Q. C., Nguyen, D. T. T., Do, M. T., Luong, M. H., Journet, B., Ledoux-Rak, I., and Lai, N. D., "Direct laser writing of polymeric nanostructures via optically induced local thermal effect," *Applied Physics Letters* **108**, 183104 (May 2016).

[47] Tong, Q. C., Luong, M. H., Remmel, J., Do, M. T., Nguyen, D. T. T., and Lai, N. D., "Rapid direct laser writing of desired plasmonic nanostructures," *Optics Letters* **42**, 2382–2385 (June 2017).

[48] Tong, Q. C., Luong, M. H., Tran, T. M., Remmel, J., Do, M. T., Kieu, D. M., Ghasemi, R., Nguyen, D. T., and Lai, N. D., "Realization of Desired Plasmonic Structures via a Direct Laser Writing Technique," *Journal of Electronic Materials* **46**, 3695–3701 (June 2017).

[49] Lin, S. Y., Fleming, J. G., Hetherington, D. L., Smith, B. K., Biswas, R., Ho, K. M., Sigalas, M. M., Zubrzycki, W., Kurtz, S. R., and Bur, J., "A three-dimensional photonic crystal operating at infrared wavelengths," *Nature* **394**, 251–253 (July 1998).

[50] Cumpston, B. H., Ananthavel, S. P., Barlow, S., Dyer, D. L., Ehrlich, J. E., Erskine, L. L., Heikal, A. A., Kuebler, S. M., Lee, I.-Y. S., McCord-Maughon, D., Qin, J., Röckel, H., Rumi, M., Wu, X.-L., Marder, S. R., and Perry, J. W., "Two-photon polymerization initiators for three-dimensional optical data storage and microfabrication," *Nature* **398**, 51–54 (Mar. 1999).

[51] Strickler, J. H. and Webb, W. W., "Three-dimensional optical data storage in refractive media by two-photon point excitation," *Optics Letters* **16**, 1780–1782 (Nov. 1991).

[52] Alkaisi, M., Blaikie, R., McNab, S., Cheung, R., and R. S. Cumming, D., "Sub-diffraction-limited patterning using evanescent near-field optical lithography," *Applied Physics Letters* **75**, 3560–3562 (Nov. 1999).

[53] Mata, A., Fleischman, A. J., and Roy, S., "Fabrication of multi-layer SU-8 microstructures," *Journal of Micromechanics and Microengineering* **16**(2), 276 (2006).

[54] Campbell, M., Sharp, D. N., Harrison, M. T., Denning, R. G., and Turberfield, A. J., "Fabrication of photonic crystals for the visible spectrum by holographic lithography," *Nature* **404**, 53–56 (Mar. 2000).

[55] Lai, N. D., Liang, W. P., Lin, J. H., Hsu, C. C., and Lin, C. H., "Fabrication of two- and three-dimensional periodic structures by multi-exposure of two-beam interference technique," *Optics Express* **13**, 9605–9611 (Nov. 2005).

[56] Lai, N. D., Zheng, T. S., Do, D. B., Lin, J. H., and Hsu, C. C., "Fabrication of desired three-dimensional structures by holographic assembly technique," *Applied Physics A* **100**, 171–175 (July 2010).

[57] Seet, K. K., Mizeikis, V., Juodkazis, S., and Misawa, H., "Three-dimensional horizontal circular spiral photonic crystals with stop gaps below 1 μm," *Applied Physics Letters* **88**, 221101 (May 2006).

[58] Sun, H.-B., Matsuo, S., and Misawa, H., "Three-dimensional photonic crystal structures achieved with two-photon-absorption photopolymerization of resin," *Applied Physics Letters* **74**, 786–788 (Mar. 1999).

[59] Gissibl, T., Thiele, S., Herkommer, A., and Giessen, H., "Two-photon direct laser writing of ultracompact multi-lens objectives," *Nature Photonics* **10**, nphoton.2016.121 (June 2016).

[60] Straub, M. and Gu, M., "Near-infrared photonic crystals with higher-order bandgaps generated by two-photon photopolymerization," *Optics Letters* **27**, 1824–1826 (Oct. 2002).

[61] Rensch, C., Hell, S., Schickfus, M. v., and Hunklinger, S., "Laser scanner for direct writing lithography," *Applied Optics* **28**, 3754–3758 (Sept. 1989).

[62] Bratton, D., Yang, D., Dai, J., and Ober, C. K., "Recent progress in high resolution lithography," *Polymers for Advanced Technologies* **17**, 94–103 (Feb. 2006).

[63] Keller, S., Blagoi, G., Lillemose, M., Haefliger, D., and Boisen, A., "Processing of thin SU-8 films," *Journal of Micromechanics and Microengineering* **18**(12), 125020 (2008).

[64] Do, M. T., Li, Q., Ledoux-Rak, I., and Lai, N. D., "Optimization of LOPA-based direct laser writing technique for fabrication of submicrometric polymer two- and three-dimensional structures," **9127**, 912703, International Society for Optics and Photonics (May 2014).

[65] Seet, K. K., Juodkazis, S., Jarutis, V., and Misawa, H., "Feature-size reduction of photopolymerized structures by femtosecond optical curing of SU-8," *Applied Physics Letters* **89**, 024106 (July 2006).

[66] Yang, S., Matthews, M., Elhadj, S., Cooke, D., M. Guss, G., G. Draggoo, V., and J. Wegner, P., "Comparing the use of mid-infrared versus far-infrared lasers for mitigating damage growth on fused silica," *Applied Optics - APPL OPT* **49** (May 2010).

[67] Wei, J., Wang, Y., and Wu, Y., "Manipulation of heat-diffusion channel in laser thermal lithography," *Optics Express* **22**, 32470–32481 (Dec. 2014).

[68] Kuwahara, M., Mihalcea, C., Atoda, N., Tominaga, J., Fuji, H., and Kikukawa, T., "Thermal lithography for 0.1 μm pattern fabrication," *Microelectronic Engineering* **61–62**, 415–421 (July 2002).

[69] Kuwahara, M., Kim, J. H., and Tominaga, J., "Dot formation with 170-nm dimensions using a thermal lithography technique," *Microelectronic Engineering* **67**, 651–656 (June 2003).

[70] Wei, J., Sun, Z., Zhang, F., Xu, W., Wang, Y., Zhou, F., and Gan, F., "Thermal melting of solid materials induced by ultrafast laser pulse irradiation as explosively homogeneous nucleation," *Chemical Physics Letters* **392**, 415–418 (July 2004).

[71] Jung, B., Sha, J., Paredes, F., Ober, C. K., Thompson, M. O., Chandhok, M., and Younkin, T. R., "Sub-millisecond post exposure bake of chemically amplified resists by CO_2 laser heat treatment," **7639**, 76390L, International Society for Optics and Photonics (Mar. 2010).

[72] Wolf, E., "Electromagnetic diffraction in optical systems - I. An integral representation of the image field," *Proc. R. Soc. Lond. A* **253**, 349–357 (Dec. 1959).

[73] Grupen, M. and Kearfott, K., "Numerical analysis of infrared laser heating in thermoluminescent material layers," *Journal of Applied Physics* **64**, 1044–1049 (Aug. 1988).

[74] Brown, M. S. and Arnold, C. B., "Fundamentals of Laser-Material Interaction and Application to Multiscale Surface Modification," in [*Laser Precision Microfabrication*], Sugioka, K., Meunier, M., and Piqué, A., eds., *Springer Series in Materials Science*(135), 91–120, Springer Berlin Heidelberg (2010). DOI: 10.1007/978-3-642-10523-4_4.

[75] Weiner, A., [*Ultrafast Optics*], John Wiley & Sons (Sept. 2011).

[76] Liu, J., Cai, B., Zhu, J., Ding, G., Zhao, X., Yang, C., and Chen, D., "Process research of high aspect ratio microstructure using SU-8 resist," *Microsystem Technologies* **10**, 265–268 (May 2004).

[77] Matta, J. A. and Outwater, J. O., "The nature, origin and effects of internal stresses in reinforced plastic laminates," *Polymer Engineering & Science* **2**, 314–319 (Oct. 1962).

[78] Scott, T. F., Kloxin, C. J., Forman, D. L., McLeod, R. R., and Bowman, C. N., "Principles of voxel refinement in optical direct write lithography," *Journal of Materials Chemistry* **21**, 14150–14155 (Sept. 2011).

[79] Chen, K.-S., Lin, I.-K., and Ko, F.-H., "Fabrication of 3d polymer microstructures using electron beam lithography and nanoimprinting technologies," *Journal of Micromechanics and Microengineering* **15**(10), 1894 (2005).

[80] Correa, D. S., Boni, L. D., Otuka, A. J. G., Tribuzi, V., and Mendonça, C. R., "Two-Photon Polymerization Fabrication of Doped Microstructures," (2012).

[81] Li, L., Gattass, R. R., Gershgoren, E., Hwang, H., and Fourkas, J. T., "Achieving lambda/20 resolution by one-color initiation and deactivation of polymerization," *Science (New York, N.Y.)* **324**, 910–913 (May 2009).

[82] Ovsianikov, A., Shizhou, X., Farsari, M., Vamvakaki, M., Fotakis, C., and Chichkov, B. N., "Shrinkage of microstructures produced by two-photon polymerization of Zr-based hybrid photosensitive materials," *Optics Express* **17**, 2143–2148 (Feb. 2009).

[83] Sun, Q., Ueno, K., and Misawa, H., "In situ investigation of the shrinkage of photopolymerized micro/nanostructures: the effect of the drying process," *Optics Letters* **37**, 710–712 (Feb. 2012).

[84] Sun, H.-B., Suwa, T., Takada, K., Zaccaria, R. P., Kim, M.-S., Lee, K.-S., and Kawata, S., "Shape precompensation in two-photon laser nanowriting of photonic lattices," *Applied Physics Letters* **85**, 3708–3710 (Oct. 2004).

[85] Maruo, S., Hasegawa, T., and Yoshimura, N., "Single-anchor support and supercritical CO2 drying enable high-precision microfabrication of three-dimensional structures," *Optics Express* **17**, 20945–20951 (Nov. 2009).

[86] Lim, T. W., Son, Y., Yang, D.-Y., Pham, T. A., Kim, D.-P., Yang, B.-I., Lee, K.-S., and Park, S. H., "Net Shape Manufacturing of Three-Dimensional SiCN Ceramic Microstructures Using an Isotropic Shrinkage Method by Introducing Shrinkage Guiders," *International Journal of Applied Ceramic Technology* **5**, 258–264 (May 2008).

[87] Sun, Q., Juodkazis, S., Murazawa, N., Mizeikis, V., and Misawa, H., "Free-standing and movable photonic microstructures fabricated by photopolymerization with femtosecond laser pulses," *Journal of Micromechanics and Microengineering* **20**(3), 035004 (2010).

[88] Fleischmann, M., Hendra, P. J., and McQuillan, A. J., "Raman spectra of pyridine adsorbed at a silver electrode," *Chemical Physics Letters* **26**, 163–166 (May 1974).

[89] Schatz, G. C. and Van Duyne, R. P., "Electromagnetic Mechanism of Surface-Enhanced Spectroscopy," in [*Handbook of Vibrational Spectroscopy*], John Wiley & Sons, Ltd (2006). DOI: 10.1002/0470027320.s0601.

[90] Carmon, T., Rokhsari, H., Yang, L., Kippenberg, T. J., and Vahala, K. J., "Temporal Behavior of Radiation-Pressure-Induced Vibrations of an Optical Microcavity Phonon Mode," *Physical Review Letters* **94**, 223902 (June 2005).

[91] Kippenberg, T. J., Rokhsari, H., Carmon, T., Scherer, A., and Vahala, K. J., "Analysis of Radiation-Pressure Induced Mechanical Oscillation of an Optical Microcavity," *Physical Review Letters* **95**, 033901 (July 2005).

[92] Henderson, J., Shi, S., Cakmaktepe, S., and Crawford, T. M., "Pattern transfer nanomanufacturing using magnetic recording for programmed nanoparticle assembly," *Nanotechnology* **23**(18), 185304 (2012).

[93] Alfadhel, A., Li, B., and Kosel, J., "Magnetic polymer nanocomposites for sensing applications," in [*IEEE SENSORS 2014 Proceedings*], 2066–2069 (Nov. 2014).

[94] Kim, J., Chung, S. E., Choi, S.-E., Lee, H., Kim, J., and Kwon, S., "Programming magnetic anisotropy in polymeric microactuators," *Nature Materials* **10**, 747–752 (Oct. 2011).

[95] Safarik, I. and Safarikova, M., "Magnetic techniques for the isolation and purification of proteins and peptides," *Biomagnetic Research and Technology* **2**, 7 (Nov. 2004).

[96] Seethapathy, S., Górecki, T., and Li, X., "Passive sampling in environmental analysis," *Journal of Chromatography. A* **1184**, 234–253 (Mar. 2008).

[97] Melin, J. and Quake, S. R., "Microfluidic large-scale integration: the evolution of design rules for biological automation," *Annual Review of Biophysics and Biomolecular Structure* **36**, 213–231 (2007).

[98] Jager, E. W. H., Smela, E., and Inganäs, O., "Microfabricating Conjugated Polymer Actuators," *Science* **290**, 1540–1545 (Nov. 2000).

[99] Huang, H.-W., Sakar, M. S., Petruska, A. J., Pané, S., and Nelson, B. J., "Soft micromachines with programmable motility and morphology," *Nature Communications* **7**, ncomms12263 (July 2016).

[100] Sukhoivanov, I. A. and Guryev, I. V., "Introduction to Photonic Crystals," in [*Photonic Crystals*], *Springer Series in Optical Sciences*, 1–12, Springer, Berlin, Heidelberg (2009).

[101] Kharboutly, M., Gauthier, M., and Chaillet, N., "Modeling the trajectory of a microparticle in a dielectrophoresis device," *Journal of Applied Physics* **106**, 114312 (Dec. 2009).

[102] Kosa, G., Shoham, M., and Zaaroor, M., "Propulsion Method for Swimming Microrobots," *IEEE Transactions on Robotics* **23**, 137–150 (Feb. 2007).

[103] Liew, L. A., Bright, V. M., Dunn, M. L., Daily, J. W., and Raj, R., "Development of SiCN ceramic thermal actuators," in [*Technical Digest. MEMS 2002 IEEE International Conference. Fifteenth IEEE International Conference on Micro Electro Mechanical Systems (Cat. No.02CH37266)*], 590–593 (Jan. 2002).

[104] Sun, H.-B., Takada, K., and Kawata, S., "Elastic force analysis of functional polymer submicron oscillators," *Applied Physics Letters* **79**, 3173–3175 (Oct. 2001).

[105] Sun, J. Z., Gaidis, M. C., O'Sullivan, E. J., Joseph, E. A., Hu, G., Abraham, D. W., Nowak, J. J., Trouilloud, P. L., Lu, Y., Brown, S. L., Worledge, D. C., and Gallagher, W. J., "A three-terminal spin-torque-driven magnetic switch," *Applied Physics Letters* **95**, 083506 (Aug. 2009).

[106] Li, J., Sattayasamitsathit, S., Dong, R., Gao, W., Tam, R., Feng, X., Ai, S., and Wang, J., "Template electrosynthesis of tailored-made helical nanoswimmers," *Nanoscale* **6**, 9415–9420 (July 2014).

[107] Gao, W., Feng, X., Pei, A., Kane, C. R., Tam, R., Hennessy, C., and Wang, J., "Bioinspired Helical Microswimmers Based on Vascular Plants," *Nano Letters* **14**, 305–310 (Jan. 2014).

[108] Zhang, L., Abbott, J. J., Dong, L., Kratochvil, B. E., Bell, D., and Nelson, B. J., "Artificial bacterial flagella: Fabrication and magnetic control," *Applied Physics Letters* **94**, 064107 (Feb. 2009).

[109] Ghosh, A. and Fischer, P., "Controlled Propulsion of Artificial Magnetic Nanostructured Propellers," *Nano Letters* **9**, 2243–2245 (June 2009).

[110] Tottori, S., Zhang, L., Qiu, F., Krawczyk, K. K., Franco-Obregón, A., and Nelson, B. J., "Magnetic Helical Micromachines: Fabrication, Controlled Swimming, and Cargo Transport," *Advanced Materials* **24**, 811–816 (Feb. 2012).

[111] Wang, J., Xia, H., Xu, B.-B., Niu, L.-G., Wu, D., Chen, Q.-D., and Sun, H.-B., "Remote manipulation of micronanomachines containing magnetic nanoparticles," *Optics Letters* **34**, 581–583 (Mar. 2009).

[112] Xia, H., Wang, J., Tian, Y., Chen, Q.-D., Du, X.-B., Zhang, Y.-L., He, Y., and Sun, H.-B., "Ferrofluids for Fabrication of Remotely Controllable Micro-Nanomachines by Two-Photon Polymerization," *Advanced Materials* **22**, 3204–3207 (Aug. 2010).

[113] Cui, Z., Rothman, J., Klaui, M., Lopez-Diaz, L., Vaz, C. A. F., and Bland, J. A. C., "Fabrication of magnetic rings for high density memory devices," *Microelectronic Engineering* **61–62**, 577–583 (July 2002).

[114] Terris, B. D. and Thomson, T., "Nanofabricated and self-assembled magnetic structures as data storage media," *Journal of Physics D: Applied Physics* **38**(12), R199 (2005).

[115] Suter, M., Ergeneman, O., Zürcher, J., Moitzi, C., Pané, S., Rudin, T., Pratsinis, S. E., Nelson, B. J., and Hierold, C., "A photopatternable superparamagnetic nanocomposite: Material characterization and fabrication of microstructures," *Sensors and Actuators B: Chemical* **156**, 433–443 (Aug. 2011).

[116] Lu, A.-H., Salabas, E. L., and Schüth, F., "Magnetic Nanoparticles: Synthesis, Protection, Functionalization, and Application," *Angewandte Chemie International Edition* **46**, 1222–1244 (Feb. 2007).

[117] Hyeon, T., "Chemical synthesis of magnetic nanoparticles," *Chem. Commun.* , 927–934 (Apr. 2003).

[118] Hai, N. H., Phu, N. D., Luong, N. H., Chau, N., Chinh, H. D., Hoang, L. H., and Leslie-Pelecky, D. L., "Mechanism for Sustainable Magnetic Nanoparticles under Ambient Conditions," *Journal of Korean Physical Society* **52**, 1327 (May 2008).

[119] Phenrat, T., Kim, H.-J., Fagerlund, F., Illangasekare, T., Tilton, R. D., and Lowry, G. V., "Particle Size Distribution, Concentration, and Magnetic Attraction Affect Transport of Polymer-Modified Fe0 Nanoparticles in Sand Columns," *Environmental Science & Technology* **43**, 5079–5085 (July 2009).

[120] Deatsch, A. E. and Evans, B. A., "Heating efficiency in magnetic nanoparticle hyperthermia," *Journal of Magnetism and Magnetic Materials* **354**, 163–172 (Mar. 2014).

[121] Mahmoudi, K. and Hadjipanayis, C. G., "The application of magnetic nanoparticles for the treatment of brain tumors," *Front. Chem.* **2**, 109 (Dec. 2014).

[122] Mody, V. V., Cox, A., Shah, S., Singh, A., Bevins, W., and Parihar, H., "Magnetic nanoparticle drug delivery systems for targeting tumor," *Appl Nanosci* **4**, 385–392 (Apr. 2013).

[123] Lu, A.-H., Schmidt, W., Matoussevitch, N., Bönnemann, H., Spliethoff, B., Tesche, B., Bill, E., Kiefer, W., and Schüth, F., "Nanoengineering of a Magnetically Separable Hydrogenation Catalyst," *Angewandte Chemie International Edition* **43**, 4303–4306 (Aug. 2004).

[124] Markides, H., Rotherham, M., and El Haj, A. J., "Biocompatibility and Toxicity of Magnetic Nanoparticles in Regenerative Medicine," (2012). DOI: 10.1155/2012/614094.

[125] Troisi, C. S., Knaflitz, M., Olivetti, E. S., Martino, L., and Durin, G., "Fabrication of new Magnetic Micro-Machines for minimally invasive surgery," in [*2008 30th Annual International Conference of the IEEE Engineering in Medicine and Biology Society*], 735–738 (Aug. 2008).

[126] Tian, Y. and Shao, X., "A Laser Fabrication of Magnetic Micromachines by Using Optimized Photosensitive Ferrofluids," *Journal of Nanomaterials* **2016** (2016).

[127] Scholl, J.-A., Koh, A.-L., and Dionne, J.-A., "Quantum plasmon resonances of individual metallic nanoparticles," *Nature* **483**, 421–427 (2012).

[128] Goncalves, M.-R., "Plasmonic nanoparticles: fabrication, simulation and experiments," *Journal Physics D: Applied Physics* **47**, 213001 (2014).

[129] Alonso-Gonzalez, P., Albella, P., Mchnell, M., Chen, J., Huth, F., Garcia-Etxarri, A., Casanova, F., Golmar, F., Arzubiaga, L., Hueso, L.-E., Aizpurua,

J., and Hillenbrand, R., "Resolving the electromagnetic mechanism of surface-enhanced light scattering at single hot spots," *Nature Communication* **3**, 684 (2012).

[130] Chen, Y.-S., Hong, M.-Y., and Huang, G.-S., "A protein transistor made of an antibody molecule and two gold nanoparticles," *Nature Nanotechnology 7, 197–203 (2012)* **7**, 197–203 (2012).

[131] Kühn, S., Håkanson, U., Rogobete, L., and Sandoghdar, V., "Enhancement of Single-Molecule Fluorescence Using a Gold Nanoparticle as an Optical Nanoantenna," *Physical Review Letters* **97**, 017402 (July 2006).

[132] Kim, S., Jin, J., Kim, Y.-J., Park, I.-Y., Kim, Y., and Kim, S.-W., "High-harmonic generation by resonant plasmon field enhancement," *Nature* **453**, 757–760 (June 2008).

[133] Zijlstra, P., Chon, J. W. M., and Gu, M., "Five-dimensional optical recording mediated by surface plasmons in gold nanorods," *Nature* **459**, 410–413 (May 2009).

[134] Schuller, J. A., Barnard, E. S., Cai, W., Jun, Y. C., White, J. S., and Brongersma, M. L., "Plasmonics for extreme light concentration and manipulation," *Nature Materials* **9**, 193–204 (Mar. 2010).

[135] Linic, S., Christopher, P., and Ingram, D. B., "Plasmonic-metal nanostructures for efficient conversion of solar to chemical energy," *Nature Materials* **10**, 911–921 (Dec. 2011).

[136] Zhang, W., Huang, L., Santschi, C., and Martin, O. J. F., "Trapping and Sensing 10 nm Metal Nanoparticles Using Plasmonic Dipole Antennas," *Nano Letters* **10**, 1006–1011 (Mar. 2010).

[137] Koller, D. M., Hohenau, A., Ditlbacher, H., Galler, N., Reil, F., Aussenegg, F. R., Leitner, A., List, E. J. W., and Krenn, J. R., "Organic plasmon-emitting diode," *Nature Photonics* **2**, 684–687 (Nov. 2008).

[138] Englund, D., Fushman, I., and Vučković, J., "General recipe for designing photonic crystal cavities," *Optics Express* **13**(16), 5961 (2005).

[139] Jiménez-Solano, A., López-López, C., Sánchez-Sobrado, O., Luque, J. M., Calvo, M. E., Fernández-López, C., Sánchez-Iglesias, A., Liz-Marzán, L. M., and Míguez, H., "Integration of Gold Nanoparticles in Optical Resonators," *Langmuir* **28**, 9161–9167 (June 2012).

[140] Wang, X. and Palpant, B., "Large and Ultrafast Optical Response of a One-Dimensional Plasmonic–Photonic Cavity," *Plasmonics* **8**, 1647–1653 (June 2013).

[141] Wang, X., Morea, R., Gonzalo, J., and Palpant, B., "Coupling Localized Plasmonic and Photonic Modes Tailors and Boosts Ultrafast Light Modulation by Gold Nanoparticles," *Nano Letters* **15**, 2633–2639 (Apr. 2015).

[142] Huang, C., Bouhelier, A., Colas des Francs, G., Bruyant, A., Guenot, A., Finot, E., Weeber, J.-C., and Dereux, A., "Gain, detuning, and radiation patterns of nanoparticle optical antennas," *Physical Review B* **78**, 155407 (Oct. 2008).

[143] Lukosz, W. and Kunz, R. E., "Light emission by magnetic and electric dipoles close to a plane interface I Total radiated power," *Journal of the Optical Society of America* **67**, 1607 (Dec. 1977).

[144] Do, M. T., Nguyen, D. T. T., Ngo, H. M., Ledoux-Rak, I., and Lai, N. D., "Controlled coupling of a single nanoparticle in polymeric microstructure by low one-photon absorption—based direct laser writing technique," *Nanotechnology* **26**(10), 105301 (2015).

[145] Merabia, S., Shenogin, S., Joly, L., Keblinski, P., and Barrat, J.-L., "Heat transfer from nanoparticles: A corresponding state analysis," *Proceedings of the National Academy of Sciences* **106**, 15113–15118 (Sept. 2009).

[146] Hashimoto, S., Werner, D., and Uwada, T., "Studies on the interaction of pulsed lasers with plasmonic gold nanoparticles toward light manipulation, heat management, and nanofabrication," *Journal of Photochemistry and Photobiology C: Photochemistry Reviews* **13**, 28–54 (Mar. 2012).

[147] Mack, C., "Conventional Resists: Exposure and Bake Chemistry," in [*Fundamental Principles of Optical Lithography*], 191–222, John Wiley & Sons, Ltd (2007). DOI: 10.1002/9780470723876.ch5.

[148] Dousse, A., Suffczyński, J., Braive, R., Miard, A., Lemaître, A., Sagnes, I., Lanco, L., Bloch, J., Voisin, P., and Senellart, P., "Scalable implementation of strongly coupled cavity-quantum dot devices," *Applied Physics Letters* **94**, 121102 (Mar. 2009).

[149] Schell, A. W., Kaschke, J., Fischer, J., Henze, R., Wolters, J., Wegener, M., and Benson, O., "Three-dimensional quantum photonic elements based on single nitrogen vacancy-centres in laser-written microstructures," *Scientific Reports* **3**, 1577 (2013).

[150] Staedler, D., Magouroux, T., Hadji, R., Joulaud, C., Extermann, J., Schwung, S., Passemard, S., Kasparian, C., Clarke, G., Gerrmann, M., Le Dantec, R., Mugnier, Y., Rytz, D., Ciepielewski, D., Galez, C., Gerber-Lemaire, S., Juillerat-Jeanneret, L., Bonacina, L., and Wolf, J.-P., "Harmonic Nanocrystals for Biolabeling: A Survey of Optical Properties and Biocompatibility," *ACS Nano* **6**, 2542–2549 (Mar. 2012).

[151] Kachynski, A. V., Kuzmin, A. N., Nyk, M., Roy, I., and Prasad, P. N., "Zinc Oxide Nanocrystals for Nonresonant Nonlinear Optical Microscopy in Biology and Medicine," *The Journal of Physical Chemistry C* **112**, 10721–10724 (July 2008).

[152] Extermann, J., Bonacina, L., Cuña, E., Kasparian, C., Mugnier, Y., Feurer, T., and Wolf, J.-P., "Nanodoublers as deep imaging markers for multi-photon microscopy," *Optics Express* **17**, 15342–15349 (Aug. 2009).

[153] Grange, R., Lanvin, T., Hsieh, C.-L., Pu, Y., and Psaltis, D., "Imaging with second-harmonic radiation probes in living tissue," *Biomedical Optics Express* **2**, 2532–2539 (Sept. 2011).

[154] Johnson, J. C., Yan, H., Schaller, R. D., Petersen, P. B., Yang, P., and Saykally, R. J., "Near-Field Imaging of Nonlinear Optical Mixing in Single Zinc Oxide Nanowires," *Nano Letters* **2**, 279–283 (Apr. 2002).

[155] Long, J. P., Simpkins, B. S., Rowenhorst, D. J., and Pehrsson, P. E., "Far-field Imaging of Optical Second-Harmonic Generation in Single GaN Nanowires," *Nano Letters* **7**, 831–836 (Mar. 2007).

[156] Bonacina, L., Mugnier, Y., Courvoisier, F., Dantec, R. L., Extermann, J., Lambert, Y., Boutou, V., Galez, C., and Wolf, J.-P., "Polar Fe(IO3)3 nanocrystals as local probes for nonlinear microscopy," *Applied Physics B* **87**, 399–403 (May 2007).

[157] Nakayama, Y., Pauzauskie, P. J., Radenovic, A., Onorato, R. M., Saykally, R. J., Liphardt, J., and Yang, P., "Tunable nanowire nonlinear optical probe," *Nature* **447**, 1098–1101 (June 2007).

[158] Treussart, F., Botzung-Appert, E., Ha-Duong, N.-T., Ibanez, A., Roch, J.-F., and Pansu, R., "Second Harmonic Generation and Fluorescence of CMONS Dye Nanocrystals Grown in a Sol-Gel Thin Film," *ChemPhysChem* **4**, 757–760 (July 2003).

[159] Floc'H, V. L., *Caractérisation de l'organisation moléculaire par microscopie non-linéaire cohérente et incohérente*, phdthesis, École normale supérieure de Cachan - ENS Cachan (May 2004).

[160] Ibanez, A., Maximov, S., Guiu, A., Chaillout, C., and Baldeck, P. L., "Controlled Nanocrystallization of Organic Molecules in Sol-Gel Glasses," *Advanced Materials* **10**, 1540–1543 (Dec. 1998).

[161] Sanz, N., Baldeck, P. L., Nicoud, J.-F., Le Fur, Y., and Ibanez, A., "Polymorphism and luminescence properties of CMONS organic crystals: bulk crystals and nanocrystals confined in gel-glasses," *Solid State Sciences* **3**, 867–875 (Dec. 2001).

[162] Delahaye, E., Tancrez, N., Yi, T., Ledoux, I., Zyss, J., Brasselet, S., and Clément, R., "Second harmonic generation from individual hybrid MnPS3-based nanoparticles investigated by nonlinear microscopy," *Chemical Physics Letters* **429**, 533–537 (Oct. 2006).

[163] Brasselet, S., Le Floc'h, V., Treussart, F., Roch, J.-F., Zyss, J., Botzung-Appert, E., and Ibanez, A., "In situ diagnostics of the crystalline nature of single organic nanocrystals by nonlinear microscopy," *Physical Review Letters* **92**, 207401 (May 2004).

[164] Le Floc'h, V., Brasselet, S., Roch, J.-F., and Zyss, J., "Monitoring of Orientation in Molecular Ensembles by Polarization Sensitive Nonlinear Microscopy," *The Journal of Physical Chemistry B* **107**, 12403–12410 (Nov. 2003).

[165] Renn, A., Seelig, J., and Sandoghdar, V., "Oxygen-dependent photochemistry of fluorescent dyes studied at the single molecule level," *Molecular Physics* **104**, 409–414 (Feb. 2006).

[166] Westphal, V. and Hell, S. W., "Nanoscale resolution in the focal plane of an optical microscope," *Physical Review Letters* **94**, 143903 (Apr. 2005).

[167] Driscoll, T. A., Hoffman, H. J., Stone, R. E., and Perkins, P. E., "Efficient second-harmonic generation in KTP crystals," *JOSA B* **3**, 683–686 (May 1986).

[168] Xuan, L. L., *Génération de seconde harmonique à l'échelle nanométrique : nanocristaux de KTP, exaltation par un réseau métallique*, phdthesis, École normale supérieure de Cachan - ENS Cachan (June 2009).

[169] Sutherland, R. L., [*Handbook of Nonlinear Optics*], CRC Press (Apr. 2003). Google-Books-ID: ccXo3WrHp2UC.

[170] Hansson, G., Karlsson, H., Wang, S., and Laurell, F., "Transmission measurements in KTP and isomorphic compounds," *Applied Optics* **39**, 5058–5069 (Sept. 2000).

[171] Patterson, G. H. and Piston, D. W., "Photobleaching in two-photon excitation microscopy," *Biophysical Journal* **78**, 2159–2162 (Apr. 2000).

[172] Tang, A. M., [*Fundamentals of Optical Parametric Processes and Oscillations*], CRC Press (Mar. 1996). Google-Books-ID: 6FJvbjklAroC.

université PARIS-SACLAY

ÉCOLE DOCTORALE
Physique et ingénierie : électrons, photons, sciences du vivant (EOBE)

Résumé

Titre : Etudes théorique et expérimentale du couplage des nanoparticules uniques dans des structures photoniques à base de polymère

Mots clés : Ecriture directe par laser, Polymère, Structure photonique, Nanoparticule, Microfabrication

Ce travail a été développé pour étudier le couplage entre des nanoparticules (NPs) et des structures photoniques (PSs).

En premier lieu, nous avons présenté brièvement la théorie d'une technique simple et peu coûteuse appelée LOPA DLW qui avait été démontrée et développée par notre groupe. Cette technique permet la fabrication de toutes les structures multidimensionnelles souhaitées. Nous avons ensuite étudié l'optimisation de la technique LOPA DLW pour surmonter certains inconvénients existants. En utilisant LOPA DLW avec un effet thermique induit optiquement, nous avons réussi à fabriquer des petites structures 2D et 3D polymériques submicrométriques, comme montré la Figure 1(a-d). Nous avons démontré que la chaleur induite par une forte intensité d'excitation d'un laser continue à la longeur d'onde de 532 nm permet de finaliser la procès de polymérisation dans la région où la température est plus élevée que la température PEB (Figure 1(e)). Cela a conduit à des structures fines et uniformes, puisque seul le matériau dans la région de température élevée a été correctement polymérisé. Le calcul de la dépendance température-profondeur a montré que cette technique permet la fabrication de microstructures 3D uniformes de grande épaisseur. Cela a ensuite été mis en évidence par une démonstration expérimentale de la fabrication d'une structure en bois 3D uniforme sans étape de PEB standard, avec une période aussi petite que 400 nm. Effet de rétrécissement non uniforme dans le polymère a également été considéré et considérablement

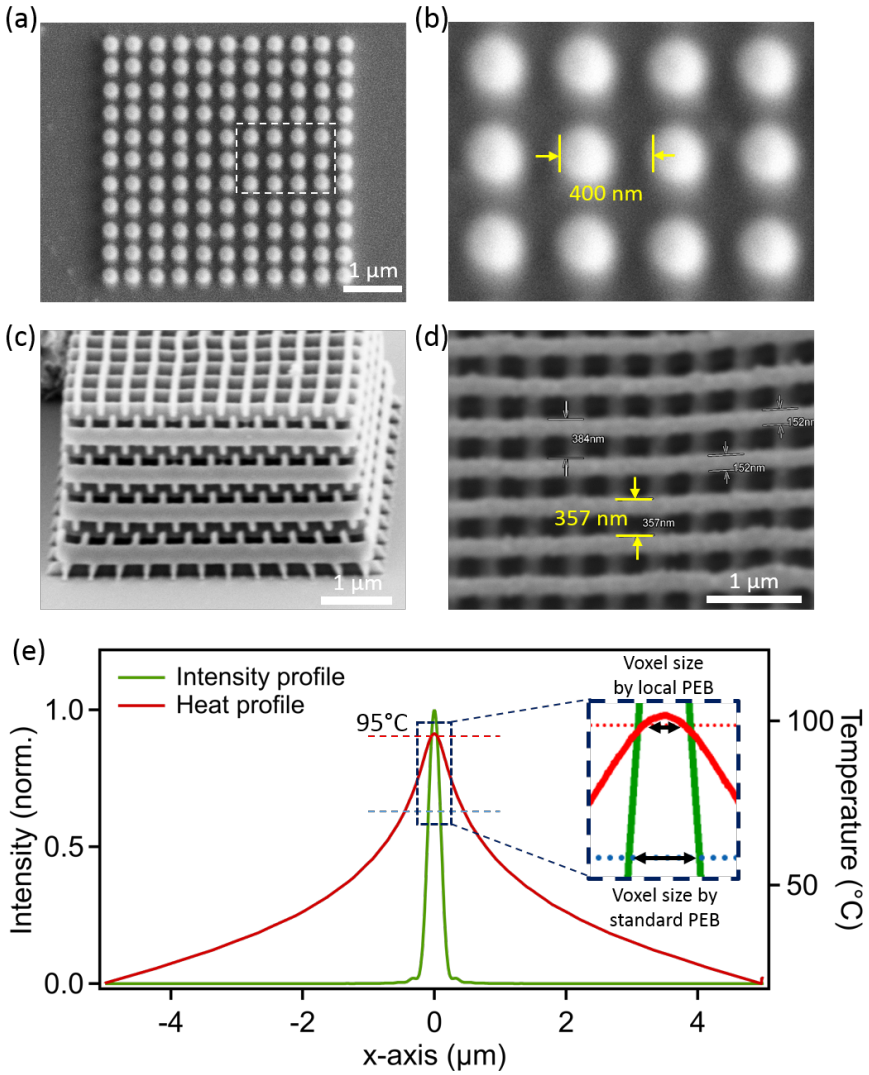

Figure 1: *Structures 2D et 3D fabriquées par DLW à base de LOPA avec PEB local. (a-b) Images MEB d'une structure fabriquée à la puissance laser de 6 mW, vitesse d'écriture = 2 µm/s, période = 400 nm. (c-d) Images au MEB d'une structure en tas de bois fabriquée avec les paramètres suivants: distance entre les barres = 400 nm; distance entre couches = 0,6 µm; nombre de couches = 18; puissance laser P = 7 mW et vitesse de balayage v = 2 µm/s. (e) Coupe transversale du profil de chaleur et de la distribution d'intensité lumineuse dans la région focale pour x -axis.*

amélioré en utilisant une méthode appelée méthode de support multi-ancrage. Comparé à la méthode TPA couramment utilisée, DLW à base de LOPA avec PEB local présente de nombreux avantages tels qu'une configuration simple et peu coûteuse et un processus

de fabrication simplifié, tout en produisant la même qualité de structures.

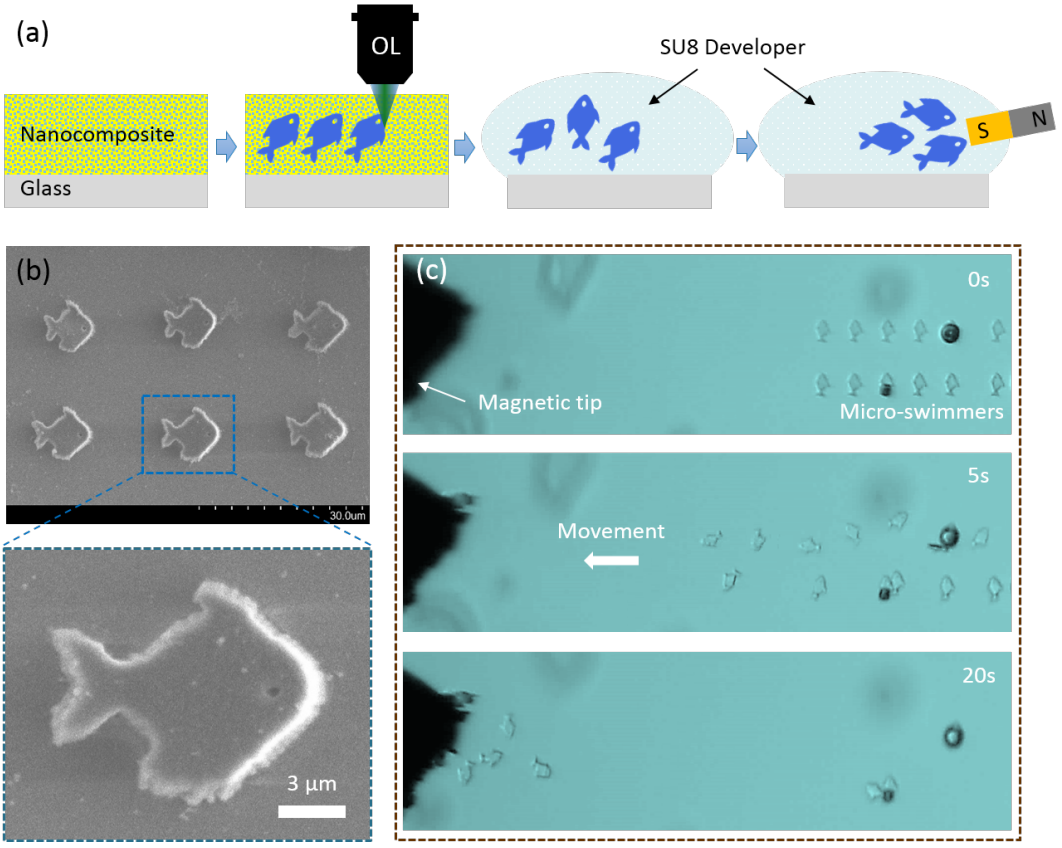

Figure 2: *(a) Illustration des processus de fabrication et de développement des micro-nageurs. (b) Image MEB et image agrandie des micro-nageurs fabriqués à 9 mW. (c) Captures d'écran montrant le mouvement des micro-nageurs vers la pointe magnétique.*

En deuxième lieu, nous avons utilisé un nanocomposite magnétique / polymère pour démontrer la fabrication de microstructures magnéto-photoniques à la demande en utilisant la technique DLW à base de LOPA. En incorporant des NPs magnétites superparamagnétiques (Fe_3O_4) dans la matrice polymère SU8 avec diverses viscosités de SU8, nous avons trouvé la valeur de viscosité la plus appropriée pour l'hébergement des MNPs pour donner la distribution uniforme des NPs à concentration d'environ 2% en poids sans sédimentation. Le temps de préparation de l'échantillon joue également un rôle important permettant l'amélioration remarquable de la dispersion MNPs laissant un nanocomposite magnétique de haute qualité. La dispersion homogène des MNPs

dans la matrice polymère permet de fabriquer les structures magnétiques souhaitées à l'échelle nanométrique. La technique DLW basée sur LOPA a été employée avec succès pour réaliser toutes les sous-microstructures 2D et 3D arbitraires. En outre, nous avons également démontré une possibilité de dispositifs magnéto-photoniques par la fabrication de microswimmers magnétiques mobiles (images MEB sur la Figure 2(b)) et par l'examen de leur interaction avec un champ magnétique externe avec un processus montré sur la Figure 2(a). La propriété de réponse magnétique élevée des structures hybrides permet le mouvement des structures vers les pointes magnétiques (Figure 2(c)). La technique DLW à base de LOPA a également été utilisée avec succès pour réaliser des cristaux magnéto-photoniques 3D et des microdispositifs avec des composants 3D complexes. Par conséquent, la combinaison de la technique DLW à base de LOPA avec un nanocomposite et à l'aide d'un champ magnétique externe permettra d'obtenir tous les dispositifs magnéto-photoniques désirés. Ceci ouvre de nombreuses applications prometteuses, telles que le développement d'outils microrobotiques pour le transport dans des systèmes biologiques.

En troisième lieu, nous avons étudié un autre type de NP, les NPs d'or, et les avons utilisées pour étudier le couplage à PS, pas comme des NPs aléatoires comme dans la partie précédente, mais comme des NPs individuelles. Nous avons démontré théoriquement et expérimentalement le couplage précis d'une NP d'or dans une microstructure photonique en utilisant la technique DLW LOPA. Des simulations basées sur la méthode FDTD ont prouvé le mécanisme du couplage de la longueur d'onde d'excitation dans les cavités, le couplage plasmonique/photonique et le couplage de la lumière émise des cavités qui prédisent l'amélioration du signal de fluorescence des NPs d'or. Le NP/PS couplé a été réalisé par une technique LOPA DLW, et avec un processus en deux étapes: une puissance d'excitation ultra-basse pour la détermination de la position NP, et une faible puissance d'excitation pour la fabrication des microstructures souhaitées. La Figure 3(a) montre une carte de fluorescence des NPs d'or séparés, révélés à faible puissance de balayage. La Figure 3(b) montre des images MEB de structures fabriquées contenant

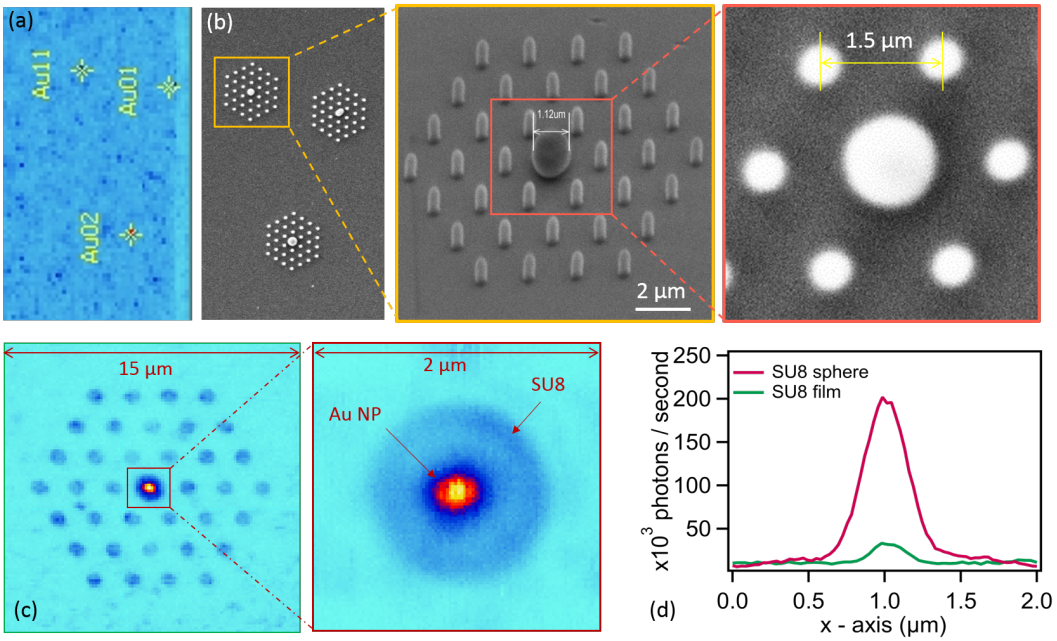

Figure 3: *(a) Image de fluorescence des NPs d'or avant la fabrication. (b) Des images MEB de structures fabriquées, chacune contenant un NP Au au centre et des images agrandies d'une structure fabriquée contenant une seule NP d'or. (c) Image de fluorescence de structures fabriquées obtenues en (xy)-plan et image agrandie de la microsphère contenant une seule NP d'or. La seule NP d'or verrouillé au centre offre des comptages d'intensité très élevée par rapport à ceux du milieu hôte SU8 voisin entouré d'air. (d) Comparaison des signaux de fluorescence dans deux cas, Au NP dans la microsphère (courbe rouge) et dans un film de photorésist SU-8 sans motif (courbe verte).*

ces NPs d'or. Nous avons rencontré un effet inattendu dû à la chaleur induite par le SPR des NPs d'or lors de la fabrication: au lieu d'un micropillier contenant une NP, nous avons obtenu une microsphère. Cependant, le couplage de NP à la microsphère a encore permis une grande amélioration du signal de fluorescence par rapport au cas sans couplage, ce qui est en bon accord avec la prédiction théorique (Figure 3(c, d)). On a étudié les NPs d'or de différentes tailles et le gain de fluorescence le plus élevé que nous avons obtenu, correspondant à une NP or de 10 nm, a atteint jusqu'à 36,6 fois. Ce DLW basé sur LOPA avec un processus en deux étapes s'est avéré être une technique très simple mais puissante pour incorporer des NPs individuelles dans PS par rapport à d'autres techniques compliquées et coûteuses.

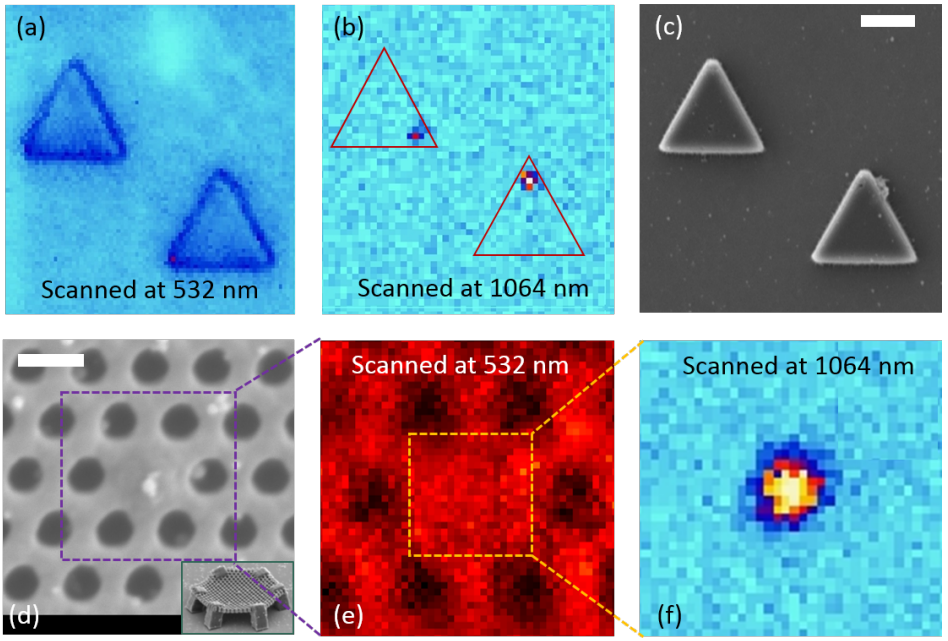

Figure 4: *(a) Image de fluorescence d'un ensemble de structures micro triangulaires (obtenues par balayage avec un laser à 532 nm). (b) Image GSH des structures montrant que les NPs de KTP sont incorporés dans différentes positions (obtenue par balayage avec un laser à 1064 nm). (c) Image MEB des structures. Barres d'échelle: 10 µm and 2 µm. (d) Image MEB d'une membrane hexagonale 3D contenant une NP KTP au centre; Encart: vue de côté. Barre d'échelle: 1 µm. (e) Image de fluorescence de la structure (obtenue par balayage avec un laser à 532 nm). (f) Image GSH du centre de la structure montrant qu'il contient une NP KTP (obtenue par balayage avec un laser à 1064 nm).*

En quatrième lieu, afin d'éviter l'effet d'explosion lors de l'exposition sous excitation laser, nous avons choisi d'étudier les NPs KTP car ils possèdent une large gamme de transparence incluant les longueurs d'onde utilisées. Nous avons étudié le couplage des NPs individuelles KTP et de différents types de structures. Dans un premier temps, nous avons étudié la générarion des secondes harmoniques des nanocristaux individuels de KTP de taille comprise entre 30 nm et 100 nm. Ces NPs KTP, sous excitation d'un laser puissant généré efficacement un signal de second harmonique. L'utilisation de KTP, avec ses coefficients non-linéaires élevés et sa transparence à la fois pour la longueur d'onde du laser d'excitation et le signal du second harmonique, conduit à un rapport signal sur bruit élevé ainsi qu'à une photostabilité parfaite. Nous avons ensuite

utilisé LOPA DLW pour réaliser la fabrication des PSs contenant des NPs KTP individuels. Les NPs de KTP ne provoquent pas d'explosion pendant la fabrication comme le font les NPs d'or, par conséquent, ils sont idéaux pour être manipulés et couplés à divers types de PS. Nous avons réussi à intégrer des NPs KTP individuels dans différents types de structures 2D et 3D, comme le montre la Figure 4. La taille et la forme des structures, ainsi que la position des NPs à l'intérieur des structures, peuvent être contrôlées à un petit pas. Nous avons trouvé une amélioration jusqu'à 90 fois du signal SHG d'un NP KTP intégré dans un pilier. L'amélioration était différente pour différents NPs (Figure 5(d)), car elle n'est pas seulement due à la résonance de la lumière fondamentale dans la cavité, mais aussi à l'orientation des nanocristaux de KTP, ce qui affecte l'efficacité de la collecte de l'OL. Un modèle de simulation utilisant la méthode FDTD a été étudié et a confirmé les résultats expérimentaux présentés de façon évidente dans la Figure 5(a-c).

En conclusion, nous avons étudié théoriquement et expérimentalement une méthode d'optimisation pour LOPA DLW, qui permet de surmonter certains inconvénients existant dans les structures polymériques telles que l'effet d'accumulation, l'effet de rétrécissement. Puis, en utilisant LOPA DLW en combinant avec cette méthode, nous avons étudié trois types de NPs, chacun d'entre eux possède des propriétés intérsantes différentes qui sont améliorées en incorporant avec une PS. Ces recherches ont prouvé la capacité remarquable de LOPA DLW et ouvrent également la voie à l'étude de nombreuses applications intéressantes de structures hybrides.

Perspectives

Pour les travaux futurs, nous soulignons quelques recherches potentielles qui peuvent suivre cette étude de thèse:

- Le PEB local peut être étudié à basse température. Alors que les zones environnantes sont maintenues à une température basse constante et que seule la zone à

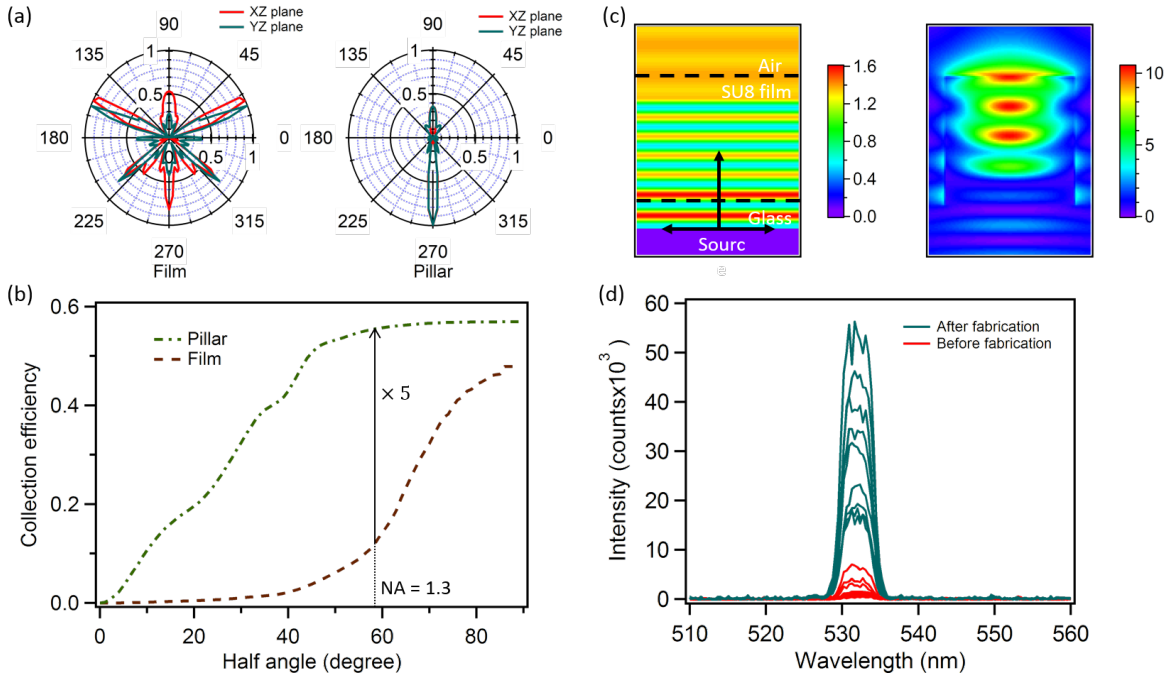

Figure 5: *(a) Les modèles de rayonnement d'un dipôle situé dans différentes structures. À gauche: diagramme d'émission en (xz) et (yz)-plan d'une structure de film. À droite: diagramme d'émission en (yz) et (yz)-plan d'une structure de pilier. (b) Calcul de l'efficacité de la collecte du signal SH en fonction du demi-angle de la lentille d'objectif dans deux cas: KTP NP dans un pilier et KTP NP dans un film mince. (c) Couplage de la lumière fondamentale dans une cavité de pilier: intensité de champ calculée (module carré du champ électrique) à la longueur d'onde de 1064 nm à l'intérieur d'un pilier d'un diamètre de 800 nm et d'une hauteur de 1,3 µm) et à l'intérieur d'un film SU8 d'une épaisseur de 1,3 µm (gauche). (d) Comparaison des signaux SHG de différents NP KTP intégrés dans des piliers avec des paramètres identiques avant (courbes rouges) et après fabrication (courbes vertes).*

l'endroit de focalisation est chauffée, il est possible d'obtenir des structures avec des tailles encore plus petites que la limite de diffraction.

- Nous avons fabriqué avec succès des microstructures magnéto-photoniques en utilisant un nanocomposite magnétique avec MNP orientés aléatoirement. Il est également possible d'étudier des structures réalisées à partir de MNP pré-orientés en appliquant un champ magnétique externe lors de la fabrication. Une autre possibilité est d'étudier des MNPs uniques pour créer des structures magnétiques à

domaine unique.

- Pour les NPs de KTP, des recherches plus approfondies sur les microstructures 3D à la fois théoriques et expérimentales sont nécessaires, car la lumière fondamentale peut avoir une résonance plus élevée dans les cavités 3D, ce qui peut améliorer considérablement le signal SHG des NPs de KTP.

université PARIS-SACLAY | ÉCOLE DOCTORALE Physique et ingénierie : électrons, photons, sciences du vivant (EOBE)

Titre : Etudes théorique et expérimentale du couplage des nanoparticules uniques dans des structures photoniques à base de polymère

Mots clés : Ecriture directe par laser, Polymère, Structure photonique, source de photon unique, Plasmonique, Microfabrication

Résumé : Dans ce travail, nous étudions théoriquement et expérimentalement le couplage entre nanoparticules uniques de différentes natures (fluorescentes, non-linéaires, plasmoniques, etc.) et une structure photonique en matériau polymère. Dans un premier temps, nous avons optimisé la méthode dite écriture directe par laser en régime de faible absorption à un photon (LOPA) pour réaliser des structures photoniques de bonne qualité à la demande. Ensuite, nous avons également exploité l'effet thermique induit par le laser d'excitation continue, pour simplifier la méthode de fabrication LOPA et améliorer les structures fabriquées. Puis nous avons introduit de façon précise une nanoparticule unique à un emplacement contrôlé dans la structure photonique. Le couplage nanoparticule/structure photonique a été réalisé par le même système optique. Ce couplage a été démontré par une augmentation du nombre de photons émis par la nanoparticule fluorescente et par une forte amélioration du signal de génération de seconde harmonique. Parallèlement, nous avons effectué des calculs numériques par la méthode FDTD pour prédire les propriétés optiques intéressantes des structures photoniques et pour confirmer les résultats expérimentaux.

Title : Controlled coupling of nanoparticles to polymer-based photonic structures

Keywords : Photonic coupling, Ultralow one-photon absorption, Nanoparticle, Microfabrication

Abstract : In this study, we investigate theoretically and experimentally the coupling between nanoparticle and photonic structures. The work focuses on the elaboration and applications of structured polymer materials, as well as the manipulation of optical properties of various kinds of single nano-fillers such as gold nanoparticles, magnetic and nonlinear nanoparticles, etc. The study of each kind of nanoparticle addresses a specific goal. In order to conduct our research, we first built and tested an optical confocal setup, which allowed us to both image and fabricate nanostructures at a sub-lambda resolution. Besides, we propose a method exploiting the thermal effect caused by a continuous-wave laser source to optimize 2D and 3D structures realized by low one-photon absorption (LOPA)-based direct laser writing (DLW).Then by using this technique, we are capable of creating novel 2D and 3D polymeric photonic structures containing nanoparticles of different kind (gold nanoparticles, nonlinear nanoparticles, and magnetic nanoparticles). The characterization of the fabricated structures was carried out using the same confocal setup. We demonstrated a significant enhancement of the optical properties of the nanoparticles embedded inside the photonic structures. We also performed numerical calculations using a finite different time domain (FDTD) method to confirm the experimental results.